



UNIVERSIDADE ESTADUAL DE CAMPINAS
Faculdade de Engenharia Elétrica e de Computação

Julio Enrique Valentín Fajardo Hernández

Robust Filtering and Control Strategies Applied to Assistive Robotics

Filtragem Robusta e Estratégias de Controle Aplicadas à Robótica Assistiva

Campinas

2023

Julio Enrique Valentín Fajardo Hernández

Robust Filtering and Control Strategies Applied to Assistive Robotics

Filtragem Robusta e Estratégias de Controle Aplicadas à Robótica Assistiva

Doctorate thesis presented to the School of Electrical and Computer Engineering of the University of Campinas in partial fulfillment of the requirements for the degree of Doctor in Electrical Engineering, in the area of Computer Engineering.

Tese apresentada à Faculdade de Engenharia Elétrica e de Computação da Universidade Estadual de Campinas como parte dos requisitos exigidos para a obtenção do título de Doutor em Engenharia Elétrica, na Área de Engenharia de Computação.

Supervisor: Prof. Dr. Eric Rohmer

Este trabalho corresponde à versão final da dissertação/tese defendida pelo aluno Julio Enrique Valentín Fajardo Hernández, e orientada pelo Prof. Dr. Eric Rohmer.

Campinas

2023

Ficha catalográfica
Universidade Estadual de Campinas
Biblioteca da Área de Engenharia e Arquitetura
Rose Meire da Silva - CRB 8/5974

Fajardo, Julio, 1984-
F178r Robust filtering and control strategies applied to assistive robotics / Julio Enrique Valentín Fajardo Hernández. – Campinas, SP : [s.n.], 2023.

Orientador: Eric Rohmer.
Tese (doutorado) – Universidade Estadual de Campinas, Faculdade de Engenharia Elétrica e de Computação.

1. Prótese robótica. 2. Otimização robusta. 3. Estratégia de controle híbrido.
I. Rohmer, Eric, 1974-. II. Universidade Estadual de Campinas. Faculdade de Engenharia Elétrica e de Computação. III. Título.

Informações Complementares

Título em outro idioma: Filtragem robusta e estratégias de controle aplicadas à robótica assistiva

Palavras-chave em inglês:

Robotic prosthesis

Robust optimization

Hybrid control strategy

Área de concentração: Engenharia de Computação

Titulação: Doutor em Engenharia Elétrica

Banca examinadora:

Eric Rohmer [Orientador]

Matheus Souza

Ricardo Coração de Leão Fontoura de Oliveira

Fernando Santos Osório

Alexandre da Silva Simões

Data de defesa: 30-05-2023

Programa de Pós-Graduação: Engenharia Elétrica

Identificação e informações acadêmicas do(a) aluno(a)

- ORCID do autor: <https://orcid.org/0000-0003-4034-189X>

- Currículo Lattes do autor: <http://lattes.cnpq.br/1979004341071680>

COMISSÃO JULGADORA – TESE DE DOUTORADO

Candidato: Julio Enrique Valentín Fajardo Hernández RA: 209479

Data da Defesa: 30 de maio de 2023

Título da Tese: “Filtragem robusta e estratégias de controle aplicadas à robótica assistiva”.

Prof. Dr. Eric Rohmer

Prof. Dr. Matheus Souza

Prof. Dr. Ricardo Coração de Leão Fontoura de Oliveira

Prof. Dr. Fernando Santos Osório

Prof. Dr. Alexandre da Silva Simões

A ata de defesa, com as respectivas assinaturas dos membros da Comissão Julgadora, encontra-se no SIGA (Sistema de Fluxo de Dissertação/Tese) e na Secretaria de PósGraduação da Faculdade de Engenharia Elétrica e de Computação.

I dedicate this thesis to God, who has been my guiding light throughout this journey. Without His grace, I would not have had the strength and courage to achieve this milestone in my life. To my family, especially my mother, father, wife, and children, who have been my unwavering source of support, love, and motivation. Your sacrifices, patience, and understanding have been invaluable to me, and I am forever grateful. To Galileo University and the authorities who allowed me to fulfill my dream of higher education. Thank you for providing the necessary resources, opportunities, and guidance to help me grow and develop as a student and as an individual. This thesis is a testament to the hard work, dedication, and perseverance of all those who have played a part in my academic journey. Thank you all for your unwavering support and for believing in me.

Acknowledgements

First and foremost, I would like to express my gratitude to God, who has been my constant source of strength and inspiration throughout this journey. His blessings and guidance have made this research possible, and I am truly grateful for His unwavering support. To Galileo University, I am immensely grateful for the opportunity to participate in the research process and for the generous funding for the research, publication, and attendance at international conferences. The support and resources provided by the university have been invaluable in the successful completion of this thesis. I want to sincerely thank the Brazilian agencies São Paulo Research Foundation (FAPESP) and the Brazilian Institute of Neuroscience and Neurotechnology (BRAINN) CEPID-FAPESP for their financial support (Grant 2013/07559-3). Their funding has been critical in realizing this research, and I am honored to have received their support. Lastly, I thank my advisor and committee members for their guidance, expertise, and feedback throughout the research process. Their constructive criticism and valuable insights have been invaluable in shaping this thesis. In conclusion, I express my gratitude to all those who have made this research possible. Your support, encouragement, and belief in me have been instrumental in this achievement.

“Unveiling the Nexus of Intelligence and Ingenuity: Pioneering the Future through Robotics.”

Resumo

A robótica assistiva desempenha um papel fundamental na melhoria da qualidade de vida e independência de indivíduos com deficiências ou limitações. Encontrar um compromisso adequado entre funcionalidade e custo é crucial na criação de dispositivos acessíveis e econômicos para aqueles que precisam deles. Essa seleção requer um foco no desenvolvimento de tecnologias inovadoras que possam fornecer o nível de suporte necessário, mantendo os custos sob controle. Por exemplo, o abandono do uso das mãos prostéticas multifuncionais deve-se à funcionalidade limitada que algumas podem oferecer. Essa questão está diretamente relacionada à controlabilidade da torção exercida pelos dedos e à responsividade que a prótese pode proporcionar na interação com diversos objetos durante as atividades da vida diária. A maioria das abordagens típicas para esse problema envolve o uso de sensores e mecanismos complexos que aumentam recursos críticos, como o preço, tamanho e peso do dispositivo prostético, afetando a reproduzibilidade e a capacidade de manutenção. Em um outro lado, o problema de localização é um desafio crítico na robótica móvel, pois determina a capacidade do robô de navegar e interagir com seu ambiente com precisão. A localização permite que os robôs executem tarefas com eficiência e segurança, tornando-se um fator crucial no desenvolvimento de sistemas móveis autônomos, como cadeiras de rodas inteligentes. Este trabalho propõe técnicas de filtragem robustas que abordam as desvantagens de mãos prostéticas acionadas por tendão sem sensor e para o problema de localização de robôs baseado em pontos de referência. Essas estratégias são baseadas em métodos de filtragem ótimos e robustos através de procedimentos de otimização baseados em desigualdades matriciais lineares, garantindo maior robustez ao processo de estimativa. Essas estratégias foram validadas usando um dispositivo prostético de membro superior de código aberto e um robô móvel de acionamento diferencial, mostrando resultados satisfatórios. Para a primeira abordagem, erros de estimativa entre $0,0490 \pm 0,0031$ e $0,0764 \pm 0,0052$ rad foram obtidos para o deslocamento angular do redutor dos motores DC de cada dedo. Além disso, a estratégia de controle foi testada por meio da apreensão de objetos comuns utilizados no dia-a-dia. Por fim, a segunda abordagem foi testada e comparada com o filtro de Kalman estendido para localização mostrando melhores resultados em ambientes pequenos.

Palavras-chaves: Prótese de membro superior, robô de acionamento diferencial, sistema sem sensor, localização baseada em pontos de referência, desigualdades matriciais lineares, controle robusto, observador robusto..

Abstract

Assistive robotics plays a crucial role in enhancing the quality of life and independence of individuals with disabilities or limitations. Finding a suitable trade-off between functionality and cost is crucial in creating devices that are accessible and affordable to those who need them. This selection requires a focus on developing innovative technologies that can provide the necessary level of support while keeping costs in check. For example, the abandonment of multifunctional prosthetic hands has been due to the limited functionality that some can offer. This issue is directly related to the controllability of the wrench exerted by the fingers and the responsiveness that the prosthesis may provide while interacting with different objects during activities of daily living. Most typical approaches to this problem involve using complex array sensors and complex mechanisms that increase critical features, such as the prosthetic device's price, size, and weight, affecting reproducibility and maintainability. On the other hand, the localization problem is a critical challenge in mobile robotics, as it determines the robot's ability to navigate and interact with its environment accurately. Localization enables robots to perform tasks efficiently and safely, making it a crucial factor in developing autonomous mobile systems such as intelligent wheelchairs. This work proposes robust filtering techniques that addresses drawbacks for sensorless under-tendon-driven prosthetic hands and for the landmark-based localization problem. These strategies are based on optimal and robust filtering methods through optimization procedures based on linear matrix inequalities, guaranteeing better robustness to the estimation process. These strategies were validated using an open-source upper-limb prosthetic device and differential drive mobile robot showing satisfactory results. For the first approach, estimation errors between 0.0490 ± 0.0031 and 0.0764 ± 0.0052 rad were obtained for the angular displacement of the gearhead of the DC motors of each finger. Besides, the control strategy were tested by grasping common objects of daily living. Finally, the second approach was tested and compared with the extended Kalman filter for localization showing better results in small environments.

Keywords: Upper-limb prosthesis, differential drive robot, sensorless system, landmark-based localization, linear matrix inequalities, robust control, robust observer.

List of Figures

Figure 2.1 – Pioneer P3DX differential wheeled robot from Adept Robots into an indoor environment.	45
Figure 2.2 – Mechanical design of the Galileo Hand.	50
Figure 2.3 – Top view of the modular palm sections. (1) The main PCB board controller. (2) Motors driving the index, middle, ring and little fingers. (3) Actuator in charge of the rotation of the thumb.	51
Figure 2.4 – Thumb mechanism side view, beveloid gear pair.	52
Figure 2.5 – UTD system, where r_1 , r_2 , r_3 and r_a , are the pulleys' radix; θ , the gearhead shaft's angular position; l_1 , l_2 and l_3 the length of each phalanx and τ_1 , τ_2 and τ_3 the joint's torque.	53
Figure 2.6 – System block diagram showing the embedded controller architecture and the integration with external modules.	56
Figure 2.7 – The image shows the Galileo Hand grabbing the objects used in the trials. (a) Holding a "water bottle"; (b), holding a small plastic "ball"; (c), holding a "wallet" and (d), "pointing".	57
Figure 2.8 – Finite State Machine showing the behavior of the interface using buttons and the Myo to operate. S_0 indicates that the hand is completely open; S_1 , that there was a change in the selected grip; S_2 , that the selected grip is being performed (when it is completed, the flag f_1 is lifted). Also, S_3 represents that the hand is currently enacting the chosen gesture; while, S_4 , that the fingers are opening (process that informs it is finished by lifting the flag f_2).	58
Figure 2.9 – Galileo Hand's graphical menu (left) and the prosthesis performing the action "Close" (right).	59
Figure 4.1 – Discrete-time system with a full order filter scheme.	69
Figure 5.1 – FSM demonstrating the opening/closing behaviour of each finger.	75
Figure 6.1 – (a) A limb-impaired volunteer tests the Galileo Hand holding a water bottle. (b) The test bed used to standardize the experiment iterations of each finger interacting with a small plastic ball.	78
Figure 6.2 – (a) Gearhead shaft's angular displacement, θ . The dotted red line represents the estimation $\hat{\theta}$; solid blue line, the ground truth. (b) The motor's armature current, i_a	79

Figure 6.3 – The response of the robust controller during the extension process, (a) Gearhead shaft's angular displacement, θ , and (b) velocity, respectively.	81
Performance of the estimator during a full power extension process,	
(c) Solid blue line is the gearhead shaft's angular displacement, θ . The dotted red line represents the $\hat{\theta}$ estimation, and (d), the current, i_a , measured on the motor's armature.	
Figure 6.4 – Torque τ applied on the MCP, PIP and DIP joints' axes (τ_1, τ_2 and τ_3 , correspondingly).	82
Figure 6.5 – Fingertip force f_{tip} exerted by the finger in x (red) and y (green) directions, as well as the magnitude of the resultant force (blue).	83
Figure 6.6 – (a) Estimated trajectory of the index finger. The solid blue line represents the trajectory of the fingertip, green and red dotted lines are the DIP and PIP joints. (b) Simulated trajectory with final generalized coordinates $\hat{\mathbf{q}} = [0.946, 1.040, 0.903]^T$ rad. (c) The ground truth for the estimated flexion process with final generalized coordinates $\mathbf{q} = [0.9323, 0.973, 0.891]^T$ rad. Either simulation and ground truth flexion movement starts in $\mathbf{q}_0 = [0.279, 0.209, 0.105]^T$ rad.	84
Figure 6.7 – Robot trajectory under a real controlled environment. The green cross is the robot's initial position; the blue is the final estimated position. The green and dotted red lines are the ground truth and the estimated trajectory, respectively.	85
Figure 6.8 – Pioneer P3DX differential wheeled mobile robots during localization tests under the real scenario.	86
Figure 6.9 – Robot pose estimation error throughout each iteration using the method proposed in Section 4.1 under a real scenario, and using the method proposed in Section 4.2 under simulation environment are in sub-figures (a) and (b). (c) EKF pose estimation error under a real scenario. (d) Robustness level γ using the method proposed in Section 4.2 under the real environment.	87

List of Tables

Table 6.1 – Mass and length of the proximal, middle, and distal phalanges, as well as the radius of the MCP, PIP, and DIP joints for each finger.	80
Table 6.2 – Ground truth and estimation error for all iterations on each finger under estimation methods proposed.	81

List of abbreviations and acronyms

ADL	Activity of Daily Living
AI	Artificial Intelligence
AR	Augmented Reality
BIBO	Bounded Input, Bounded Output
BLE	Bluetooth Low Energy
DIP	Distal InterPhalangeal
DOA	Degrees of Actuation
DOF	Degrees of Freedom
EKF	Extended Kalman Filter
EMG	ElectroMyoGraphy
FPGA	Field Programmable Gate Array
FSR	Force Sensitive Resistor
HLC	High-Level Controller
ICP	Iterative Closest Points
KF	Kalman Filter
LiDAR	Light Detection and Ranging
LMI	Linear Matrix Inequalities
LPV	Linear Parameter-Varying
MCL	Monte Carlo Localization
MCP	MetaCarpoPhalangeal
MCU	Microcontroller Unit
ML	Machine Learning
NCP	Normal Distribution Transforms

PC	Personal Computer
PIP	Proximal InterPhalangeal
PF	Particle Filter
RMSE	Root Means Square Error
SBC	Single-Board Computer
SD	Standard Deviation
SLAM	Simultaneous Localization and Mapping
UPI	User-Prosthesis Interface
UART	Universal Asynchronous Receiver/Transmitter
UTD	Under-Tendon-Driven
VR	Virtual Reality

List of symbols

$\mathbb{R}^{n \times p}$	Set of real matrices of dimension n by p
$\mathbb{C}^{n \times p}$	Set of complex matrices of dimension n by p
\forall	For all
\exists	Exists
\in	Is an element of
\subset	Subset of
$\langle \mathbf{a}, \mathbf{b} \rangle$	The inner product between \mathbf{a} and \mathbf{b}
\mathbf{A}^*	Transpose Conjugate of Matrix \mathbf{A}
\mathbf{A}^T	Transpose of Matrix \mathbf{A}
\mathbf{A}^{-1}	Inverse of Matrix \mathbf{A}
$\mathbf{P} > 0$	Positive definite \mathbf{P} matrix
$\mathbf{P} \geq 0$	Positive semi-definite \mathbf{P} matrix
$\mathbf{P} = \mathbf{P}^T$	Symmetric matrix \mathbf{P}
$\text{Tr}(\mathbf{A})$	Trace (sum of elements on the main diagonal) of matrix \mathbf{A}
$\bar{\sigma}(\mathbf{A})$	Maximum singular value of matrix \mathbf{A}
\mathcal{L}_p	Signal norm for $p = 1, 2, \dots, \infty$.
\mathcal{H}_p	System norm for $p = 1, 2, \dots, \infty$.
\mathbf{A}^\perp	Matrix that consists of columns that make up a basis for the null space of matrix \mathbf{A} .
\min	Minimize verb, used in optimization problems
$\arctan(\theta)$	The inverse of the tangent function (\tan) of an angle θ
$\text{rank}(\mathbf{A})$	Rank of matrix \mathbf{A}
t	Continuous-time variable
k	Discrete-time variable

s	Laplace variable
z	Complex variable for discrete-time systems
\mathcal{N}	Gaussian distribution
μ_t	Greek letter mu, the mean of the Gaussian distribution
Σ_t	Greek letter Sigma, the covariance matrix of the Gaussian distribution
$p(a b)$	Probability of a given b
$\mathbf{P}_{a b}$	Probability matrix of a given b
$bel(\mathbf{x}_t)$	The belief, Gaussian distribution
$\sum_{t \in I} h(k)$	Sum of the sequence $h(k)$ on an interval I
$\int_{t \in I} f(t)dt$	Integral of the function $f(t)$ on an interval I
$\sup_{t \in I} f(t)$	Supremum of the function $f(t)$ on an interval I
$\text{ess sup}_{t \in I} f(t)$	Essential supremum of the function $f(t)$ on an interval I

Contents

1	INTRODUCTION	19
1.1	Publications	26
2	FUNDAMENTALS	27
2.1	Signal and System Norms	27
2.1.1	Basic Concepts	27
2.1.2	Hilbert Spaces	28
2.1.3	Hardy Spaces \mathcal{H}_2 and \mathcal{H}_∞	29
2.1.4	Linear Matrix Inequalities (LMIs)	32
2.1.5	Finsler's Lemma	32
2.1.6	Projection Lemma	33
2.2	\mathcal{H}_2 and \mathcal{H}_∞ Norms using LMIs	34
2.2.1	\mathcal{H}_2 Norm	34
2.2.1.1	Continuous-time Systems	35
2.2.1.2	Discrete-time Systems	36
2.2.2	\mathcal{H}_∞ Norm	37
2.2.2.1	Continuous-time Systems	37
2.2.2.2	Discrete-time Systems	39
2.3	Bayesian Filters	40
2.3.1	Kalman Filter	41
2.3.2	Extended Kalman Filter	42
2.3.3	Particle Filter	43
2.4	Differential Wheeled Robot	44
2.4.1	Dead-Reckoning	44
2.4.2	Markov Localization	45
2.4.3	Kalman Filter Localization	47
2.4.4	Extended Kalman Filter Localization	48
2.4.5	Monte Carlo Localization	49
2.5	Galileo Hand	50
2.5.1	Palm Design and Mechanisms	51
2.5.2	Thumb Movement Characteristics	51
2.6	The Under-tendon-driven Machine	52
2.7	User-prostheses Interface	54
2.7.1	High Level Controller	55
2.7.1.1	Gestures adapted to the prosthesis	56

2.7.1.2	Multimodal approach using buttons and Myo interface	57
3	PROBLEM STATEMENT	60
3.1	Robust Control Strategy for Sensorless UTD Prosthetic Hands	61
3.2	\mathcal{H}_∞ Estimation for Landmark-based Mobile Robot Localization	62
4	LMI-BASED \mathcal{H}_∞ ROBUST FILTERING	65
4.1	Discrete-time \mathcal{H}_∞ Full-State Estimator	65
4.2	Discrete-time \mathcal{H}_∞ Filter	69
5	CONTROL STRATEGY	74
5.1	On-off Controller	75
5.2	Discrete-time \mathcal{H}_∞ Feedback Controller	76
6	RESULTS	78
6.1	Robust Control Strategy for Sensorless UTD Prosthetic Hands	78
6.2	\mathcal{H}_∞ Filters for Landmark-based Mobile Robot Localization	85
7	CONCLUSIONS	89
	BIBLIOGRAPHY	92

1 Introduction

Robotics has become essential for society due to its immense potential to automate various industrial and service sector processes. Also, it offers high accuracy, consistency, and precision for the abovementioned processes, which are difficult to achieve through traditional human labor. The use of robots for some processes also increases productivity and efficiency while reducing the overall costs of production, and also plays a critical role in fields such as healthcare, where robots can perform surgery and assist in patient care, and space exploration, where robots can operate in environments too harsh for human exploration. In addition, with advances in Artificial Intelligence (AI) and Machine Learning (ML), robots are becoming more intelligent and autonomous, allowing them to make decisions and perform complex tasks with greater accuracy and efficiency. Moreover, robotics is a crucial technology that is revolutionizing various industries, such as healthcare, improving the quality of life for people worldwide. This way, intelligent prostheses, and assistive and rehabilitation robotics play a crucial role in society by providing individuals with disabilities, injuries, and physical impairments with greater independence, mobility, and functionality. These advanced technologies enhance the quality of life by enabling impaired ones to perform daily activities, such as walking and grasping objects. In addition to promoting physical rehabilitation, intelligent prostheses can improve mental and emotional well-being by restoring self-confidence, autonomy, and a sense of purpose. These devices have the potential to revolutionize healthcare, improve patient outcomes, and reduce the burden on healthcare providers by enabling patients to manage their conditions independently. As the population ages, the demand for these robotics devices will continue to grow, making it increasingly necessary to invest in developing and integrating these technologies into society.

The last World Report on Disabilities shows that at least 30 million people with amputations reside in developing countries, and most of them cannot acquire prosthetic care or afford leading commercial assistive technology with pricing around \$1000, such as upper-limb prosthetic devices ([PILLING; BARRETT; FLOYD, 2004](#); [ORGANIZATION *et al.*, ; CUMMINGS, 1996](#); [KATE; SMIT; BREEDVELD, 2017](#)). Meanwhile, several research laboratories focus on improving dexterity and biomimetics of prosthetic hands, and implementing expensive and intrusive ways to gather the user intent ([BRIDGES; PARA; MASHNER, 2011](#); [LEVY; BEATY, 2011](#); [HOTSON *et al.*, 2016](#); [CIPRIANI; CONTROZZI; CARROZZA, 2010](#); [CIPRIANI; CONTROZZI; CARROZZA, 2011](#)). Sometimes, neglecting other vital aspects of the prosthetic device, like aesthetics, controllability, and the user interface, the lack of which can influence patients to stop using them ([CORDELLA *et al.*, 2016](#)).

Due to the limitations of conventional body-powered prostheses, like steel hooks, and the elevated cost, weight, and difficulties in repairing commercial myoelectric prosthetic devices (MEDYNSKI; RATTRAY, 2011; TROCCAZ; CONNOLLY, 2008; KONTOUDIS *et al.*, 2015), many open-source projects based on 3D printing technologies have been released (KONTOUDIS *et al.*, 2015; SLADE *et al.*, 2015; AKHTAR *et al.*, 2016; FAJARDO; LEMUS; ROHMER, 2015), whose target is a lightweight and affordable upper-limb prosthetic device. These limitations encourage its widespread distribution through global networks by reducing manufacturing costs. That is why the implementation of such technology in assistive devices has been increasing, improving availability, pricing and can also offer an extended set of grasps and functionality (KONTOUDIS *et al.*, 2015; SLADE *et al.*, 2015; AKHTAR *et al.*, 2016; FAJARDO *et al.*, 2017).

Overall, the choice of upper limb prostheses depends on the individual needs and preferences of the user, as well as their level of amputation and residual limb function. Thus, a prosthetist can work with the impaired to determine the most appropriate type of prosthesis and ensure a proper fit and functionality. This way, the several advantages offered by multifunctional bionic upper limb prostheses compared to passive and body-powered ones improve the quality of life of impaired ones while interacting with different objects during activities of daily living (ADLs). However, the rejection rate for adults is around 23%, likely due to the weight, cost, repairability, and maintenance offered by most available alternatives (BIDDISS; CHAU, 2007). On the other hand, both low- and high-level control strategy directly affects the use of the prosthetic device and its performance, mainly due to the poor functionality to interact with objects and interpret the user's intent. This way, certain aspects such as overall strength and precision can be improved using efficient low-level controller/observer approaches implemented in compact, lightweight, and affordable systems.

Most approaches employ transducers to close the feedback control loops and improve functionality during ADLs. Rotational and linear potentiometers, quadrature encoders, and force or tactile/pressure sensors have been used to increase the functionality of the prosthetic hands by controlling the speed and the strength exerted by each finger (CRANNY *et al.*, 2005; CIPRIANI; CONTROZZI; CARROZZA, 2011; AKHTAR *et al.*, 2016; JIANG *et al.*, 2014). Nevertheless, these approaches entail an increase in price, size, and weight of the prosthetic device, leading the impaired ones to settle with lightweight aesthetic prostheses and, in some cases, not to use any at all (SCIENCES; MEDICINE *et al.*, 2017; SUL, 2011).

Alternatively, sensorless control systems are employed to compensate for some of the disadvantages of sensor-based systems. These approaches tend to either implement open-loop or observer-based techniques. The first one requires the user to regulate the speed and force exerted by the prosthesis according to the behavior perceived by the user showing

an affordable and straightforward option for achieving the desired purpose (AKHTAR *et al.*, 2016). However, it presents difficulties for the user to adjust its parameters without haptics and only through visual stimuli. Typical approaches to close the position or force control loops in prosthetic hands involve using potentiometers or quadrature encoders and pressure sensors, respectively (CRANNY *et al.*, 2005; CIPRIANI; CONTROZZI; CARROZZA, 2011; AKHTAR *et al.*, 2016; JIANG *et al.*, 2014). Some of them employ complex control strategies that combine multiple feedback loops and anti-windup schemes, improving its overall performance; however, it increases the price and the device's size, leading patients to not buy or to abandon their assistive device (SEOK, 2006; ENGEBERG; MEEK; MINOR, 2008; SCIENCES; MEDICINE *et al.*, 2017).

The use of sensory feedback provides the patients a more realistic substitute for their biological counterparts, conveying information as thermal, pressure, strain, or vibrational stimuli (CHORTOS; LIU; BAO, 2016; JIMENEZ; FISHEL, 2014). This tactile feedback has been shown to be important since the coordination, manipulation, and grip selection whilst interacting with everyday items has been demonstrated to worsen when having a lower sensitivity (ROTHWELL *et al.*, 1982; JOHANSSON; WESTLING, 1984; MONZÉE; LAMARRE; SMITH, 2003). However, haptics alone does not improve the user's interaction with common objects. This leads to employing different kinds of transducers to close the feedback control loops of the assistive devices to increase their usability during ADLs. In this way, these approaches increase the price and, in some cases, the prosthesis's size, leading the patients to settle with lightweight aesthetic prostheses or not to use any at all (SCIENCES; MEDICINE *et al.*, 2017; SUL, 2011).

Other approaches rely on using full-order state observers by measuring the current demanded by the actuators to estimate the entire state of the system. In contrast, this approach can even allow the system to eliminate the use of sensors on a prosthetic device, reduce its size and cost, and facilitate its repairability and maintenance (VAZQUEZ-SANCHEZ; SOTTILE; GOMEZ-GIL, 2017). In general, for brushed DC motors, the angular velocity of the motor shaft can be estimated based on the ripple component of the signal (SINCERO; CROS; VIAROUGE, 2008; FIGARELLA; JANSEN, 2007). On the other hand, the full state of the system can also be estimated based on its dynamic linear model (YACHIANGKAM *et al.*, 2004; BOWES; SEVINC; HOLLIDAY, 2004). Thus, it is more convenient to employ a stochastic dynamical system to improve the estimation of their states. These methodologies, such as the Kalman (KF), extended Kalman (EKF), and particle (PF) filters, provide robustness to the exogenous disturbances that may arise from the sensor and the process itself (PRAESOMBOON *et al.*, 2009; KHALID; NAWAZ, 2014; AYDOGMUS; TALU, 2011). Their main drawback is that the resulting errors and noises must be modeled as Gaussian, causing practical application issues. As opposed to the stochastic counterpart, \mathcal{H}_∞ -based, energy-bounded estimators may obtain similar results with a convergent solution without an idealized model of the noise (FAJARDO *et*

al., 2020; FAJARDO *et al.*, 2021).

Furthermore, some approaches that involve the non-linear model of brushed DC motors employ artificial neural networks to approximate it, specifically in prosthetic devices (CASTANEDA *et al.*, 2011; LIU; LUO; RASHID, 2003; FARKAS; HALÁSZ; KÁDÁR, 2004; WEERASOORIYA; EL-SHARKAWI, 1991). However, this leads to high computational needs, similar to those using sensors with complex algorithms, which leads to using relatively large, heavy, and expensive microcontroller units (MCUs), Field Programmable Gate Arrays (FPGAs), or single-board computers (SBCs) (GAETANI *et al.*, 2018; CHEN *et al.*, 2011).

On the other hand, mobile assistive robotics, such as autonomous wheelchairs, play an essential role in improving the quality of life and independence of people with disabilities. These innovative devices offer mobility previously unavailable to people with physical limitations, allowing them to navigate and interact with their environment in a way that was once thought impossible. Autonomous technology in wheelchairs gives users increased control over their movements, enabling them to move more freely, safely, and efficiently. Moreover, using these devices may reduce the burden on caregivers and healthcare professionals, allowing them to focus on other areas of care, leading to greater efficiency in care provision, improved patient outcomes, and reduced healthcare system costs. Additionally, autonomous wheelchairs may reduce the risk of injury to users and caregivers and reduce the physical strain of manual handling, reducing healthcare costs and improving health outcomes.

The importance of these devices lies in their ability to empower individuals with physical disabilities and improve their quality of life. With advances in technology and continued research and development, these devices have the potential to revolutionize the way people with disabilities live and interact with their environments, providing them with greater independence and freedom of movement. Therefore, to achieve a sufficient level of autonomy, following the see-think-act developed by (SIEGWART; NOURBAKHSH; SCARAMUZZA, 2011) is necessary. This scheme describes the three critical steps an autonomous mobile robot must perform to navigate and interact with its environment safely and effectively.

The first step in the see-think-act scheme is "see". This step involves the robot perceiving and understanding its environment through various sensors such as cameras, LiDARs, radars, and other sensors. These sensors provide the robot with information about its surroundings, such as obstacles, other objects, and terrain features. The second step is "think". In this step, the robot processes the information gathered from its sensors and generates a map of its environment, localizing it within it. This map is used to plan a safe and efficient path for the robot to navigate through the environment. The robot also uses its "thinking" capability to make decisions based on the data gathered from its

sensors, such as avoiding obstacles or adjusting its speed based on the terrain. The third and final step is "act". In this step, the robot executes its planned actions based on its environment and its decisions. For example, if the robot detects an obstacle in its path, it will adjust its path accordingly to avoid the obstacle. Thus, the see-think-act scheme is a powerful tool for autonomous mobile robots, allowing them to navigate and interact with their environment safely and effectively. By perceiving their environment, processing the data, and acting on the information, robots can perform tasks that would otherwise be impossible for humans. With ongoing advancements in robotics technology, we can expect to see even more sophisticated and capable autonomous mobile robots, leveraging the see-think-act scheme and other principles of robotics to accomplish a wide range of tasks in various settings ([SIEGWART; NOURBAKHSH; SCARAMUZZA, 2011](#)).

Therefore, the localization problem plays a fundamental task in autonomous navigation systems, from simple tasks such as vacuum cleaners and floor mops to self-driving cars and autonomous wheelchairs. This task has been studied over decades, facilitating various approaches to solve this problem. These approaches differ mainly due to the techniques involved in dealing with the problem, specifically the methods to represent the belief about the current pose of the robot and the different sensors used to acquire information about its surroundings. To achieve full autonomy, only onboard sensors must be used to perform the robot's localization ([YANG *et al.*, 2009](#)). Thus, one of the most common methods to predict a mobile robot's current pose is the dead reckoning technique using encoders ([BORENSTEIN; FENG, 1996; KIRIY; BUEHLER, 2002](#)). Nevertheless, the prediction error increases as the robot travels, degrading the platform's pose estimation, especially for long trajectories and even worse on slippery surfaces ([WANG, 1988](#)).

Dead reckoning is a standard method for mobile robot localization that relies on the robot's internal sensors, such as encoders, to estimate its position and orientation based on its previous known location and the robot's motion information. However, this method needs to improve on cumulative errors that may accumulate over time and cause inaccurate estimates of the robot's position and orientation. In addition, external factors such as slippery surfaces or uneven terrain can further increase the error in dead reckoning ([BORENSTEIN; FENG, 1996; KIRIY; BUEHLER, 2002](#)). Other techniques, such as landmark-based localization and visual odometry, have been developed to overcome these limitations. Landmark-based localization involves detecting and recognizing specific features or landmarks in the robot's environment and using them to estimate the robot's position and orientation, as well as visual odometry involves using visual sensors, such as cameras, to estimate the robot's motion and position by analyzing the changes in the visual information captured by the sensors ([KIRIY; BUEHLER, 2002; BETKE; GURVITS, 1997](#)). The choice of the feature extraction technique depends on the specific application requirements and constraints, such as the available sensors, the computational resources, and the accuracy and robustness requirements. However, their main disadvantages rely

on their dependence on the characteristics of the environment leading to erroneous interpretation of the provided measurements (YANG *et al.*, 2009).

The most common approach to deal with the problem of robot localization is the probabilistic one based on Bayesian estimation. Classical algorithms like the KF and EKF make stochastic assumptions about the process and sensor noises, treating them as additive Gaussian noise (JETTO; LONGHI; VENTURINI, 1999; JETTO; LONGHI; VITALI, 1999; FABRIZI *et al.*, 1998). However, it is well known that in real applications, the probability distributions are multimodal, and the system's nonlinearities also degrade the performance of these methods. Furthermore, other methods like the Monte Carlo approach and the Markov-chain-Monte-Carlo-based methods deal with the problem without assuming noise characteristics (GORDON; SALMOND; SMITH, 1993; PITT; SHEPHARD, 1999; FOX; BURGARD; THRUN, 1999; THRUN *et al.*, 2001).

Nowadays, other mainstream techniques are based on the fast laser scan matching approach, which is based on the iterative closest points (ICP) and the normal distribution transform (NCP) algorithms (KOHLBRECHER *et al.*, 2011; PENG; WANG; CHEN, 2017; LU; MILIOS, 1997; BIBER; STRASSER, 2003). However, some drawbacks are present due to issues with the beam sensor model. Modern optimization-based techniques include incremental constrained smoothing for state estimation, mainly to solve the simultaneous localization and mapping (SLAM) problem (SODHI *et al.*, 2020). Its limitation is the need for a fixed linearization point for older states, making it unsuitable for highly nonlinear problems. Also, run-time performance can be further improved by exploiting sparsity in constrained jacobians.

This work proposes advanced robust estimation techniques and output-feedback control strategies based on linear matrix inequalities (LMIs) applied to sensorless transradial upper-limb prostheses and mobile robotics. The first application case considers a hybrid control strategy that regulates the force applied to the fingertips during the closing process using an on-off and an \mathcal{H}_∞ full-state feedback controllers. This way, an \mathcal{H}_∞ observer-based filter and a full-order filter \mathcal{H}_∞ can also be implemented to estimate the states of the motor in the under-tendon-driven (UTD) system that drives each finger of the Galileo Hand, an anthropomorphic upper-limb prostheses (FAJARDO *et al.*, 2017; FAJARDO *et al.*, 2020).

Therefore, convex optimization techniques based on interior point methods are employed to solve the problems of designing LMI-based robust control strategies, one of the most potent tools for formulating control systems since it offers more flexibility in designing dynamic linear systems than traditional techniques that minimize scalar functions for optimization (OLIVEIRA; GEROMEL; BERNUSOU, 2002; GEROMEL *et al.*, 2000; SKELTON, 2021). These strategies may be computationally intensive; however, once the optimization problem is solved using a personal computer (PC) or a laptop, these

can be implemented in the embedded controller of an affordable upper limb prosthetic. Additionally, an approximate system model is used to reduce the computational load on the MCU embedded in the main controller of the prosthetic device.

The second application case proposes two alternative approaches to the probabilistic method for landmark-based mobile robot localization based on more conservative and robust techniques. These approaches also rely on robust extended \mathcal{H}_∞ estimation methods, as outlined "in prior work of" (YANG *et al.*, 2009; HUR; AHN, 2012). The critical difference between these two approaches is that they leverage the power of LMI-based robust filtering methodologies. The proposed robust estimators throughout this work can handle nonlinear systems with unknown noise inputs using general noise vectors that only require to be energy-bounded. These noise vectors are challenging to solve analytically (BOYD *et al.*, 1993). Additionally, these methods ensure that the energy gain from noise inputs to the estimation error ratio is limited by an upper-bound limit, guaranteeing solution convergence.

The first estimation approach involves designing an \mathcal{H}_∞ observer-based filter under a two-step prediction correction structure to localize the robot in a predefined environment. In contrast, the second approach uses a full-order filter \mathcal{H}_∞ , which ensures better robust performance requirements than the previous approach. Both methods require solving a convex optimization problem at each time step to determine the filter parameters that estimate the differential wheeled robot's pose. This approach offers a better solution to complex estimation problems than the analytical way finding feasible suboptimal solutions by solving the Riccati equation, as done in works (YANG *et al.*, 2009; HUR; AHN, 2012), allowing for modeling the effects of process and measurement noise in a more general and robust way (SHAKED; THEODOR, 1992; GRIGORIADIS; WATSON, 1997).

The notation used throughout this work is the following: capital and lower-case bold letters stand for matrices and vectors, respectively; the rest denote scalars. Furthermore, for vectors and matrices, $(^T)$ indicates transpose; for symmetric matrices, $\mathbf{P} > 0$ indicates that \mathbf{P} is a positive definite matrix; similarly, with $\mathbf{P} \geq 0$ denoting it as a positive semi-definite matrix. For a transfer function, $H(z)$ analytic for $z \geq 0$, $\|H(z)\|_2$ and $\|H(z)\|_\infty$ denote the standard \mathcal{H}_2 and \mathcal{H}_∞ norms, accordingly. Besides, to ease the notation of partitioned symmetric matrices, the symbol \star indicates, generically, each of its symmetric blocks.

The document is structured as follows: Chapter 2 introduces the fundamental concepts used in this dissertation, details of the hardware used to conduct the tests, and explains the dynamics of an UTD machine. Chapter 3 discusses the challenges of designing observer-based LMI-based filtering methods for a UTD-based upper-limb prosthesis and solving the landmark-based localization problem for mobile robotics without making assumptions about sensor noise and disturbances. Chapter 4 delves into the different

approaches exposed to address guaranteed-cost \mathcal{H}_∞ full-state estimation applied to assistive robotics. Chapter 5 presents the overall control strategy implemented into the Galileo Hand. Finally, the experimental results and conclusions are presented in Chapters 6 and 7, respectively.

1.1 Publications

During the course of this research, the following publications related to the topic were published and have been organized chronologically:

- FAJARDO, J., FERMAN, V., CARDONA, D., MALDONADO, G., LEMUS, A., ROHMER, E. (2020). Galileo Hand: An anthropomorphic and affordable upper-limb prosthesis. *IEEE Access*, 8, 81365-81377.
- FAJARDO, J., CARDONA, D., MALDONADO, G., NETO, A. R., ROHMER, E. (2020, July). A robust \mathcal{H}_∞ full-state observer for under-tendon-driven prosthetic hands. In *2020 IEEE/ASME International Conference on Advanced Intelligent Mechatronics (AIM)* (pp. 1555-1560). IEEE.
- FAJARDO, J., FERMAN, V., GUERRA, J., NETO, A. R., ROHMER, E. (2021, July). LMI Methods for Extended \mathcal{H}_∞ Filters for Landmark-based Mobile Robot Localization. In *2021 IEEE/ASME International Conference on Advanced Intelligent Mechatronics (AIM)* (pp. 511-517). IEEE.
- FAJARDO, J., CARDONA, D., MALDONADO, G., FERMAN, V., ROHMER, E. (2021, December). A Robust Control Strategy for Sensorless Under-Tendon-Driven Prosthetic Hands. In *2021 20th International Conference on Advanced Robotics (ICAR)* (pp. 581-587). IEEE.
- FAJARDO, J., CARDONA, D., MALDONADO, G., FERMAN, V., ROHMER, E. (2023, April). Guaranteed Cost Robust Control Strategy for Sensorless Under-Tendon-Driven Prosthetic Hands. Under review in *IEEE Transactions on Mechatronics*.

2 Fundamentals

This chapter aims to present the theoretical tools and some concepts that underpin the subsequent chapters, providing readers with key definitions for a better understanding of the methods and results obtained throughout this thesis.

2.1 Signal and System Norms

Signal and system norms are quantitative measures used to evaluate their behavior in control theory. Signal norms, such as the \mathcal{L}_1 , \mathcal{L}_2 , and \mathcal{L}_∞ norms, are used to measure the magnitude of a signal. In contrast, system norms, such as the \mathcal{H}_2 and \mathcal{H}_∞ norms, are used to evaluate a system's stability, robustness, and sensitivity. These norms play a crucial role in the analysis and design of control systems, providing engineers with a framework to optimize system performance and ensure robustness in the presence of disturbances and uncertainties (ZHOU; DOYLE; GLOVER, 1996).

2.1.1 Basic Concepts

Normed spaces are an essential concept in linear algebra and functional analysis. A norm is a mathematical object that assigns a non-negative real number, called the norm, to every vector in a vector space. Most of the concepts exposed in this section can be found in (FAIRMAN, 1998; ROMAO, 2017). A normed vector space is a vector space equipped with a norm. Formally, a norm is defined as follows:

Let \mathbb{K} be the field of scalars (either the real numbers \mathbb{R} or the complex numbers \mathbb{C} sets), and let \mathbf{X} be a vector space over \mathbb{K} . A norm on \mathbf{X} is a function $\|\cdot\| : \mathbf{X} \rightarrow \mathbb{R} \geq 0$ that satisfies the following properties for all $\mathbf{x}, \mathbf{y} \in \mathbf{X}$ and $\alpha \in \mathbb{K}$:

1. Positive definiteness: $\|\mathbf{x}\| = 0$ if and only if $\mathbf{x} = 0$.
2. Homogeneity: $\|\alpha\mathbf{x}\| = |\alpha|\|\mathbf{x}\|$.
3. Triangle inequality: $\|\mathbf{x} + \mathbf{y}\| \leq \|\mathbf{x}\| + \|\mathbf{y}\|$.

Furthermore, a Banach space is a complete normed vector space. In other words, it is a vector space \mathbf{X} equipped with a norm $\|\cdot\|$ such that every Cauchy sequence in \mathbf{X} converges to an element in \mathbf{X} . For example, the normed vector space $C[a, b]$ is a Banach space.

Considering \mathbf{X} a normed vector space, as well as a sequence $\{\mathbf{x}_n\}$ contained in \mathbf{X} . We say this sequence is convergent in \mathbf{X} , that is $\mathbf{x}_n \rightarrow \mathbf{x}$, if $\|\mathbf{x}_n - \mathbf{x}\| \rightarrow 0$, for some

$x \in \mathbf{X}$. In addition, $\{x_n\}$ is a Cauchy sequence if $\|x_n - x_m\| \rightarrow 0$ for natural numbers $n, m \rightarrow \infty$.

Accordingly, the spaces $\ell_p[0, \infty)$, for $p \in \mathbb{N}$ such that $0 < p < \infty$. Thus, for each value of p , $\ell_p[0, \infty)$ represents the set of sequences x_n with norm defined as follows

$$\|x\|_p = \left(\sum_{i=0}^{\infty} |x_i|^p \right)^{1/p}$$

If $p = \infty$, the space $\ell_\infty[0, \infty)$ represents the set of limited sequences with norm defined with the following equation:

$$\|x\|_\infty = \sup_i |x_i|$$

Finally, the absolute value operator, denoted by $|\cdot|$, can be replaced with the corresponding norm to yield a more appropriate mathematical representation in vector or matrix-based spaces. Additionally, for vector spaces equipped with an inner product, a norm can be induced by the dot product, which is defined as follows.

$$\|\mathbf{x}\| = \sqrt{\langle \mathbf{x}, \mathbf{x} \rangle}$$

2.1.2 Hilbert Spaces

Hilbert spaces are a type of complete inner product space (a special case of Banach spaces) and are fundamental objects of study in functional analysis and mathematical physics. For example, a Hilbert Space \mathbf{H} is a vector space over the complex field \mathbb{C} that is equipped with an inner product $\langle \cdot, \cdot \rangle : \mathbf{H} \times \mathbf{H} \rightarrow \mathbb{C}$ that satisfies the following properties for all $x, y, z \in \mathbf{H}$ and $\alpha, \beta \in \mathbb{C}$:

1. Linearity in the first argument: $\langle \alpha \mathbf{x} + \beta \mathbf{y}, \mathbf{z} \rangle = \alpha \langle \mathbf{x}, \mathbf{z} \rangle + \beta \langle \mathbf{y}, \mathbf{z} \rangle$.
2. Conjugate symmetry: $\langle \mathbf{x}, \mathbf{y} \rangle = \overline{\langle \mathbf{y}, \mathbf{x} \rangle}$.
3. Positive-definiteness: $\langle \mathbf{x}, \mathbf{x} \rangle \geq 0$, with equality only if $\mathbf{x} = 0$.

The norm induced by the inner product turns \mathbf{H} into a metric space, which is complete because every Cauchy sequence converges to an element in \mathbf{H} . This completeness property is crucial for many applications, such as studying infinite-dimensional systems and developing quantum mechanics. Hilbert Spaces also provide a framework for analyzing Fourier series, wavelets, and other mathematical objects. The mathematical properties of Hilbert Spaces make them an essential tool for understanding and solving problems in various fields, such as physics and engineering.

In addition, as an example of finite-dimensional Hilbert spaces, consider $\mathbb{C}^{n \times m}$ with the following inner product.

$$\langle \mathbf{A}, \mathbf{B} \rangle = \text{Tr}(\mathbf{A}^* \mathbf{B}) = \sum_{i=1}^n \sum_{j=1}^m a_{ij}^* b_{ij}, \forall \mathbf{A}, \mathbf{B} \in \mathbb{C}^{n \times m}$$

where a_{ij} and b_{ij} are elements of the matrices \mathbf{A} and \mathbf{B} .

The space $\ell_2(-\infty, \infty)$ equipped with the dot product in Euclidean space is a Hilbert space of infinite dimension. Similarly, $\mathcal{L}_2(I)$ is the space formed by quadratically integrable functions on an interval $I \subset \mathbb{R}$ with an inner product defined by

$$\langle f, g \rangle = \int_I f(t)^* g(t) dt$$

where $f(t), g(t) \in \mathcal{L}_2(I)$. On the other hand, if the functions are vectors or matrices, the inner product is defined by

$$\langle f, g \rangle = \int_I \text{Tr}(f(t)^* g(t)) dt$$

In addition, the vector spaces $\mathcal{L}_2(-\infty, +\infty)$, $\mathcal{L}_2[0, +\infty)$ and $\mathcal{L}_2(-\infty, 0]$ receive the following notation \mathcal{L}_2 , \mathcal{L}_{2+} and \mathcal{L}_{2+}^\perp , correspondingly ([ROMAO, 2017](#)). Therefore, for a Hilbert space, \mathcal{H} , consider a subset $\mathcal{S}_1 \subset \mathcal{H}$, the orthogonal complement of \mathcal{S}_1 in \mathcal{H} , called \mathcal{S}_1^\perp is defined as follows.

$$\mathcal{S}_1^\perp = \{\mathbf{x} \in \mathcal{H} : \langle \mathbf{x}, \mathbf{y} \rangle = 0, \forall \mathbf{y} \in \mathcal{S}_1\}$$

2.1.3 Hardy Spaces \mathcal{H}_2 and \mathcal{H}_∞

Hardy spaces are a family of function spaces that arise naturally in complex and harmonic analyses. In this section, spaces formed by complex functions of complex variables are approached. Specifically, $S \subset \mathbb{C}$, an open subset, and a function $f : S \rightarrow \mathbb{C}$ are considered. The function f is considered analytic at a point z_0 if it is differentiable at z_0 and in a neighborhood of z_0 . Furthermore, it is recognized from the complex variable theory that a function is analytic at a point z_0 if and only if it has a Taylor series representation at z_0 ([BROWN; CHURCHILL, 2009](#)). Moreover, the function f is analytic on S if, for every point $z \in S$, the function is analytic on z .

Let $S \subset \mathbb{C}$ be an open subset. The finite-dimensional space formed by functions $F : S \rightarrow \mathbb{C}$ such that

$$\int_{-\infty}^{+\infty} \text{Tr}(F(j\omega)^* F(j\omega)) d\omega < +\infty$$

equipped with an inner product defined by

$$\langle F, G \rangle = \frac{1}{2\pi} \int_{-\infty}^{+\infty} \text{Tr}(F(j\omega)^* G(j\omega)) d\omega$$

and induced norm that is given by

$$\|F\|_2 = \sqrt{\langle F, F \rangle}$$

is denominated an \mathcal{L}_2 space.

Thus, the subset \mathcal{H}_2 is the set of analytic functions in $\text{Re}(s) > 0$. The orthogonal complement of \mathcal{H}_2 , defined as \mathcal{H}_2^\perp , is formed by the set of analytic matrices in the left half plane. This way, from the point of view of systems theory, transfer matrices associated with stable and causal dynamic systems belong to the \mathcal{H}_2 space. On the other hand, non-causal and anti-stable systems generate transfer matrices that belong to \mathcal{H}_2^\perp .

Therefore, being a Hilbert space, the \mathcal{H}_2 space is equipped with an inner product and a norm defined as

$$\|F\|_2^2 = \sup_{\sigma>0} \left\{ \frac{1}{2\pi} \int_{-\infty}^{+\infty} \text{Tr}(F(\sigma + j\omega)^* F(\sigma + j\omega)) d\omega \right\} \quad (2.1)$$

where $F \in \mathcal{H}_2$ (ZHOU; DOYLE; GLOVER, 1996), the following expression is equivalent to Eq. (2.1).

$$\|F\|_2^2 = \frac{1}{2\pi} \int_{-\infty}^{+\infty} \text{Tr}(F(j\omega)^* F(j\omega)) d\omega \quad (2.2)$$

Since \mathcal{L}_2 , \mathcal{H}_2 , and \mathcal{H}_2^\perp spaces in the frequency domain are related to the time domain spaces previously introduced in this chapter. Note that if a function (matrix, vector, or scalar) in time $f(t) \in \mathcal{L}_2(\infty, +\infty)$, then the bilateral Laplace transform exists, and the imaginary axis as belonging to the convergence region. Therefore, defining $F(s) = \mathbb{L}\{f(t)\}$, with $F(s)$ as the Laplace transform of the function $f(t)$, and $\mathbb{L} : \mathcal{L}_2(\infty, +\infty) \rightarrow \mathcal{L}_2$ as a linear transformation between the spaces $\mathcal{L}_2(\infty, +\infty)$, in the time and frequency domains. Thus, using Parseval's theorem, the following expression is obtained.

$$\|F(s)\|_2 = \|f(t)\|_2$$

therefore, the spaces $\mathcal{L}_2(\infty, +\infty)$, \mathcal{L}_{2+} , and \mathcal{L}_{2+}^\perp are related by an isomorphic linear transformation with the spaces in the frequency domain \mathcal{L}_2 , respectively \mathcal{H}_2 and \mathcal{H}_2^\perp .

Furthermore, it should be noted that the set \mathcal{L}_∞ is a Banach space, meaning it is a complete normed vector space. However, it cannot be classified as a Hilbert space since

it lacks an inner product. This space comprises complex functions of complex variables bounded on the imaginary axis, which is bounded as follows.

$$\operatorname{ess\,sup}_{\omega \in \mathbb{R}} \bar{\sigma}(F(j\omega)) < \infty,$$

where $\bar{\sigma}$ is the maximum singular value of matrix $F(j\omega)$ with norm

$$\|F(s)\|_{\infty} = \operatorname{ess\,sup}_{\omega \in \mathbb{R}} \bar{\sigma}(F(j\omega)). \quad (2.3)$$

For the case in which $F(j\omega)$ is a rational function, the following expression is equivalent

$$\|F(s)\|_{\infty} = \sup_{\omega \in \mathbb{R}} \bar{\sigma}(F(j\omega)) \quad (2.4)$$

The space \mathcal{L}_{∞} is associated with two subspaces: \mathcal{H}_{∞} and \mathcal{H}_{∞}^- . \mathcal{H}_{∞} is composed of analytic functions that are bounded on the imaginary axis and defined on the region $\operatorname{Re}(s) > 0$, while \mathcal{H}_{∞}^- consists of analytic functions that are bounded on the imaginary axis and defined on the region $\operatorname{Re}(s) < 0$. The norm on \mathcal{H}_{∞} is given by:

$$\|F(s)\|_{\infty} = \operatorname{ess\,sup}_{\sigma > 0} \bar{\sigma}(F(s)) = \operatorname{ess\,sup}_{\omega \in \mathbb{R}} \bar{\sigma}(F(j\omega)), \quad (2.5)$$

while \mathcal{H}_{∞}^- is equipped with a norm given by:

$$\|F(s)\|_{\infty} = \operatorname{ess\,sup}_{\sigma < 0} \bar{\sigma}(F(s)) = \operatorname{ess\,sup}_{\omega \in \mathbb{R}} \bar{\sigma}(F(j\omega)), \quad (2.6)$$

This way, if $F(s) \in \mathcal{H}_{\infty}$ or $F(s) \in \mathcal{H}_{\infty}^-$ is a rational eigenfunction, then the norm $\|F(s)\|_{\infty} = \sup_{\omega \in \mathbb{R}} \bar{\sigma}(F(j\omega))$.

The \mathcal{H}_{∞} norm has an important interpretation in the study of time-invariant linear systems, as it represents the value of the maximum gain, called \mathcal{L}_2 gain, between the input and output energy when considering input signals belonging to the \mathcal{L}_2 space.

Theorem 2.1.1. Let $H(s) \in \mathcal{L}_{\infty}$ be the transfer matrix of a linear system and time-invariant of dimension $p \times q$. $\|H\|_{\infty}$ represents the maximum output energy gain for the input when applying quadratically integrable input signals belonging to \mathcal{L}_2 space.

The proof of the theorem can be found in (ZHOU; DOYLE; GLOVER, 1996).

In addition, the following properties associated with the rational handover matrices belonging to the \mathcal{L}_{∞} space are essential in the context of this work.

1. If $H(s) \in \mathcal{L}_\infty$, then $\{Y(s) : Y(s) = H(s)U(s) : U(s) \in \mathcal{L}_2\} \subset \mathcal{L}_2$;
2. If $H(s) \in \mathcal{H}_\infty$, then $\{Y(s) : Y(s) = H(s)U(s) : U(s) \in \mathcal{H}_2\} \subset \mathcal{H}_2$;
3. If $H(s) \in \mathcal{H}_\infty^-$, then $\{Y(s) : Y(s) = H(s)U(s) : U(s) \in \mathcal{H}_2^\perp\} \subset \mathcal{H}_2^\perp$.

These concepts refer to the rational matrices that belong to the space \mathcal{H}_∞ , and, therefore, it is assumed that $\|H(s)\|_\infty \leq \gamma$ implies that $H(s)$ is a transfer matrix of a causal and analytic system in the right half plane and, therefore, BIBO (Bounded input bounded output) stable.

2.1.4 Linear Matrix Inequalities (LMIs)

LMIs are a powerful tools in the field of control theory for designing controllers and analyzing the stability of dynamic systems. An LMI is an inequality that involves matrices and can be written in the form:

$$F(\mathbf{x}) = \sum_{i=0}^n \mathbf{x}_i F_i \preceq \mathbf{0},$$

where $F(\mathbf{x})$ is a function, such as a matrix-valued function of the variable \mathbf{x} . The notation " \preceq " means "less than or equal to in the sense of positive semidefiniteness", i.e., $\mathbf{A} \preceq \mathbf{0}$ if and only if $\mathbf{x}^T \mathbf{A} \mathbf{x} \leq 0$ for all vectors \mathbf{x} (GHAOUI; NICULESCU, 2000).

LMIs provide a general framework for modeling various constraints and objectives in control problems, such as robust stability, performance, and robustness to disturbances and uncertainties. They can be used to formulate convex optimization problems, which can be efficiently solved using numerical algorithms. One of the main advantages of LMIs is their ability to handle complex nonlinearities and uncertainties in a systematic and tractable manner. By representing nonlinear functions and uncertainties as parameter-dependent matrices, it is often possible to transform a nonlinear control problem into an LMI problem, which can be solved using existing convex optimization software (GHAOUI; NICULESCU, 2000).

In addition to their use in control theory, LMIs have applications in many other areas of science and engineering, such as signal processing, communications, and optimization. The development of efficient numerical algorithms for solving LMI problems has led to their widespread use in practice.

2.1.5 Finsler's Lemma

Finsler's Lemma is a fundamental result in differential geometry composed of four algebraic equivalences (OLIVEIRA; SKELTON, 2007; SKELTON; IWASAKI; GRIGORIADIS, 2013). It provides a powerful way to compute the derivative of a function

defined on a Riemannian manifold and has numerous applications in physics and engineering. In particular, Finsler's Lemma is an essential tool in designing control systems using LMIs. By leveraging Finsler's Lemma, control engineers can optimize the performance of control systems subject to constraints and uncertainties, leading to more robust and reliable systems.

Lemma 2.1.2. Consider a Hermitian matrix $\mathbf{Q} \in \mathbb{C}^{n \times n}$ and a matrix $\mathbf{B} \in \mathbb{C}^{m \times n}$ with $m < n$ and $\text{rank}(\mathbf{B}) = r < n$. Then, the following conditions are equivalent.

- i) $\mathbf{z}^* \mathbf{Q} \mathbf{z} < 0, \forall \mathbf{z}$ s.t. $\mathbf{B} \mathbf{z} = 0$.
- ii) $\mathbf{B}^{\perp*} \mathbf{Q} \mathbf{B}^{\perp} \prec 0$.
- iii) $\exists \mu \in \mathbb{R}, \mu > 0 : \mathbf{Q} - \mu \mathbf{B}^* \mathbf{B} \prec 0$.
- iv) $\exists \mathbf{X} \in \mathbb{C}^{n \times m} : \mathbf{Q} + \mathbf{X} \mathbf{B} + \mathbf{B}^* \mathbf{X}^* \prec 0$.

The proof of the lemma can be found in (OLIVEIRA; SKELTON, 2007; SKELTON; IWASAKI; GRIGORIADIS, 2013).

2.1.6 Projection Lemma

The Projection Lemma is a fundamental mathematical result with numerous applications, including in the control systems engineering field. This lemma provides alternative methods for testing the negativity of a matrix expression in two subspaces simultaneously, which is a critical step in the analysis of linear and time-invariant dynamical systems. Specifically, the Projection Lemma enables the development of alternative conditions for calculating the \mathcal{H}_2 and \mathcal{H}_{∞} norms of these systems, which are important measures of their performance and stability. By leveraging the Projection Lemma, control engineers can develop more efficient and accurate methods for analyzing the behavior of dynamical systems and designing control systems that ensure stability and optimal performance.

Lemma 2.1.3. Consider $\mathbf{x} \in \mathbb{C}^n$, $\mathbf{Q} = \mathbf{Q} \in \mathbb{C}^{n \times n}$, $\mathbf{S} \in \mathbb{C}^{m \times n}$ and $\mathbf{K} \in \mathbb{R}^{p \times n}$ s.t. $\text{rank}(\mathbf{S}) < n$ and $\text{rank}(\mathbf{K}) < n$. Then, the following conditions are equivalent:

- i) $\mathbf{S}^{\perp*} \mathbf{Q} \mathbf{S}^{\perp} \prec 0$ and $\mathbf{K}^{\perp*} \mathbf{Q} \mathbf{K}^{\perp} \prec 0$.
- ii) $\exists \mu \in \mathbb{R}, \mu > 0 : \mathbf{Q} - \mu \mathbf{S}^* \mathbf{S} \prec 0$ and $\mathbf{Q} - \mu \mathbf{K}^* \mathbf{K} \prec 0$.
- iii) $\exists \mathbf{X} \in \mathbb{C}^{p \times m} : \mathbf{Q} + \mathbf{K}^* \mathbf{X} \mathbf{S} + \mathbf{S}^* \mathbf{X}^* \mathbf{K} \prec 0$.

The proof of the lemma can be found in (BOYD *et al.*, 1994; SKELTON; IWASAKI; GRIGORIADIS, 2013).

2.2 \mathcal{H}_2 and \mathcal{H}_∞ Norms using LMIs

This section presents the calculation of \mathcal{H}_2 and \mathcal{H}_∞ norms of transfer matrices associated with linear and time-invariant dynamic systems using LMIs. Most of the concepts described in this section are in (ROMAO, 2017).

Consider a state-space system

$$\delta[\mathbf{x}] = \mathbf{Ax} + \mathbf{Bu} \quad (2.7)$$

$$\mathbf{y} = \mathbf{Cx} + \mathbf{Du}$$

with $\mathbf{A} \in \mathbb{R}^{n \times n}$, $\mathbf{B} \in \mathbb{R}^{n \times r}$, $\mathbf{C} \in \mathbb{R}^{p \times n}$ and $\mathbf{D} \in \mathbb{R}^{p \times r}$, where $\mathbf{x} \in \mathbb{R}^n$ is the state vector, $\mathbf{u} \in \mathbb{R}^r$ is the input vector, $\mathbf{y} \in \mathbb{R}^p$ is the output vector, $\delta[\mathbf{x}]$ is the derivative operator, $\dot{\mathbf{x}}(t)$, for continuous systems, or time advance, $\mathbf{x}[k+1]$, for discrete systems. In addition, consider

$$H(\zeta) = \mathbf{C} (\zeta \mathbf{I} - \mathbf{A})^{-1} \mathbf{B} + \mathbf{D} \quad (2.8)$$

the rational transfer matrix associated with the system described in Eq. (2.7), where ζ is the Laplace variable s in the case of continuous systems or the complex variable z for discrete systems.

2.2.1 \mathcal{H}_2 Norm

To derive conditions using LMIs for calculating the \mathcal{H}_2 norm of the system described in Eq. (2.7), it is important to note that the model represents causal systems in the continuous case, meaning their impulse response $h(t)$ is zero for $t < 0$. As a result, the corresponding transfer matrices described in Eq. (2.8) belong to the space \mathcal{H}_2 if and only if $h(t) \in \mathcal{L}_2[0, +\infty)$. This condition implies that matrix \mathbf{A} is Hurwitz, and must have all eigenvalues having negative real part, and matrix \mathbf{D} is zero (ZHOU; DOYLE; GLOVER, 1996).

In the discrete case, $h[k] \in \mathcal{L}_2[0, +\infty)$ if and only if the matrix \mathbf{A} is Schur stable, and must have all eigenvalues lying within the unit circle of the complex plane. These conditions provide necessary and sufficient conditions for the \mathcal{H}_2 norm of the system, which can be calculated using LMIs for continuous and discrete systems. Therefore, understanding the nature of causal systems in the continuous case and Schur stability in the discrete case is crucial to deriving quadratic stability conditions using LMIs for calculating the \mathcal{H}_2 norm of the system, as presented by (ZHOU; DOYLE; GLOVER, 1996).

At this point on, when mentioning the \mathcal{H}_2 norm of a transfer matrix, it is implicitly assumed that the restrictions above are imposed on the model described in Eq. (2.7).

2.2.1.1 Continuous-time Systems

Considering the expression described in Eq. (2.2), if the transfer matrix $H(s)$ described in Eq. (2.8) belongs to the space \mathcal{H}_2 , the norm is defined by

$$\|H(s)\|_2^2 = \frac{1}{2\pi} \int_0^{+\infty} \text{Tr}(H(j\omega)^* H(j\omega)) d\omega = \int_0^{+\infty} \text{Tr}(h(t)h^*(t)) dt, \quad (2.9)$$

where

$$h(t) = \begin{cases} \mathbf{C}e^{\mathbf{A}t}\mathbf{B}, & t \geq 0, \\ 0, & t < 0. \end{cases}$$

Therefore, by substituting the expression for $h(t)$ in Eq. (2.9), the following result for the calculation of the \mathcal{H}_2 norm of the continuous system described in Eq. (2.8) is obtained.

Lemma 2.2.1. Consider the controllable and observable continuous system described by Eq. (2.8), where matrix \mathbf{A} is Hurwitz and matrix $\mathbf{D} = \mathbf{0}$. The value of the norm \mathcal{H}_2 (squared) of the transfer matrix $H(s)$ is given by

$$\|H(s)\|_2^2 = \text{Tr}(\mathbf{B}^T \mathbf{P} \mathbf{B}) = \text{Tr}(\mathbf{C} \mathbf{W} \mathbf{C}^T) \quad (2.10)$$

where $\mathbf{P} = \mathbf{P}^T \succ \mathbf{0}$ and $\mathbf{W} = \mathbf{W}^T \succ \mathbf{0}$ are the solutions for the following quadratic Lyapunov equations for continuous systems:

$$\mathbf{A}^T \mathbf{P} + \mathbf{P} \mathbf{A} + \mathbf{C}^T \mathbf{C} = \mathbf{0}, \quad (2.11)$$

$$\mathbf{A} \mathbf{W} + \mathbf{W} \mathbf{A}^T + \mathbf{B} \mathbf{B}^T = \mathbf{0}. \quad (2.12)$$

\mathbf{P} and \mathbf{W} matrices called the observability and controllability gramians, respectively.

These equations, (2.11)–(2.12), have unique, symmetric, positive definite solutions if matrix \mathbf{A} is Hurwitz and if (\mathbf{A}, \mathbf{C}) is observable, or if (\mathbf{A}, \mathbf{B}) is controllable (properties of the solution of the Lyapunov equation). Therefore, using the result of Lemma 2.2.1, the norm \mathcal{H}_2 of the system described in Eq. (2.7) can be calculated by the expression described in (2.10) from the solution of the Eqs. (2.11) or (2.12).

Alternatively, using the results presented by (RAN; VREUGDENHIL, 1988), the calculation of the \mathcal{H}_2 norm of a system as the one described in (2.7) can be formulated through a convex optimization problem with LMIs constraints (OLIVEIRA, 1999). However, this methodology is not considered for filtering design in posterior sections.

2.2.1.2 Discrete-time Systems

In the same way as the continuous systems case, the following expression calculates the \mathcal{H}_2 norm of the discrete transfer matrix described in Eq. (2.8).

$$\|H(z)\|_2^2 = \frac{1}{2\pi} \int_{-\pi}^{\pi} \text{Tr} \left(H(e^{j\omega})^* H(e^{j\omega}) \right) d\omega = \sum_{k=0}^{+\infty} \text{Tr} (h[k]^* h[k]) \quad (2.13)$$

where the sequence $h[k]$ is the impulse response of the discrete system described in Eq. (2.7) given by

$$h[k] = \begin{cases} \mathbf{C}\mathbf{A}^{k-1}\mathbf{B}, & k > 0, \\ \mathbf{D}, & k = 0. \end{cases}$$

Therefore, substituting $h[k]$ into Eq. (2.13), the following result is obtained (analogous to the Lemma 2.2.1 for continuous systems).

Lemma 2.2.2. Considering the discrete system described in Eq. (2.7), with a stable \mathbf{A} Schur matrix. Then,

$$\|H(z)\|_2^2 = \text{Tr}(\mathbf{B}^T \mathbf{P} \mathbf{B} + \mathbf{D}^T \mathbf{D}) = \text{Tr}(\mathbf{C} \mathbf{W} \mathbf{C}^T + \mathbf{D} \mathbf{D}^T) \quad (2.14)$$

where $\mathbf{P} = \mathbf{P}^T \succ 0$ and $\mathbf{W} = \mathbf{W}^T \succ 0$ are the solutions for the following quadratic Lyapunov equations for discrete systems:

$$\mathbf{A}^T \mathbf{P} \mathbf{A} - \mathbf{P} + \mathbf{C}^T \mathbf{C} = \mathbf{0}, \quad (2.15)$$

$$\mathbf{A} \mathbf{W} \mathbf{A}^T - \mathbf{W} + \mathbf{B} \mathbf{B}^T = \mathbf{0}. \quad (2.16)$$

\mathbf{P} and \mathbf{W} matrices called the observability and controllability gramians, respectively.

Similarly to the continuous case, as matrix \mathbf{A} is Schur stable, the matrices \mathbf{P} and \mathbf{W} are positive definite. The \mathcal{H}_2 norm for discrete systems can be determined using LMIs ([OLIVEIRA, 1999](#)). However, this methodology is not considered for filtering design in posterior sections.

2.2.2 \mathcal{H}_∞ Norm

Even though Eqs. (2.10-2.12) and (2.13-2.16) are crucial for comprehending optimal and resilient control, the focus of this study is mainly on computing the \mathcal{H}_∞ norm of filter-based estimators for discrete systems, especially since do not take any assumptions about noise. Nonetheless, the continuous systems will be considered before delving into the discrete systems case.

2.2.2.1 Continuous-time Systems

Considering dynamic systems whose transfer matrices are rational and that belong to the \mathcal{H}_∞ space (causal and analytic in the closed right half-plane), the transfer matrix is bounded on the imaginary axis and has a norm \mathcal{H}_∞ given by

$$\|H(s)\|_\infty = \sup_{\omega>0} \bar{\sigma}(H(j\omega)).$$

Therefore, from the result of Theorem 2.1.1 (as well as the discrete equivalent), the following result is established for calculating the \mathcal{H}_∞ norm of the linear and time-invariant system given in Eq. (2.7).

Lemma 2.2.3. Considering the time-invariant linear continuous system given in Eq. (2.7). The following conditions are equivalent:

i) $\|H(s)\|_\infty < \gamma$.

ii) There is a symmetric matrix $0 \prec \mathbf{P} \in \mathbb{R}^{n \times n}$ such that

$$\begin{bmatrix} \mathbf{A}^T \mathbf{P} + \mathbf{P} \mathbf{A} & \mathbf{P} \mathbf{B} & \mathbf{C}^T \\ \mathbf{B}^T \mathbf{P} & -\mathbf{I} & \mathbf{D}^T \\ \mathbf{C} & \mathbf{D} & -\gamma^2 \mathbf{I} \end{bmatrix} \prec \mathbf{0}. \quad (2.17)$$

Proof. From the Theorem 2.1.1, it is known that $\|H(s)\|_\infty < \gamma$ if, and only if,

$$\|y(t)\|_2^2 \leq \gamma^2 \|u(t)\|_2^2. \quad (2.18)$$

Note that if $H(s)$ is rational and analytic in the closed right half plane is the same as guaranteeing that the matrix \mathbf{A} in the system described in (2.7) is Hurwitz. That is, there exists a symmetric matrix $\mathbf{P} \succ \mathbf{0}$ such that the derivative of the quadratic Lyapunov function on the states, $v(x(t)) = x(t)^T \mathbf{P} x(t)$, is negative as follows:

$$x(t)^T (\mathbf{A}^T \mathbf{P} + \mathbf{P} \mathbf{A}) x(t) + 2u(t)^T \mathbf{B}^T \mathbf{P} x(t) < 0. \quad (2.19)$$

This way, the following inequality is obtained by rewriting Eq. (2.18) using dot products and adding the resulting inequality with Eq. (2.20).

$$x(t)^T (\mathbf{A}^T \mathbf{P} + \mathbf{P} \mathbf{A}) x(t) + 2u(t)^T \mathbf{B}^T \mathbf{P} x(t) + y(t)^T y(t) - \gamma^2 u(t)^T u(t) < 0. \quad (2.20)$$

Thus, by substituting the expression for $y(t)$ from Eq. (2.7) into Eq. (2.20), the following expression is obtained.

$$\begin{bmatrix} x(t)^T u(t)^T \end{bmatrix} \begin{bmatrix} \mathbf{A}^T \mathbf{P} + \mathbf{P} \mathbf{A} + \mathbf{C}^T \mathbf{C} & \mathbf{P} \mathbf{B} + \mathbf{C}^T \mathbf{C} \\ \mathbf{B}^T \mathbf{P} + \mathbf{D}^T \mathbf{C} & \mathbf{D}^T \mathbf{D} - \gamma^2 \mathbf{I} \end{bmatrix} \begin{bmatrix} x(t) \\ u(t) \end{bmatrix} < 0. \quad (2.21)$$

Since the inequality described in (2.21) must be valid for all $t \geq 0$, $\forall x(t)$ as well as for $\forall u(t)$, then

$$\begin{bmatrix} \mathbf{A}^T \mathbf{P} + \mathbf{P} \mathbf{A} + \mathbf{C}^T \mathbf{C} & \mathbf{P} \mathbf{B} + \mathbf{C}^T \mathbf{C} \\ \mathbf{B}^T \mathbf{P} + \mathbf{D}^T \mathbf{C} & \mathbf{D}^T \mathbf{D} - \gamma^2 \mathbf{I} \end{bmatrix} \prec \mathbf{0}. \quad (2.22)$$

Therefore, the result presented in Eq. (2.17) follows by applying the Schur complement to the expression described in Eq. (2.22). This way, the value of the norm \mathcal{H}_∞ can be obtained from the following convex optimization problem

$$\|H(s)\|_{\infty}^2 = \min \gamma^2$$

subjected to the LMI described in Eq. (2.17).

2.2.2.2 Discrete-time Systems

In the discrete case, systems are considered in which the transfer matrix is limited to the unit circle, with norm \mathcal{H}_{∞} given by

$$\|H(z)\|_{\infty} = \sup_{\omega \in [-\pi, \pi]} \bar{\sigma}(H(e^{j\omega})).$$

Lemma 2.2.4. Considering the discrete system represented by Eq. (2.7), the following conditions are equivalent.

- i) $\|H(z)\|_{\infty} < \gamma$.
- ii) There exist a symmetric matrix $0 \prec \mathbf{P} \in \mathbb{R}^{n \times n}$ such that

$$\begin{bmatrix} \mathbf{A}^T \mathbf{P} \mathbf{A} - \mathbf{P} & \mathbf{A}^T \mathbf{P} \mathbf{B} & \mathbf{C}^T \\ \mathbf{B}^T \mathbf{P} \mathbf{A} & \mathbf{B}^T \mathbf{P} \mathbf{B} - \gamma^2 \mathbf{I} & \mathbf{D}^T \\ \mathbf{C} & \mathbf{D} & -\mathbf{I} \end{bmatrix} \prec 0. \quad (2.23)$$

The proof of this Lemma is carried out in the same way as in the continuous case. In this way, the norm \mathcal{H}_{∞} is obtained by solving the following convex optimization problem:

$$\|H(z)\|_{\infty}^2 = \min \gamma^2$$

subjected to the LMI described in Eq. (2.23).

2.3 Bayesian Filters

Most of the concepts in this section can be found in (THRUN, 2002). Bayesian filters are a class of probabilistic algorithms used for estimating the state of a system based on noisy measurements. Given the available measurements, these filters recursively update the probability distribution over the system state.

The basic idea behind a Bayesian filter is to maintain a probability distribution $bel(\mathbf{x}_t)$ over the system's state at time t , based on all the available measurements up to that point. This distribution is called the belief state, representing the best estimate of the system state given the available information. The belief state is updated recursively using the Bayes rule:

$$bel(\mathbf{x}_t) = \frac{p(\mathbf{z}_t|\mathbf{x}_t) \cdot \int p(\mathbf{x}_t|\mathbf{x}_{t-1}, \mathbf{u}_t) \cdot bel(\mathbf{x}_{t-1}) d\mathbf{x}_{t-1}}{p(\mathbf{z}_t)}$$

where $p(\mathbf{z}_t|\mathbf{x}_t)$ is the likelihood function, representing the probability of observing the measurement \mathbf{z}_t given the state \mathbf{x}_t . The integral $\int p(\mathbf{x}_t|\mathbf{x}_{t-1}, \mathbf{u}_t) \cdot bel(\mathbf{x}_{t-1}) d\mathbf{x}_{t-1}$ is the prediction step, which represents the probability of the state at time t given the state at time $t - 1$ and the control input \mathbf{u}_t , and $p(\mathbf{z}_t)$ is the normalization constant, which ensures that the belief state is a valid probability distribution.

The Bayesian filter can be divided into two main steps: the prediction step and the measurement update step. In the prediction step, the belief state is updated based on the control input \mathbf{u}_t and the transition model $p(\mathbf{x}_t|\mathbf{x}_{t-1}, \mathbf{u}_t)$, which represents the probability of the state at time t given the state at time $t - 1$ and the control input \mathbf{u}_t :

$$\overline{bel}(\mathbf{x}_t) = \int p(\mathbf{x}_t|\mathbf{x}_{t-1}, \mathbf{u}_t) \cdot bel(\mathbf{x}_{t-1}) d\mathbf{x}_{t-1}$$

where $\overline{bel}(\mathbf{x}_t)$ is the predicted belief state.

In the measurement update step, the belief state is updated based on the measurement \mathbf{z}_t and the likelihood function $p(\mathbf{z}_t|\mathbf{x}_t)$:

$$bel(\mathbf{x}_t) = \frac{p(\mathbf{z}_t|\mathbf{x}_t) \cdot \overline{bel}(\mathbf{x}_t)}{p(\mathbf{z}_t)}$$

where $bel(\mathbf{x}_t)$ is the updated belief state.

Many applications use Bayesian filters, such as robot localization, object tracking, and signal processing. They are particularly useful when the system's state is not directly observable and must be inferred from noisy measurements.

2.3.1 Kalman Filter

KF is a mathematical algorithm widely used in control systems and robotics to estimate the state of a dynamic system based on noisy measurements. The KF is based on the principle of Bayesian inference, which allows us to update our beliefs about the state of a system as we receive new information.

This filter assumes that the system's state can be modeled as a linear function of the previous state plus some Gaussian noise. The state of the system is represented as a vector \mathbf{x}_k at time k , and the linear function models the system dynamics:

$$\mathbf{x}_k = \mathbf{F}_k \mathbf{x}_{k-1} + \mathbf{B}_k \mathbf{u}_k + \mathbf{w}_k$$

where \mathbf{F}_k is the state transition matrix, \mathbf{B}_k is the control input matrix, \mathbf{u}_k is the control input vector, and \mathbf{w}_k is the process noise vector, which is assumed to be Gaussian with mean zero and covariance matrix \mathbf{Q}_k .

At each time step k , the KF receives a noisy measurement of the system's state, represented as a vector \mathbf{z}_k . The measurement is modeled as a linear function of the true state plus some Gaussian noise:

$$\mathbf{z}_k = \mathbf{H}_k \mathbf{x}_k + \mathbf{v}_k$$

where \mathbf{H}_k is the measurement matrix and \mathbf{v}_k is the measurement noise vector, which is assumed to be Gaussian with mean zero and covariance matrix \mathbf{R}_k .

The KF estimates the true state of the system by combining the prior estimate with the current measurement. The prior estimate is obtained by propagating the previous estimate through the system dynamics. This filter uses the covariance matrices \mathbf{P}_{k-1} and \mathbf{Q}_k to estimate the covariance matrix of the prior estimate:

$$\hat{\mathbf{x}}_{k|k-1} = \mathbf{F}_k \hat{\mathbf{x}}_{k-1|k-1} + \mathbf{B}_k \mathbf{u}_k$$

$$\mathbf{P}_{k|k-1} = \mathbf{F}_k \mathbf{P}_{k-1|k-1} \mathbf{F}_k^T + \mathbf{Q}_k$$

where $\hat{\mathbf{x}}_{k-1|k-1}$ and $\mathbf{P}_{k-1|k-1}$ are the estimated state and covariance matrix at the previous time step, respectively.

The KF then combines the prior estimate with the current measurement to obtain the posterior estimate of the state and also uses the covariance matrices $\mathbf{P}_{k|k-1}$ and \mathbf{R}_k to estimate the covariance matrix of the posterior estimate:

$$\mathbf{K}_k = \mathbf{P}_{k|k-1} \mathbf{H}_k^T \left(\mathbf{H}_k \mathbf{P}_{k|k-1} \mathbf{H}_k^T + \mathbf{R}_k \right)^{-1}$$

2.3.2 Extended Kalman Filter

The EKF is a variant of the Kalman Filter that can handle nonlinear system dynamics and nonlinear measurement functions. The EKF works by approximating the nonlinear functions with linear functions using a first-order Taylor series expansion.

This filter assumes that the system's state can be modeled as a nonlinear function of the previous state plus some Gaussian noise. The state of the system is represented as a vector \mathbf{x}_k at time k , and the nonlinear function models the system dynamics:

$$\mathbf{x}_k = \mathbf{f}(\mathbf{x}_k, \mathbf{u}_k) + \mathbf{w}_k$$

where \mathbf{f} is the nonlinear function that describes the system dynamics, \mathbf{u}_k is the control input vector, and \mathbf{w}_k is the process noise vector, which is assumed to be Gaussian with mean zero and covariance matrix \mathbf{Q}_k .

At each time step k , the EKF receives a noisy measurement of the state of the system, represented as a vector \mathbf{z}_k . The measurement is modeled as a nonlinear function of the true state plus some Gaussian noise:

$$\mathbf{z}_k = \mathbf{h}(\mathbf{x}_k) + \mathbf{v}_k$$

where \mathbf{h} is the nonlinear function that describes the measurement function and \mathbf{v}_k is the measurement noise vector, which is assumed to be Gaussian with mean zero and covariance matrix \mathbf{R}_k .

To use the EKF to estimate the state of the system, we need to linearize the nonlinear functions around the current state estimate. We can do this by taking the first-order Taylor series expansion of the nonlinear functions:

$$\mathbf{f}(\mathbf{x}_k, \mathbf{u}_k) \approx \mathbf{F}_k \mathbf{x}_{k-1} + \mathbf{G}_k \mathbf{u}_k$$

$$\mathbf{h}(\mathbf{x}_k) \approx \mathbf{H}_k \mathbf{x}_k$$

where \mathbf{F}_k and \mathbf{G}_k are the Jacobians of the nonlinear function \mathbf{f} with respect to the state and control inputs, respectively, and \mathbf{H}_k is the Jacobian of the nonlinear function \mathbf{h} with respect to the state.

Using the linearized functions, we can apply the standard KF equations to estimate the system's state. The EKF updates the prior estimate of the state in the same way as the KF:

$$\hat{\mathbf{x}}_{k|k-1} = \mathbf{f}(\hat{\mathbf{x}}_{k-1|k-1}, \mathbf{u}_k)$$

$$\mathbf{P}_{k|k-1} = \mathbf{F}_k \mathbf{P}_{k-1|k-1} \mathbf{F}_k^T + \mathbf{G}_k \mathbf{Q}_k \mathbf{G}_k^T$$

where $\hat{\mathbf{x}}_{k-1|k-1}$ and $\mathbf{P}_{k-1|k-1}$ are the estimated state and covariance matrix at the previous time step, respectively.

2.3.3 Particle Filter

The PF is a probabilistic filtering algorithm that can handle nonlinear and non-Gaussian systems. This filter represents the belief about the system's state as a set of particles, each representing a possible state of the system. The particles are sampled from the prior distribution, which is the distribution of the state of the system at the previous time step. Each particle is assigned a weight that reflects how well it explains the measurements.

At each time step, the PF applies a two-step process to update the set of particles. The first step is the prediction step, which updates the particles based on the system dynamics:

$$\mathbf{x}_k^{[i]} = \mathbf{f}(\mathbf{x}_{k-1}^{[i]}, \mathbf{u}_k) + \mathbf{w}_k^{[i]}$$

where $\mathbf{x}_k^{[i]}$ is the state of the i -th particle at time k , \mathbf{f} is the system dynamics function, \mathbf{u}_k is the control input at time k , and $\mathbf{w}_k^{[i]}$ is the process noise that affects the i -th particle at time k .

The second step is the measurement update step, which updates the weights of the particles based on how well they explain the measurements:

$$w_k^{[i]} \propto p(\mathbf{z}_k | \mathbf{x}_k^{[i]})$$

where \mathbf{z}_k is the measurement at time k , and $p(\mathbf{z}_k | \mathbf{x}_k^{[i]})$ is the likelihood of the measurement given the i -th particle.

The algorithm resamples the particles according to their weights to avoid particle impoverishment. The resampling process generates a new set of particles with higher weights and discards those with lower weights. The new set of particles represents a better approximation of the true posterior distribution. The PF is a powerful tool for probabilistic filtering in nonlinear and non-Gaussian systems. However, it may suffer from particle degeneracy and poor sampling efficiency in high-dimensional spaces.

2.4 Differential Wheeled Robot

Most of the concepts in this section can be found in (SIEGWART; NOUR-BAKHSH; SCARAMUZZA, 2011; THRUN, 2002). A Differential Wheeled robot is a type of mobile robot that uses two independently driven wheels to move and turn. The name comes from the fact that the wheels on either side of the robot can be driven at different speeds, allowing the robot to turn by varying the speed of each wheel.

The kinematics of a Differential Wheeled robot (as shown in Fig. 2.1) can be described using the following equations:

$$v = \frac{r}{2}(\omega_r + \omega_l)$$

$$\omega = \frac{r}{b}(\omega_r - \omega_l)$$

where v is the linear velocity of the robot, ω is its angular velocity, r is the radius of the wheels, b is the distance between the wheels, ω_r is the angular velocity of the right wheel, and ω_l is the angular velocity of the left wheel. These equations show that the robot will move forward in a straight line if both wheels are driven at the same speed. If the speeds of the two wheels are different, the robot will turn, with the direction and rate of turning determined by the difference in speeds.

Differential Wheeled robots are commonly used in robotics research and applications, as they are relatively simple and easily controlled. However, they have some limitations, such as difficulty accurately measuring the robot's position and orientation, especially on uneven or slippery terrain.

2.4.1 Dead-Reckoning

Dead-reckoning is a method that autonomous mobile robots use to estimate their pose (position and orientation) by keeping track of their movements over time. This method relies on measuring the robot's speed and direction of movement and integrating these measurements to calculate the robot's pose. Let Δt be the time interval between two successive measurements of the robot's speed and direction, v be the robot's linear speed, and ω be the robot's angular speed.

Then, the robot's position and orientation can be estimated using the following equations:

$$\Delta x = \Delta t v \cos(\theta)$$

$$\Delta y = \Delta t v \sin(\theta)$$

$$\Delta\theta = \Delta t \omega$$

where θ is the robot's orientation relative to some reference frame. By integrating these equations over time, the robot's position and orientation can be updated as follows:

$$x_t = x_{t-1} + \Delta x_t$$

$$y_t = y_{t-1} + \Delta y_t$$

$$\theta_t = \theta_{t-1} + \Delta \theta_t$$

where (x_t, y_t) is the robot's position at time t and θ_t is the robot's orientation at time t . However, dead-reckoning has some inherent errors that accumulate over time due to inaccuracies in the robot's speed and direction measurements and external factors such as wheel slippage and terrain irregularities. These errors may lead to significant deviations from the robot's true position and orientation, especially over long distances. Finally, this method is often combined with other localization methods, such as landmark-based localization or odometry correction, to mitigate these errors. These methods use external reference points, such as visual landmarks or beacons, to correct the robot's estimated position and orientation and improve its overall accuracy.

2.4.2 Markov Localization

Markov Localization is a technique for estimating the robot's state in an environment given its sensor measurements and actions. In this approach, the robot's state is modeled as a probability distribution over a discrete set of possible locations or poses. The belief of the robot's state is updated recursively based on its sensor readings



Figure 2.1 – Pioneer P3DX differential wheeled robot from Adept Robots into an indoor environment.

and actions. Let \mathbf{x}_t be the true state of the robot at time t , and let $\mathbf{z}_{1:t}$ and $\mathbf{u}_{1:t}$ be the sequences of all sensor measurements and actions up to time t , respectively. The goal of this localization algorithm is to estimate the belief $bel(\mathbf{x}_t)$, the probability distribution of the robot's state at time t given all the available sensor measurements and actions:

$$bel(\mathbf{x}_t) = p(\mathbf{x}_t | \mathbf{z}_{1:t}, \mathbf{u}_{1:t})$$

This distribution is updated recursively using Bayes' rule:

$$bel(\mathbf{x}_t) = \eta p(\mathbf{z}_t | \mathbf{x}_t) \sum_{\mathbf{x}_{t-1}} p(\mathbf{x}_t | \mathbf{x}_{t-1}, \mathbf{u}_t) bel(\mathbf{x}_{t-1})$$

where η is a normalization constant to ensure that $bel(\mathbf{x}_t)$ is a valid probability distribution, $p(\mathbf{z}_t | \mathbf{x}_t)$ is the likelihood of the sensor measurement \mathbf{z}_t given the robot's state \mathbf{x}_t , and $p(\mathbf{x}_t | \mathbf{x}_{t-1}, \mathbf{u}_t)$ is the transition probability of moving from state \mathbf{x}_{t-1} to state \mathbf{x}_t given the action \mathbf{u}_t . The summation is over all possible states \mathbf{x}_{t-1} that could have led to the current state \mathbf{x}_t .

This localization algorithm initializes the belief $bel(\mathbf{x}_0)$ as a uniform distribution over all possible states. Then, at each time step t , it updates the belief using the above recursive formula, based on the current sensor measurement \mathbf{z}_t and action \mathbf{u}_t . The resulting belief $bel(\mathbf{x}_t)$ represents the robot's estimate of its state at time t and can be used for planning and control purposes. Markov Localization is a powerful technique for robot localization in uncertain environments and has been widely used in many robotics applications. However, it can be computationally expensive, especially in large environments or high-dimensional state spaces. Various approximations and optimizations, such as particle filters and grid-based methods, have been developed to address these issues.

2.4.3 Kalman Filter Localization

The KF Localization algorithm is a technique for estimating the robot's state in an environment, given its sensor measurements and actions. In this approach, the robot's state is modeled as a continuous vector, and the belief of the robot's state is represented as a Gaussian distribution over this vector. Let \mathbf{x}_t be the actual state of the robot at time t , and let $\mathbf{z}_{1:t}$ and $\mathbf{u}_{1:t}$ be the sequences of all sensor measurements and actions up to time t , respectively. The goal of Kalman Filter Localization is to estimate the belief $bel(\mathbf{x}_t)$, the Gaussian distribution of the robot's state at time t given all the available sensor measurements and actions:

$$bel(\mathbf{x}_t) = \mathcal{N}(\mathbf{x}_t | \mu_t, \Sigma_t)$$

where μ_t is the mean of the Gaussian distribution, and Σ_t is its covariance matrix.

The Kalman Filter Localization algorithm updates the belief recursively based on the sensor measurements and actions using the following steps:

1. Prediction: the algorithm predicts the robot's state after executing the current action \mathbf{u}_t , based on the previous belief $bel(\mathbf{x}_{t-1})$ and the motion model $p(\mathbf{x}_t | \mathbf{x}_{t-1}, \mathbf{u}_t)$:

2. Correction: the algorithm corrects the predicted belief based on the sensor measurement \mathbf{z}_t , using the observation model $p(\mathbf{z}_t|\mathbf{x}_t)$:

This localization algorithm initializes the belief $bel(\mathbf{x}_0)$ as a Gaussian distribution with a known mean and covariance. Then, at each time step t , it updates the belief using the above recursive formula, based on the current sensor measurement \mathbf{z}_t and action \mathbf{u}_t . The resulting belief $bel(\mathbf{x}_t)$ represents the robot's estimate of its state at time t and can be used for planning and control purposes. Finally, its main drawback is that systems must be linear, and the robot's state needs to be Gaussian.

2.4.4 Extended Kalman Filter Localization

The EKF is a widely used technique for state estimation and localization in robotics. It is an extension of the KF capable of handling non-linear systems by linearizing the system dynamics and measurement models around the current estimate. In robot localization, the EKF estimates the robot's pose in a known environment, given noisy sensor measurements. The EKF maintains a probability distribution over the robot's pose, which is updated based on the robot's motion and sensor measurements.

The EKF localization algorithm also consists of two main steps: the prediction step and the update step. In the prediction step, the EKF uses the motion model to predict the robot's pose at the current time step based on its previous pose and control inputs. The motion model is typically non-linear and includes uncertainties due to control noise and model inaccuracies. In the update step, the EKF uses the sensor measurements to correct the predicted pose. The sensor measurements are typically noisy and nonlinear and, therefore, cannot be directly incorporated into the prediction step. Instead, the EKF linearizes the measurement model around the predicted pose to obtain a linear approximation of the measurement model. This localization algorithm is an iterative process that alternates between the prediction and update steps, using the updated probability distribution from the previous time step as the prior for the current prediction step. This algorithm is computationally efficient and can handle nonlinear motion and measurement models, making it a popular choice for localization in robotics. However, there are several issues with using an EKF to model a Gaussian process.

Firstly, the EKF relies on linearizing the system dynamics, which may result in inaccurate predictions when dealing with highly nonlinear systems. This may lead to poor performance, especially in cases where the system dynamics are changing rapidly. Secondly, the EKF assumes that the process and measurement noise are Gaussian and independent. In practice, this assumption may not hold, especially when dealing with real-world data that is subject to various types of noise and uncertainty. This may result in biased estimates and suboptimal performance. Thirdly, the EKF requires an explicit

definition of the process and measurement models, which may not always be possible or accurate. This may be especially problematic when dealing with complex non-linear systems, where it may be difficult to accurately model the dynamics. Finally, the EKF requires the estimation of many parameters, such as the mean and covariance of the Gaussian process and the noise parameters. Estimating these parameters accurately can be challenging, especially when dealing with high-dimensional or noisy data.

2.4.5 Monte Carlo Localization

The Monte Carlo Localization (MCL) algorithm, also known as PF Localization, is a technique for estimating the state of a robot in an environment given its sensor measurements and actions. Unlike KF Localization algorithm, MCL does not assume a Gaussian distribution for the robot's state but represents the belief as a set of weighted particles, each representing a possible hypothesis of the robot's state. This algorithm is a powerful technique for robot localization in uncertain and nonlinear environments and has been widely used in many robotics applications. However, it suffers from the particle degeneracy problem, where the weights of most particles become very small over time, leading to poor sampling efficiency and loss of representativeness.

2.5 Galileo Hand

The Galileo Hand (illustrated in Fig. 2.2) is an affordable, open-source and UTD myoelectric upper-limb prosthesis designed for unilateral transradial amputees (FAJARDO *et al.*, 2017; FAJARDO *et al.*, 2020). The distal, proximal, and middle phalanges conform each digit, with the following three: distal and proximal interphalangeal (DIP and PIP) and the metacarpophalangeal (MCP) one, as illustrated in Fig. 2.5). In addition, every finger has 3 degrees of freedom (DOF). Each finger has attached a geared brushed DC motor with an output torque of around 0.42 Nm that drives every limb with a gear ratio of 250:1, which results in one degree of actuation (DOA) for each digit. In addition, the thumb mechanism functions differently, as it possesses only two DOA: one for the flexion and extension processes and another for the abduction and adduction movements (FAJARDO *et al.*, 2020).

The Galileo Hand's design is underactuated with the aim to simplify the manufacturing and assembling processes, as well as to assimilate the human hand's movements and reduce costs. In addition, adaptive grasping can be achieved with such an actuation system, as explained in (TAKAKI; OMATA, 2011; DARIO *et al.*, 2000), which consists of interacting with objects during ADLs. The main modules in the prosthesis are the palm, the thumb rotation mechanism, and the fingers, which vary only in the length of each phalanx.

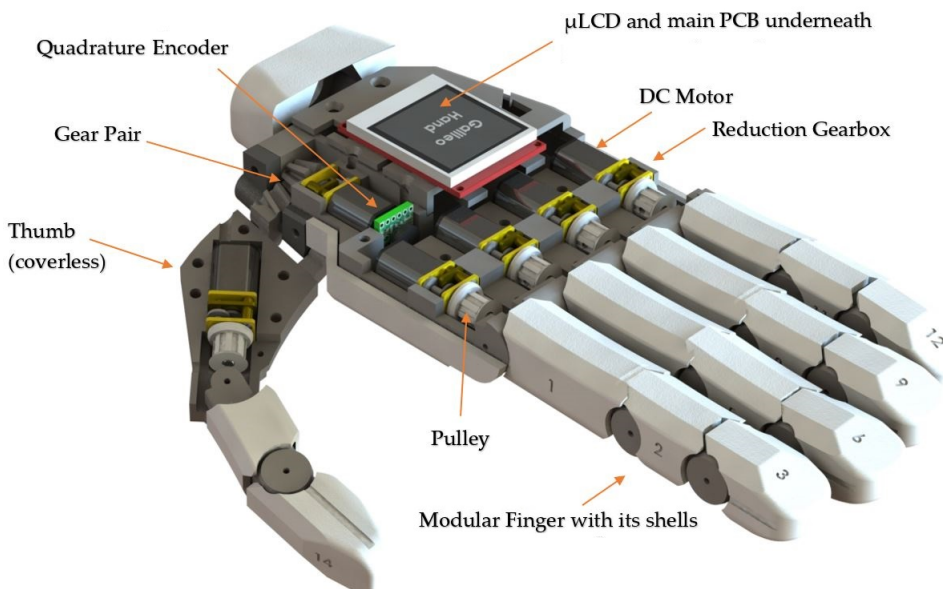


Figure 2.2 – Mechanical design of the Galileo Hand.

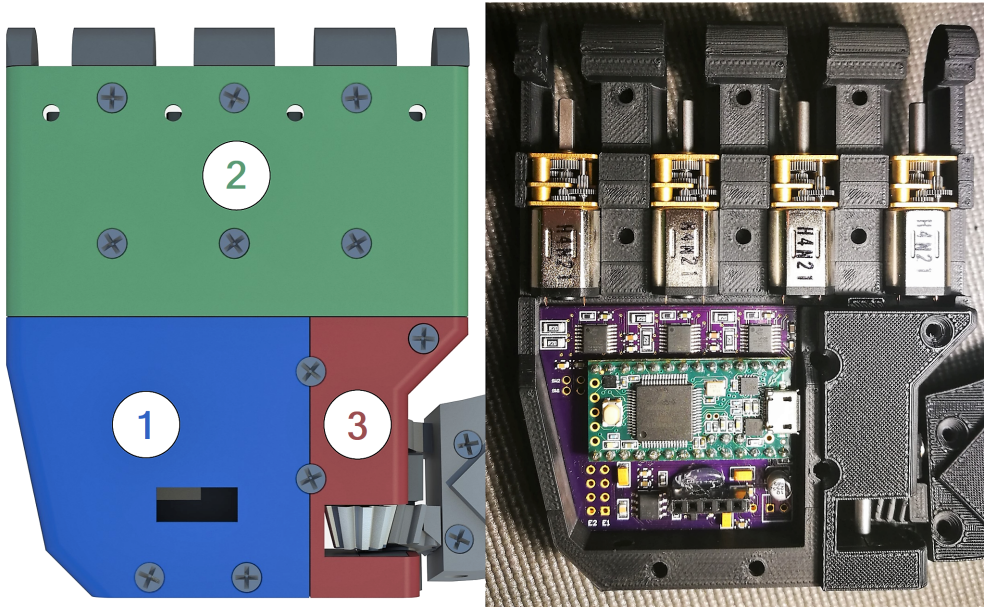


Figure 2.3 – Top view of the modular palm sections. (1) The main PCB board controller. (2) Motors driving the index, middle, ring and little fingers. (3) Actuator in charge of the rotation of the thumb.

2.5.1 Palm Design and Mechanisms

The design requirements were set up with the help of two male volunteers suffering from unilateral, transradial amputation and considering the results from the reported users' needs in (CORDELLA *et al.*, 2016). The mechanism consists of Micro-metal brushed DC gear motors (250:1) with an output torque of around 0.42 Nm , which perform the flexion/extension movements of the five fingers through an under-tendon-actuated system.

The palm has three different sections with individual covers, one for the six motors that drive each digit but the thumb, another for the actuator that enables the thumb rotation, and the last one for the rest of the components, as it is shown in Fig. 2.3. Such a design allows for easy maintenance without disassembling the whole prosthetic hand.

2.5.2 Thumb Movement Characteristics

The thumb has been designed with two DOAs to recreate the six movements that humans can perform, as described in (KAPANDJI, 1971). One actuator is located inside the thumb metacarpal phalanx, responsible for the flexion and extension of the proximal and distal phalanges. The second one, located in the metacarpophalangeal joint of the thumb, is responsible for its abduction and adduction, which is monitored by the reading of a quadrature encoder. This joint is built by a bevel and a helical gear working together to transmit the torque from the actuator with a ratio of 8:11, creating a beveloid

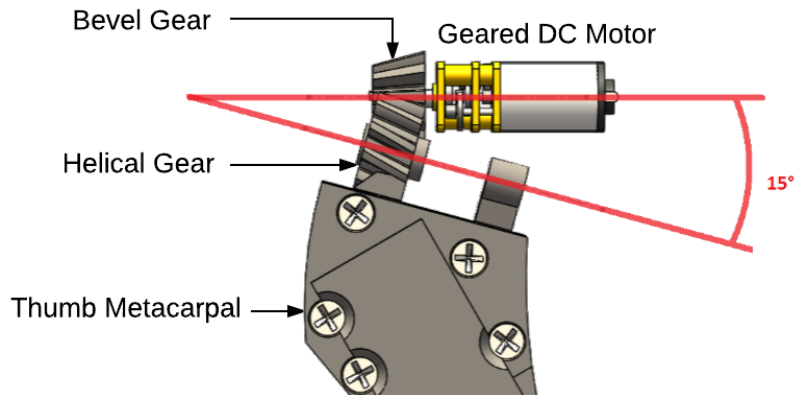


Figure 2.4 – Thumb mechanism side view, beveloid gear pair.

gear pair (ZHU *et al.*, 2012), as shown in Fig. 2.4. Rotating the thumb around an axis shifted 15° from the palm plane increases the abducted position of the thumb. This way, the rotation axis is shifted without inclining the motor, allowing it to perform a larger prismatic grasp (CUTKOSKY, 1989) while simultaneously saving space inside the palm and making it easier to manufacture using 3D printing technology.

2.6 The Under-tendon-driven Machine

The finger's flexion and extension process is achieved using active and passive tendons (illustrated in Fig. 2.5). The active one is a waxed nylon cord actuated by its corresponding motor, closing the digit. The passive one is a round, surgical-grade elastic that springs the finger back open.

This results in a positive tensile force, f_{ta} , when the motor coils the string; and a passive one, f_{te} , which is uniquely dependant on the deflection of the joints, opposing itself to its active counterpart (OZAWA; HASHIRII; KOBAYASHI, 2009; FAJARDO *et al.*, 2020). Thus, the relationship for the generalized coordinates, $\mathbf{q} = [q_1 \ q_2 \ q_3]^T$, of a finger and the motor angle vector, $\boldsymbol{\theta} = [\theta \ 0]^T$, with, θ , as the gearhead's angular position, is given by the following expression

$$\mathbf{q} = \mathbf{J}_j^+ [\mathbf{l} - \mathbf{l}_0 - \mathbf{J}_a \boldsymbol{\theta}] + \mathbf{q}_0 \quad (2.24)$$

where, $\mathbf{l} = [l_a \ l_e]^T$, is the deflection of the active and passive tendons (l_a and l_e , correspondingly); \mathbf{q}_0 are the initial angular displacement of the joints, $\mathbf{l}_0 = [0 \ l_{e0}]^T$ the initial expansion of the tendons; and

$$\mathbf{J}_a = \begin{bmatrix} r_a & 0 \\ 0 & 0 \end{bmatrix}$$

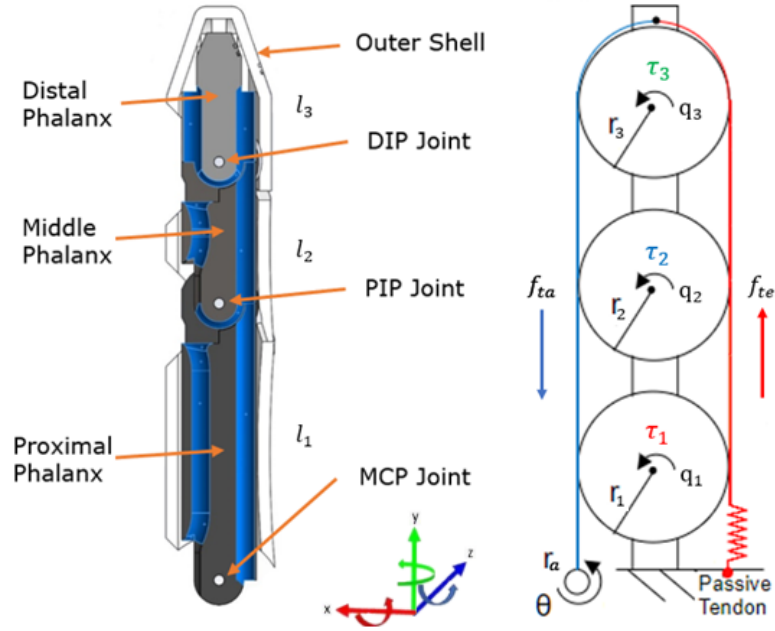


Figure 2.5 – UTD system, where r_1, r_2, r_3 and r_a , are the pulleys' radix; θ , the gearhead shaft's angular position; l_1, l_2 and l_3 the length of each phalanx and τ_1, τ_2 and τ_3 the joint's torque.

the Jacobian matrix related to the actuator, such that r_a is the motor's gearhead shaft pulley radius.

Besides, $(\mathbf{J}_j^T)^+$ is the Moore-Penrose pseudoinverse of the transposed Jacobian matrix J_j composed by the active and passive tendons as $\mathbf{J}_j = [\mathbf{J}_{ja} \quad \mathbf{J}_{je}]^T$, which results in the following expression (for a two-tendon, $L = 2$, and three-jointed, $N = 3$, model)

$$\mathbf{J}_j = \begin{bmatrix} r_1 & r_2 & r_3 \\ -r_1 & -r_2 & -r_3 \end{bmatrix} \quad (2.25)$$

considering that r_1, r_2 and r_3 are the radius of the MCP, PIP and DIP joints, respectively.

Hence, the torque exerted by each joint, $\boldsymbol{\tau} \in \mathbb{R}^N$, and the tensile force, $\mathbf{f}_t \in \mathbb{R}^L$ such that $\mathbf{f}_t = [f_{ta} \quad f_{te}]^T$ can be determined as follows

$$\boldsymbol{\tau} = -\mathbf{J}_j^T \mathbf{f}_t \quad (2.26)$$

$$\mathbf{f}_t = \mathbf{f}_b - (\mathbf{J}_j^T)^+ \boldsymbol{\tau} \quad (2.27)$$

with $\mathbf{f}_b \in \mathbb{R}^L$ being a bias force vector that prevents the tendons from loosening and defined as follows

$$\mathbf{f}_b = \mathbf{A}\boldsymbol{\xi}, \quad \mathbf{A} = [\mathbf{I}_L - (\mathbf{J}_j^T)^+ \mathbf{J}_j^T] \quad (2.28)$$

such that ξ is a compatible dimensional vector with \mathbf{A} and \mathbf{I}_L is the identity matrix of size L .

Since a positive initial expansion of the passive tendon, l_{e0} , is considered for each finger, $f_b > 0$, and $\text{rank}(\mathbf{J}_j) = 1 < \mathbf{N}$, resulting in a UTD mechanism described by the following dynamic system.

$$\mathbf{M}(\mathbf{q})\ddot{\mathbf{q}} + \mathbf{C}(\mathbf{q}, \dot{\mathbf{q}})\dot{\mathbf{q}} + \mathbf{G}_g(\mathbf{q}) + \mathbf{J}_j^T \mathbf{f}_t = 0 \quad (2.29)$$

$$J_m \ddot{\theta} + b\dot{\theta} + r_p f_{ta} = \tau_m \quad (2.30)$$

where $\mathbf{M}(\mathbf{q})$ is the inertia matrix of the finger, $\mathbf{C}(\mathbf{q}, \dot{\mathbf{q}})$ is the Coriolis matrix and $\mathbf{G}_g(\mathbf{q})$ is the gravity load matrix. Furthermore, J_m , are the gearhead's moment of inertia, b , is the damping coefficient, τ_m , the torque exerted by the motor gearhead's shaft, and r_p , the radius of the pulley (OZAWA; HASHIRII; KOBAYASHI, 2009).

2.7 User-prosthesis Interface

Several works in the literature present substantial progress in advanced bionic prosthetic devices in recent years, offering people with disabilities many different alternatives and characteristics to improve their condition. This progress includes promisingly works in haptics (CHORTOS; LIU; BAO, 2016; JIMENEZ; FISHEL, 2014) and diverse methods to recover and interpret the user intent (MOUTOPOULOU *et al.*, 2015; HOTSON *et al.*, 2016; NAVARAJ *et al.*, 2015; JOHANSEN *et al.*, 2016). Some methods to operate upper-limb prostheses control the prosthetic device using user-prosthesis interfaces (UPIs) that exclusively analyze a specific activation profile based on processing electromyography (EMG) signals. Some of such iterations substitute the visual stimuli by utilizing other types of feedback, like vibrotactile ones (CIPRIANI *et al.*, 2008). Moreover, others include implants that utilize Bluetooth or radio channel waves to communicate with them (MOUTOPOULOU *et al.*, 2015; MIOZZI *et al.*, 2018; STANGO; YAZDANDOOST; FARINA, 2015). These versions use wireless charging to function and regulate the power dissipation inside a safe range to avoid damage to the user's skin tissue.

Some approaches use brain-machine interfaces (BMI) to control these devices, eliminating any visual stimulus to interact with the artificial limb and resembling how limbs are usually operated. Newer methodologies are based on high-density electrocorticography (ECoG), which allows the patient to control each finger individually through an adequate reinnervation process (HOTSON *et al.*, 2016). However, these interfaces require very intrusive and expensive procedures. Other projects utilize interaction processes that do not seem intuitive to the users, employing more creative approaches to analyzing the EMG

signals by using other members to drive the movements of the prosthetic limb, as shown on (NAVARAJ *et al.*, 2015) and (JOHANSEN *et al.*, 2016), which use the toes and the tongue, respectively. Such techniques result in viable alternatives, especially for bilateral amputees. However, there may be better options than such methodologies for unilateral transradial amputees since they affect how some typical activities of daily living (ADLs) must be carried out.

Alternatively, most sophisticated research assistive devices are based on multimodal approaches. These methodologies usually consist of taking a set of predefined and well-known EMG features and complementing them with information from other kinds of sensors like inertial measurement units (IMUs), micro-electromechanical systems (MEMS) microphones, mechanomyography (MMG), or force myography (FMG) showing a substantial improvement in classification rates and bimanual performance (GUO *et al.*, 2017; VOLKMAR *et al.*, 2019; FUJIWARA; SUZUKI, 2018; JIANG *et al.*, 2017). This approach has been used successfully to improve the user control of prosthetic devices in different manners, such as using a multimodal system with Radio Frequency Identification (RFID) tags on specific objects. In this stance, the cognitive effort is reduced to operate an upper-limb prosthetic device and address some of the well-known issues of EMG techniques, such as the limb position effect (TRACHTENBERG *et al.*, 2011; FOUGNER *et al.*, 2012; FOUGNER *et al.*, 2011). Other stances have been considered using the multimodal approach, such as utilizing voice control in tandem with visual feedback through a small embedded touchscreen LCD, providing the users with other alternatives to control their prosthetic device in different manners (FAJARDO; LEMUS; ROHMER, 2015; FAJARDO *et al.*, 2017). Other studies have been conducted to increase upper-limb prostheses' functionality, combining surface EMG (sEMG) and deep-learning-based artificial vision systems. This approach works by associating a subset of predefined objects to a list of specific grasp based on the target's geometric properties, which are gathered by different types of cameras. Such classification processes are fulfilled via convolutional neural networks (CNN) employing customized image object classifiers.

2.7.1 High Level Controller

The Galileo Hand incorporates a Myo armband to gather and interpret eight channels of sEMG with an HM-10 Bluetooth Low Energy (BLE) module to transmit interpreted poses to the main MCU of the prosthetic device, as well as an intelligent μ LCD (4D-Systems' 1.44" μ LCD-144-G2) for visual feedback. This way, utilizing the MyoBridge library and adapting the hardware according to the architecture proposed in (RYSER *et al.*, 2017) allows a successful exchange of information between the components. The gathered information is later transferred to an ATmega328P (secondary microcontroller unit) and posteriorly to the main MCU to drive each DC motor, illustrated in Fig. 2.6. This

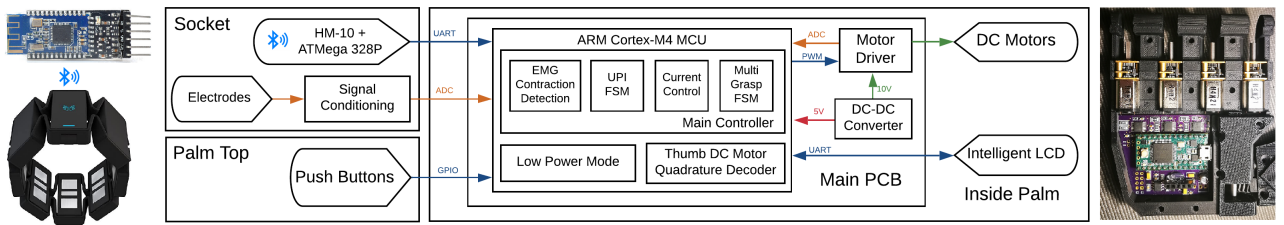


Figure 2.6 – System block diagram showing the embedded controller architecture and the integration with external modules.

complementary MCU is responsible for acquiring the user intent as raw EMG signals or Myo-specific poses. Consequently, it converts them into packages transmitted via Universal Asynchronous Receiver/Transmitter (UART) to the Galileo Hand's main MCU. The HM-10's firmware was flashed with the MyoBridge program, using RedBearLab's CCLoader as an aide for this procedure to function aptly. This way, the armband may connect with the BLE module to transmit raw EMG signals or interpreted poses correctly.

Packet reception is handled using UART interruptions. Once the package is received, it is evaluated, and action is taken based on the transmission content. If the message contains a Myo-specific pose, it triggers transitions between Finite State Machines (FSM) states used to implement the UPI that controls the prosthetic device and alters the information presented on the screen. In that case, a notification via another UART port is sent to the independent μ LCD's microcontroller to present visual feedback to the user. On the other hand, if the message contains raw EMG signals, the device fills up two circular buffers of signals collected by the electrodes placed near the palmaris longus and the extensor digitorum muscles (for unilateral below-elbow disarticulations). This way, customized methods to interpret the user intention can be used to adapt the bracelet to the prosthesis, such as works presented in ([ATASOY et al., 2016](#); [VISCONTI et al., 2018](#)). Then, once the user's intent has been received, a high-level controller (HLC) uses this information to perform the necessary action that each finger must take to achieve predefined gestures and grips available to the user.

2.7.1.1 Gestures adapted to the prosthesis

Below is a clear and detailed explanation of the various gestures and grips that users can perform through the UPI of the prosthesis. Some of them are illustrated in Fig. 2.7.

1. "Close": This grasp involves flexion of all the fingers and rotation of the thumb.
2. "Hook": In this grasp, the thumb is the only finger extended and adducted.
3. "Lateral": Coiling of the strings of all fingers occurs, with the thumb abducted.

4. "Pinch": This grasp involves flexion of the index and thumb, along with abduction of the thumb, enabling a precision grasp.
5. "Point": All motors are actuated except for the index finger.
6. "Peace": All fingers are closed except for the index and middle finger.
7. "Rock": Flexion of all fingers except the index and little finger, with the thumb adducted.
8. "Aloha": The index, middle, and annular fingers are flexed.
9. "Three": All motors are actuated except for the index, middle, and annular fingers.
10. "Four": Similar to the previous gesture, but with the little finger extended.
11. "Fancy": The only extended finger is the little finger, with an adducted thumb.
12. "Index": In this grasp, the only flexed finger is the one giving the name to the action.

2.7.1.2 Multimodal approach using buttons and Myo interface

The interface selected to operate the prosthesis was selected based on the results obtained in ([FAJARDO et al., 2021](#)). This interface operates either by receiving gestures from the Myo armband or push buttons installed on the hand's dorsal side to select a grip from the graphical menu or to perform an action ([FAJARDO et al., 2017](#)). The functionality of this UPI is shown in the FSM in Fig. 2.8. Both the buttons, $B = \{b_0, b_1\}$, and a reduced muscle contractions subset, $Q = \{q_0, q_1\}$, corresponding to Thalmic Labs' "Myo poses", are used to operate the prosthesis. Performing "wave out", q_0 , and "wave in", q_1 , hand extension and flexion, respectively, as well as b_0 and b_1 , causes a forward or backward switch of the selected element in the menu displayed on the screen (shown in Fig. 2.9); this process is represented by the state S_1 .

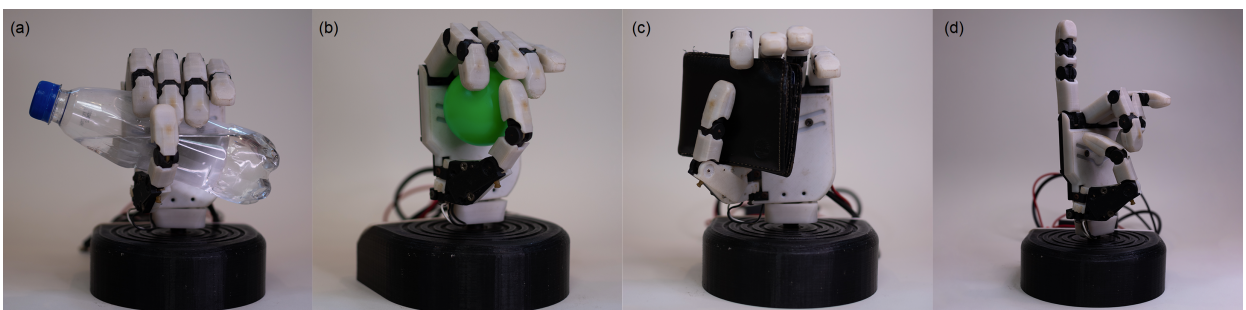


Figure 2.7 – The image shows the Galileo Hand grabbing the objects used in the trials.
 (a) Holding a "water bottle"; (b), holding a small plastic "ball"; (c), holding a "wallet" and (d), "pointing".

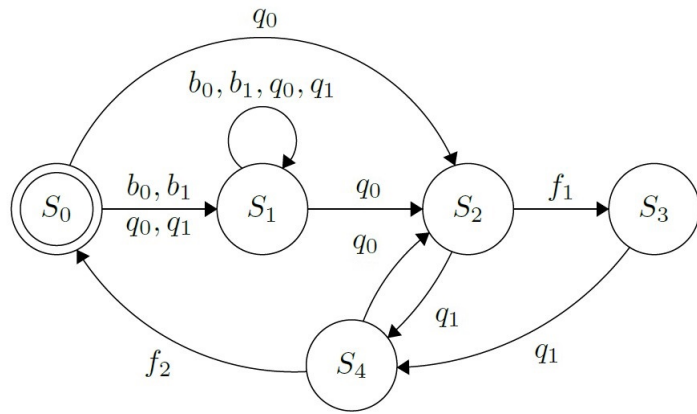


Figure 2.8 – Finite State Machine showing the behavior of the interface using buttons and the Myo to operate. S_0 indicates that the hand is completely open; S_1 , that there was a change in the selected grip; S_2 , that the selected grip is being performed (when it is completed, the flag f_1 is lifted). Also, S_3 represents that the hand is currently enacting the chosen gesture; while, S_4 , that the fingers are opening (process that informs it is finished by lifting the flag f_2).

The state S_0 indicates that the fingers on the prosthesis are fully extended, in their default initial state, while in S_3 , the hand is currently performing the chosen grip. An important aspect to note is that, while in this state, changing the menu's selection is presented to the user, as the motor activation processes' timing differs between actions and could lead to wrong finger positioning if the case arose. The states S_2 and S_4 indicate that the prosthetic device is currently closing or opening its fingers, respectively. These procedures can be interrupted by each other if a correct command is received. In addition to that, to execute an action q_0 needs to be performed by the user. At the same time, q_1 also deactivates performed actions. This simplified subset provides a viable alternative if some of the Myo poses are unperformable by the patient.

Finally, the last elements in the FSM representing the interface's behavior are the flags f_1 and f_2 . The first one is triggered when all the fingers have reached their desired position when performing an action, while the second triggers when all the fingers returned to their initial position, θ_0 .



Figure 2.9 – Galileo Hand’s graphical menu (left) and the prosthesis performing the action “Close” (right).

3 Problem Statement

This chapter delves into the application of robust filtering to assistive robotics. The first approach proposes advanced robust estimation techniques and output-feedback control strategies based on LMIs applied to sensorless transradial upper-limb prostheses. In contrast, the second approach delves into two alternatives to the probabilistic method for landmark-based mobile robot localization, also based on LMIs.

In a sensorless system such as the Galileo Hand, measuring all the system's states is often difficult or impractical, negatively impacting the performance of the prosthetic device. \mathcal{H}_∞ filter estimators provide a solution to this problem by using a mathematical model of the system to estimate its states based on available sensor measurements.

The main advantage of \mathcal{H}_∞ filter estimators is their robustness to disturbances and uncertainties. This advantage is relevant due to the significant input signal variations related to environmental changes, system degradation, or due to the user's movements. These filter estimators are designed to minimize the impact of these disturbances and uncertainties, resulting in more accurate state estimates. In addition to their robustness, \mathcal{H}_∞ filter estimators also offer excellent performance in terms of convergence and tracking. This feature means that these estimators can quickly and accurately estimate the system's state and adjust to changes in the input signals in real-time applications.

On the other hand, \mathcal{H}_∞ filter estimators also have proven to be a powerful tool for landmark-based mobile robot localization. Mobile robots operating in real-world environments are also subject to various sources of uncertainty, including sensor noise, environmental variability, and odometry errors. Therefore, in addition to the advantages mentioned above, \mathcal{H}_∞ filter estimators offer a flexible and modular approach to the mobile robot localization problem. They can be easily combined with other state estimation and control techniques to create a complete localization and control system for the robot. This flexibility allows the robot to adapt to different environments and tasks and may lead to improved overall performance.

Therefore, the methods proposed throughout this work take advantage of LMI-based \mathcal{H}_∞ filter estimation methods, which have several advantages over stochastic approaches. In addition to presenting robustness against uncertainties, they can handle nonlinearity and time-varying systems through linear parameter-varying (LPV) systems, guaranteeing the stability and performance.

3.1 Robust Control Strategy for Sensorless UTD Prosthetic Hands

To control the fingertip force exerted by the fingers and the angular position of the gear shaft that drives the fingers of the prosthetic device, it is necessary to determine both parameters at each moment. This way, a control system can regulate them to the desired value and operate the actuators on the prosthesis accordingly. However, from Eqs. (2.29)-(2.30), it is evident that the finger's dynamic behavior of the coupled system is not described by a Linear Time-invariant (LTI) system, mainly due to the nature of its terms. Thus, it is difficult to estimate in real-time the full state of the coupled system of differential equations using an embedded system based on an ARM Cortex-M4 microcontroller unit (MCU), as shown in Fig. 2.3.

In this manner, the system's behavior was approximated by a linear model, which considers the dynamic equations of motion of the finger as a mass-spring system. This approximation was employed since it presents a mechanical behavior similar to that of a UTD machine, where the passive tendon opposes the flexion movement but favors the extension one. Therefore, it simplifies the computational load since it is unnecessary to linearize the model, allowing the implementation of this control strategy on the MCU used on the prosthetic device. This mechanism does not have a mechanical limit to stop the extension movement, unlike the flexion movement, which is limited when the finger comes into contact with an object or when it is completely closed. This causes the motor to rotate and flex the digit again (as the pulley uncoils completely and then coils the string in the opposite direction), making it difficult to control the extension movement without using a position sensor on the motor shaft. This issue could not be solved simply by measuring the time the finger requires to close and then calculating the extension time. These amounts of time are not equal, as the passive tendon opposes itself to the coiling mechanism but favors its counterpart, even worst when possible disturbance while actuating may provide an offset in that angular position.

On the other hand, if the fingertip position is known and related to the gearhead's angular position, θ , one can close the fingers without any of the problems mentioned previously. Hence, the purpose of implementing a robust observer is to determine the angular displacement and velocity of the gearhead's shaft only, leading to not requiring an exact result for the generalized coordinates \mathbf{q} . However, the estimated state is useful to get an approximation of this parameter as well as the joints' torque, τ by employing Eqs. (2.24) and (2.29).

In addition, by considering i_a as the armature current demanded by the DC motor, G_r as the gear ratio, k_t as the motor's torque constant, and η as the gearhead's efficiency, τ_m can be obtained with the following expression:

$$\tau_m = \eta G_r k_t i_a \quad (3.1)$$

Thus, the continuous-time state-space model for brushed DC motors results in:

$$\dot{\mathbf{x}} = \begin{bmatrix} 0 & 1 & 0 \\ \frac{k_s r_p^2}{J_m} & -\frac{b}{J_m} & \frac{k_t}{J_m} \\ 0 & -\frac{k_e}{L_a} & -\frac{R_a}{L_a} \end{bmatrix} \mathbf{x} + \begin{bmatrix} 0 \\ 0 \\ \frac{1}{L_a} \end{bmatrix} u \quad (3.2)$$

$$\mathbf{y} = [0 \ 0 \ 1] \mathbf{x} \quad (3.3)$$

where $\mathbf{x} = [\theta \ \dot{\theta} \ i_a]^T$, with θ and $\dot{\theta}$ being the gearhead's angular position and velocity, respectively; R_a is the armature's resistance, L_a is the motor's inductance, k_e is the electromotive force constant, k_s is the elastic constant of the passive tendon, u is the applied voltage, and \mathbf{y} is the measured output. This way, the purpose of this simplified model is to develop an \mathcal{H}_∞ observer-based filter in tandem with a full-order filter \mathcal{H}_∞ to estimate the states of the motor of the UTD system that drives the fingers of the Galileo Hand ([FAJARDO et al., 2017](#); [FAJARDO et al., 2020](#)). Thus, several methods are proposed in the following chapter.

3.2 \mathcal{H}_∞ Estimation for Landmark-based Mobile Robot Localization

Localization of mobile robots in a two-dimensional space requires a mathematical model to describe the robot's position as a rigid body on wheels moving across a horizontal plane. Hence, the discrete kinematic model of the differential drive for mobile robots is considered as follows ([SIEGWART; NOURBAKHSH; SCARAMUZZA, 2011](#)).

$$\mathbf{x}_{k+1} = \begin{bmatrix} x_k + \Delta T v_k \cos(\theta_k + \Delta T \omega_k / 2) \\ y_k + \Delta T v_k \sin(\theta_k + \Delta T \omega_k / 2) \\ \theta_k + \Delta T \omega_k \end{bmatrix} \quad (3.4)$$

where $\mathbf{x}_k \in \mathbb{R}^n$ is the robot state vector at time k . Thus, $\mathbf{x}_k = [x_k, y_k, \theta_k]^T$, where x_k and y_k are the Cartesian coordinates of the main axis midpoint between the two driving wheels and θ_k is the orientation of the robot with respect to the inertial frame, while ΔT is the sampling period of the process. Besides, the input control vector $\mathbf{u}_k \in \mathbb{R}^p$ is defined as $\mathbf{u}_k = [v_k, \omega_k]^T$ where v_k and ω_k are the linear and angular velocities of the robot, respectively.

In this way, the kinematic model described in Eq. (3.4) can be rewritten in the following form

$$\mathbf{x}_{k+1} = \begin{bmatrix} 1 & 0 & 0 \\ 0 & 1 & 0 \\ 0 & 0 & 1 \end{bmatrix} \mathbf{x}_k + \begin{bmatrix} \Delta T v_k \cos(\theta_k + \Delta T \omega_k / 2) \\ \Delta T v_k \sin(\theta_k + \Delta T \omega_k / 2) \\ \Delta T \omega_k \end{bmatrix}$$

$$\mathbf{x}_{k+1} = \mathbf{A} \mathbf{x}_k + \tilde{\mathbf{f}}(\mathbf{x}_k, \mathbf{u}_k) \quad (3.5)$$

where $\mathbf{A} \in \mathbb{R}^{n \times n}$ is the process matrix and $\tilde{\mathbf{f}}(\mathbf{x}_k, \mathbf{u}_k)$ represents the nonlinear effect of the control input that also depends on the orientation of the robot θ_k , as is shown in Equation (3.5). So, for the sake of simplicity in the notation, the nonlinear term will be denoted by the matrix $\mathbf{B}_{1,k}$. Also, it is essential to emphasize that this term does not affect the dynamic of the filters proposed in Sections 4.1 and 4.2.

Furthermore, a mathematical model of the sensor that acquires information about the environment is also required. Thus, for this particular case, the 2-D laser-based measurement model was adopted as follows.

$$\mathbf{y}_k = \mathbf{g}(\mathbf{x}_k) = \begin{bmatrix} \sqrt{(x_m - x_k)^2 + (y_m - y_k)^2} \\ \arctan\left(\frac{y_m - y_k}{x_m - x_k}\right) - \theta_k \end{bmatrix} \quad (3.6)$$

where $\mathbf{y}_k \in \mathbb{R}^q$ is the measured output vector, $x_m \in \mathbb{R}$ and $y_m \in \mathbb{R}$ are the Cartesian coordinates of one landmark (for N landmarks, the length of the output vector has to be equal to $2N$). Furthermore, $\mathbf{y}_k = [\rho_k \ \phi_k]^T$, where $\rho_k \in \mathbb{R}$ and $\phi_k \in \mathbb{R}$ are the euclidean distance and the angle from the robot position to a landmark. Besides, well-known methods for feature extraction (corners) and landmark correspondence are assumed (PENG; WANG; CHEN, 2017). However, occupied cells from an occupancy grid map can be considered as individual landmarks, and the correspondence with each laser measurement can be performed using a bi-linear interpolation (KOHLBRECHER *et al.*, 2011).

Since the measurement model $\mathbf{g}(\mathbf{x}_k)$ is nonlinear and time-variant, this expression can be expanded in a Taylor series about the operating point $\hat{\mathbf{x}}_k \in \mathbb{R}^n$ as follows

$$\mathbf{C}_k = \left[\begin{array}{ccc} -\frac{(x_m - x_k)}{\rho_k} & -\frac{(y_m - y_k)}{\rho_k} & 0 \\ \frac{(y_m - y_k)}{\rho_k^2} & -\frac{(x_m - x_k)}{\rho_k^2} & -1 \end{array} \right]_{\mathbf{x}_k=\hat{\mathbf{x}}_k} \quad (3.7)$$

Thus, to solve the localization problem under the LMI-based methods presented in the following chapter, it is necessary to linearize the measurement model $\mathbf{g}(\mathbf{x}_k)$ at each

time step k . This linearization implies solving a convex optimization problem in each algorithm iteration, precisely a semi-definite programming problem via interior point methods ([NEMIROVSKII; GAHINET, 1994](#)).

4 LMI-based \mathcal{H}_∞ Robust Filtering

Linear Matrix Inequality (LMI) based filtering and estimation techniques are state-space methods that utilize matrix inequalities to synthesize optimal filters and estimators for linear systems subject to constraints. These techniques have gained significant attention in the last few decades due to their ability to handle various constraints on the system, such as input/output disturbances, noise, and uncertainties. LMI-based filters and estimators ensure robustness, stability, and performance by minimizing the effect of disturbances while optimizing the system's output. These techniques have numerous applications in areas such as control engineering, signal processing, and robotics.

This chapter delves into two different approaches to addressing guaranteed-cost \mathcal{H}_∞ full-state estimation. The first is based on the well-known two-step prediction-correction approach, while the second presents a full-order robust filter that guarantees better robustness and performance than the two-step method.

4.1 Discrete-time \mathcal{H}_∞ Full-State Estimator

For designing the observer, a discretization of the aforementioned system is required. Considering the noise components and a sampling time k , it results in the following:

$$\mathbf{x}_{k+1} = \mathbf{A}\mathbf{x}_k + \mathbf{B}_1\mathbf{u}_k + \mathbf{B}_2\mathbf{w}_k \quad (4.1)$$

$$\mathbf{y}_k = \mathbf{C}\mathbf{x}_k + \mathbf{D}_1\mathbf{v}_k + \mathbf{D}_2\mathbf{w}_k \quad (4.2)$$

Taking into consideration that for the second case of application, the linearization of the measurement model, $\mathbf{g}(\mathbf{x}_k)$, is needed, the output equation can be described as follows:

$$\mathbf{y}_k = \mathbf{C}_k\mathbf{x}_k + \mathbf{D}_1\mathbf{v}_k + \mathbf{D}_2\mathbf{w}_k \quad (4.3)$$

where $\mathbf{x}_k \in \mathbb{R}^n$, $\mathbf{u}_k \in \mathbb{R}^p$, $\mathbf{y}_k \in \mathbb{R}^q$, $\mathbf{w}_k \in \mathbb{R}^s$ and $\mathbf{v}_k \in \mathbb{R}^t$ are the states, control input, measured output, process, and measurement noise vectors, respectively. Besides, $\mathbf{A} \in \mathbb{R}^{n \times n}$, $\mathbf{B}_1 \in \mathbb{R}^{n \times p}$, $\mathbf{B}_2 \in \mathbb{R}^{n \times s}$, $\mathbf{C} \in \mathbb{R}^{q \times n}$, $\mathbf{D}_1 \in \mathbb{R}^{q \times t}$ and $\mathbf{D}_2 \in \mathbb{R}^{q \times s}$ are the process, input control, and input process noise, measured output, as well as the output process and output sensor noise matrices, correspondingly. For the sake of simplicity, \mathbf{C} and \mathbf{C}_k will

be treated interchangeably. Then, by defining a general noise vector, $\tilde{\mathbf{w}}_k = [\mathbf{w}_k \ \mathbf{v}_k]^T$, an observer-based filter can be described by

$$\hat{\mathbf{x}}_{k+1} = \mathbf{A}\hat{\mathbf{x}}_k + \mathbf{B}_1\mathbf{u}_k - \mathbf{L}(\mathbf{y}_k - \hat{\mathbf{y}}_k) \quad (4.4)$$

where $\hat{\mathbf{x}}_k \in \mathbb{R}^n$ is the estimated state; $\hat{\mathbf{y}}_k \in \mathbb{R}^n$ the estimated output; and \mathbf{L} , the observer gain.

Since the initial conditions of the estimated state, $\hat{\mathbf{x}}_0$, are equal to those of the initial state, $\mathbf{x}_0 = [0 \ 0 \ 0]^T$, one can determine the filtering error dynamic, from the expressions (4.1)-(4.4), with the following augmented system.

$$\mathbf{e}_{k+1} = \mathbf{A}_o\mathbf{e}_k + \mathbf{B}_o\tilde{\mathbf{w}}_k \quad (4.5)$$

$$\tilde{\mathbf{y}}_k = \mathbf{C}_o\mathbf{e}_k + \mathbf{D}_o\tilde{\mathbf{w}}_k \quad (4.6)$$

with

$$\mathbf{A}_o = \mathbf{A} + \mathbf{LC} \quad \mathbf{B}_o = [\mathbf{B}_2 + \mathbf{LD}_2 \quad \mathbf{LD}_1] \quad (4.7)$$

$$\mathbf{C}_o = \mathbf{C} \quad \mathbf{D}_o = [\mathbf{D}_2 \quad \mathbf{D}_1]$$

The main goal is to find an optimal robust observer-based filter for the system composed by (4.1) and (4.2), where the error filtering, \mathbf{e}_k , has to satisfy that $\|\mathbf{e}_k\|_2 \leq \gamma(\|\mathbf{w}_k\|_2 + \|\mathbf{v}_k\|_2)$, with the robustness level $\gamma \in \mathbb{R}$ such that $\gamma > 0$. Therefore, from the bounded-real lemma and given the transfer function $H(z)$ in the complex frequency-domain for the system (4.1-4.3), the norm \mathcal{H}_∞ can be characterized using the quadratic Lyapunov function, $\nu(\mathbf{x}_k) = \mathbf{x}_k^T \mathbf{P} \mathbf{x}_k$, as done in (BOYD *et al.*, 1994), imposing that

$$\|H(z)\|_\infty < \gamma \Leftrightarrow \exists \mathbf{P} \in \mathbb{R}^{n \times n} \ni \mathbf{P} = \mathbf{P}^T > 0 \quad (4.8)$$

where the following expression results by substituting the equations described in (4.7) into Eq. (2.23), defining $\mu = \gamma^2$ and by applying the Schur complement:

$$\begin{bmatrix} \mathbf{P} & \mathbf{A}_o^T \mathbf{P} & \mathbf{0} & \mathbf{C}_o^T \\ * & \mathbf{P} & \mathbf{PB}_o & \mathbf{0} \\ * & * & \mathbf{I}_r & \mathbf{D}_o^T \\ * & * & * & \mu \mathbf{I}_q \end{bmatrix} > 0$$

This way, by substituting again the equations described in (4.7), the following expression is obtained.

$$\begin{bmatrix} \mathbf{P} & \mathbf{A}^T \mathbf{P} + \mathbf{C}^T \mathbf{L}^T \mathbf{P} & \mathbf{0}_{n \times s} & \mathbf{0}_{n \times s} & \mathbf{C}^T \\ * & \mathbf{P} & \mathbf{PB}_2 + \mathbf{PLD}_2 & \mathbf{PLD}_1 & \mathbf{0}_{n \times q} \\ * & * & \mathbf{I}_s & \mathbf{0}_{s \times s} & \mathbf{D}_2^T \\ * & * & * & \mathbf{I}_s & \mathbf{D}_1^T \\ * & * & * & * & \mu \mathbf{I}_q \end{bmatrix} > \mathbf{0}$$

Hence, by changing the variable to substitute the nonlinear term \mathbf{PL} by \mathbf{Z} , an observer meeting the aforementioned requirements may be successfully established if a solution to the following convex optimization problem can be found.

$$\min_{\mathbf{Z}, \mathbf{P}=\mathbf{P}^T > 0} \mu \quad (4.9)$$

which is subject to the following LMI

$$\begin{bmatrix} \mathbf{P} & \mathbf{A}^T \mathbf{P} + \mathbf{C}^T \mathbf{Z}^T & \mathbf{0}_{n \times s} & \mathbf{0}_{n \times s} & \mathbf{C}^T \\ * & \mathbf{P} & \mathbf{PB}_2 + \mathbf{ZD}_2 & \mathbf{ZD}_1 & \mathbf{0}_{n \times q} \\ * & * & \mathbf{I}_s & \mathbf{0}_{s \times s} & \mathbf{D}_2^T \\ * & * & * & \mathbf{I}_s & \mathbf{D}_1^T \\ * & * & * & * & \mu \mathbf{I}_q \end{bmatrix} > \mathbf{0} \quad (4.10)$$

where the matrices $\mathbf{Z} \in \mathbb{R}^{n \times q}$ and \mathbf{P} are the variables of the problem (OLIVEIRA; GEROMEL; BERNUSOU, 2002). In addition to that, $\mathbf{L} \in \mathbb{R}^{n \times q}$ can be recovered using the following expression:

$$\mathbf{L} = \mathbf{P}^{-1} \mathbf{Z} \quad (4.11)$$

On the other hand, to further improve this system's robustness, a slack variable, $\mathbf{G} \in \mathbb{R}^{n \times n}$, can be incorporated so that the optimization problem is given by.

$$\min_{\mathbf{Z}, \mathbf{G}, \mathbf{P}=\mathbf{P}^T > 0} \mu \quad (4.12)$$

subject to the following LMI

$$\begin{bmatrix} \mathbf{P} & \mathbf{A}^T \mathbf{G} + \mathbf{C}^T \mathbf{Z}^T & \mathbf{0}_{n \times s} & \mathbf{0}_{n \times s} & \mathbf{C}^T \\ * & \mathbf{G} + \mathbf{G}^T - \mathbf{P} & \mathbf{G}^T \mathbf{B}_2 + \mathbf{Z} \mathbf{D}_2 & \mathbf{Z} \mathbf{D}_1 & \mathbf{0}_{n \times q} \\ * & * & \mathbf{I}_s & \mathbf{0}_{s \times s} & \mathbf{D}_2^T \\ * & * & * & \mathbf{I}_s & \mathbf{D}_1^T \\ * & * & * & * & \mu \mathbf{I}_q \end{bmatrix} > \mathbf{0} \quad (4.13)$$

Moreover, since $\mathbf{G} + \mathbf{G}^T > \mathbf{P} > 0$, this implies that \mathbf{G} is non-singular ([OLIVEIRA; GEROMEL; BERNUSOU, 2002](#)), resulting in \mathbf{L} that can be recovered by evaluating the equation mentioned underneath:

$$\mathbf{L} = (\mathbf{G}^T)^{-1} \mathbf{Z} \quad (4.14)$$

4.2 Discrete-time \mathcal{H}_∞ Filter

To design a full-order filter (i.e., a $n_f = n$) that guarantees an improved performance level γ , which upper bounds the maximum magnitude of the transfer function from the noise inputs to the estimation error, it was considered an LTI discrete-time system with noise components at sampling time k in the following form

$$\mathbf{x}_{k+1} = \mathbf{A}\mathbf{x}_k + \mathbf{B}_1\mathbf{u}_k + \mathbf{B}_2\mathbf{w}_k \quad (4.15)$$

$$\mathbf{z}_k = \mathbf{C}_1\mathbf{x}_k + \mathbf{D}_{11}\mathbf{w}_k \quad (4.16)$$

$$\mathbf{y}_k = \mathbf{C}_2\mathbf{x}_k + \mathbf{D}_{21}\mathbf{v}_k + \mathbf{D}_{22}\mathbf{w}_k \quad (4.17)$$

Taking into consideration that for the second case of application, the linearization of the process and measurement models is needed, the output equations can be described as follows:

$$\mathbf{x}_{k+1} = \mathbf{A}\mathbf{x}_k + \mathbf{B}_{1,k}\mathbf{u}_k + \mathbf{B}_2\mathbf{w}_k \quad (4.18)$$

$$\mathbf{z}_k = \mathbf{C}_1\mathbf{x}_k + \mathbf{D}_{11}\mathbf{w}_k \quad (4.19)$$

$$\mathbf{y}_k = \mathbf{C}_{2,k}\mathbf{x}_k + \mathbf{D}_{21}\mathbf{v}_k + \mathbf{D}_{22}\mathbf{w}_k \quad (4.20)$$

where $\mathbf{x}_k \in \mathbb{R}^n$, $\mathbf{u}_k \in \mathbb{R}^m$, and $\mathbf{w}_k \in \mathbb{R}^r$, are the state, control input and process noise vectors, whereas $\mathbf{y}_k \in \mathbb{R}^q$, $\mathbf{z}_k \in \mathbb{R}^p$, and $\mathbf{v}_k \in \mathbb{R}^s$ are the measured output, the output reference, and measurement noise vectors, correspondingly (as shown in Fig. 4.1).

Furthermore, $\mathbf{A} \in \mathbb{R}^{n \times n}$, $\mathbf{B}_1 \in \mathbb{R}^{n \times t}$, and $\mathbf{B}_2 \in \mathbb{R}^{n \times r}$ correspond to the process, input control and input process noise matrices; $\mathbf{C}_1 \in \mathbb{R}^{p \times n}$ and $\mathbf{C}_2 \in \mathbb{R}^{q \times n}$ are the output

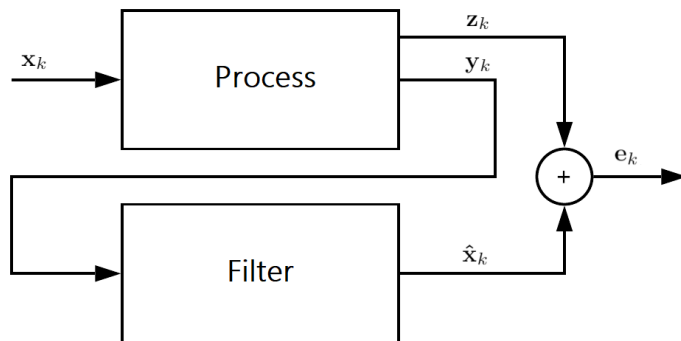


Figure 4.1 – Discrete-time system with a full order filter scheme.

reference and measured output matrices, $\mathbf{D}_{11} \in \mathbb{R}^{p \times r}$ and $\mathbf{D}_{22} \in \mathbb{R}^{q \times r}$ correspond to the process noise matrices related to the output reference and measured output; as well as $\mathbf{D}_{21} \in \mathbb{R}^{q \times r}$ is the sensor noise matrix. For the sake of simplicity, \mathbf{C}_1 and $\mathbf{C}_{1,k}$, as well as \mathbf{C}_2 and $\mathbf{C}_{2,k}$ will be treated interchangeably.

Thus, by defining a general noise vector, $\tilde{\mathbf{w}}_k = [\mathbf{w}_k \ \mathbf{v}_k]^T$ and based on what are presented in works (FAJARDO *et al.*, 2020; FAJARDO *et al.*, 2021), the dynamic of the optimal guaranteed robust \mathcal{H}_∞ filter can be described by

$$\hat{\mathbf{x}}_{k+1} = \mathbf{A}_f \hat{\mathbf{x}}_k + \mathbf{B}_f \mathbf{y}_k \quad (4.21)$$

$$\hat{\mathbf{z}}_k = \mathbf{C}_f \hat{\mathbf{x}}_k + \mathbf{D}_f \mathbf{y}_k \quad (4.22)$$

where $\hat{\mathbf{x}}_k \in \mathbb{R}^{n_f}$ is the estimated state, $\hat{\mathbf{z}}_k \in \mathbb{R}^p$ is the estimated output, as shown in Fig. 4.1. Hence, the matrices $\mathbf{A}_f \in \mathbb{R}^{n \times n}$, $\mathbf{B}_f \in \mathbb{R}^{n \times q}$, $\mathbf{C}_f \in \mathbb{R}^{p \times n}$ and $\mathbf{D}_f \in \mathbb{R}^{p \times q}$ are to be determined (GEROMEL *et al.*, 2000). In this way, from expressions (4.15)-(4.22), considering $\mathbf{e}_k = \mathbf{z}_k - \hat{\mathbf{z}}_k$, and control input does not affect the dynamic of the proposed filter, an augmented state dynamic is given by

$$\tilde{\mathbf{x}}_{k+1} = \mathbf{A}_a \tilde{\mathbf{x}}_k + \mathbf{B}_a \tilde{\mathbf{w}}_k \quad (4.23)$$

$$\mathbf{e}_k = \mathbf{C}_a \tilde{\mathbf{x}}_k + \mathbf{D}_a \tilde{\mathbf{w}}_k \quad (4.24)$$

with

$$\begin{aligned} \mathbf{A}_a &= \begin{bmatrix} \mathbf{A} & \mathbf{0} \\ \mathbf{B}_f \mathbf{C}_2 & \mathbf{A}_f \end{bmatrix} & \mathbf{B}_a &= \begin{bmatrix} \mathbf{B}_2 & \mathbf{0} \\ \mathbf{B}_f \mathbf{D}_{22} & \mathbf{D}_f \mathbf{D}_{21} \end{bmatrix} \\ \mathbf{C}_a &= \begin{bmatrix} \mathbf{C}_1 - \mathbf{D}_f \mathbf{C}_2 & -\mathbf{C}_f \end{bmatrix} \\ \mathbf{D}_a &= \begin{bmatrix} \mathbf{D}_{11} - \mathbf{D}_f \mathbf{D}_{22} & \mathbf{D}_f \mathbf{D}_{21} \end{bmatrix} \end{aligned}$$

Therefore, based on what are presented in works (FAJARDO *et al.*, 2021; FAJARDO *et al.*, 2021), a full-order filter that meets robust requirements, where the estimation error, \mathbf{e}_k , has to satisfy that $\|\mathbf{e}_k\|_2 \leq \gamma(\|\mathbf{w}_k\|_2 + \|\mathbf{v}_k\|_2)$, with the robustness

level $\gamma \in \mathbb{R}$ s.t. $\gamma > 0$, can be successfully characterized if and only if there exists a symmetric matrix $\mathbf{P} = \mathbf{P}^T > 0$ such that

$$\begin{bmatrix} \mathbf{P} & \mathbf{PA_a} & \mathbf{PB_a} & \mathbf{0} \\ * & \mathbf{P} & \mathbf{0} & \mathbf{C_a^T} \\ * & * & \mathbf{I}_r & \mathbf{D_a^T} \\ * & * & * & \gamma^2 \mathbf{I}_q \end{bmatrix} > 0 \quad (4.25)$$

In this way, following the same methodology applied in ([GEROMEL et al., 2000](#)), where the matrices $\mathbf{P} \in \mathbb{R}^{2n \times 2n}$ and its inverse, \mathbf{P}^{-1} , are partitioned into $n \times n$ blocks to convert the nonlinear matrix inequality into an LMI as follows

$$\mathbf{P} = \begin{bmatrix} \mathbf{X} & \mathbf{I}_n \\ \mathbf{I}_n & \tilde{\mathbf{X}} \end{bmatrix} \quad \mathbf{P}^{-1} = \begin{bmatrix} \mathbf{Y} & \mathbf{V}^T \\ \mathbf{V} & \tilde{\mathbf{Y}} \end{bmatrix} \quad (4.26)$$

Thus, by developing the expression, $\mathbf{P}\mathbf{P}^{-1} = \mathbf{I}_{2n}$, the following expressions are derived:

$$\mathbf{XY} + \mathbf{V} = \mathbf{I}_n$$

$$\mathbf{XV}^T + \tilde{\mathbf{Y}} = \mathbf{0}$$

$$\mathbf{Y} + \tilde{\mathbf{X}}\mathbf{V} = \mathbf{0}$$

$$\mathbf{V}^T + \tilde{\mathbf{X}}\tilde{\mathbf{Y}} = \mathbf{I}_n$$

where $\mathbf{X}, \mathbf{Y}, \tilde{\mathbf{X}}, \tilde{\mathbf{Y}} \in \mathbb{R}^{n \times n}$ are positive definite symmetric matrices. This way, defining the following nonsingular matrices:

$$\mathbf{S} = \begin{bmatrix} \mathbf{Y} & \mathbf{I}_n \\ \mathbf{V} & \mathbf{0} \end{bmatrix} \quad \mathbf{R} = \begin{bmatrix} \mathbf{Y} & \mathbf{0} \\ \mathbf{0} & \mathbf{I}_n \end{bmatrix}$$

with the following inverse matrices:

$$\mathbf{S}^{-1} = \begin{bmatrix} \mathbf{0} & \mathbf{V}^{-1} \\ \mathbf{I}_n & -\mathbf{YV}^{-1} \end{bmatrix} \quad \mathbf{R}^{-1} = \begin{bmatrix} \mathbf{Y}^{-1} & \mathbf{0} \\ \mathbf{0} & \mathbf{I}_n \end{bmatrix}$$

The following similarity transformation for the Eq. (4.25) is performed

$$\begin{bmatrix} \mathbf{R}^{-1}\mathbf{S}^T & 0 & 0 & 0 \\ 0 & \mathbf{R}^{-1}\mathbf{S}^T & 0 & 0 \\ 0 & 0 & \mathbf{I}_p & 0 \\ 0 & 0 & 0 & \mathbf{I}_r \end{bmatrix} \begin{bmatrix} \mathbf{P} & \mathbf{PA}_a & \mathbf{PB}_a & \mathbf{0} \\ * & \mathbf{P} & \mathbf{0} & \mathbf{C}_a^T \\ * & * & \mathbf{I}_r & \mathbf{D}_a^T \\ * & * & * & \gamma^2 \mathbf{I}_q \end{bmatrix} \begin{bmatrix} \mathbf{SR}^{-1} & 0 & 0 & 0 \\ 0 & \mathbf{SR}^{-1} & 0 & 0 \\ 0 & 0 & \mathbf{I}_p & 0 \\ 0 & 0 & 0 & \mathbf{I}_r \end{bmatrix} > \mathbf{0} \quad (4.27)$$

Then, by substituting the matrix, \mathbf{P} , defined in Eq. (4.26) on the resulting expression from Eq. (4.27), one has that the robust full-order filter can be characterized if and only if there exist positive definite symmetric matrices $\mathbf{X}, \mathbf{Y} \in \mathbb{R}^{n \times n}$, $\tilde{\mathbf{X}}, \tilde{\mathbf{Y}} \in \mathbb{R}^{n \times n}$, with $\mathbf{Z} = \mathbf{Y}^{-1}$; the matrix $\mathbf{V} \in \mathbb{R}^{n \times n}$ as well as the following matrices $\mathbf{F} \in \mathbb{R}^{p \times n}$, $\mathbf{G} \in \mathbb{R}^{n \times n}$, \mathbf{B}_f and \mathbf{D}_f , that minimize the robustness level $\gamma = \sqrt{\mu}$ subject to the following LMI

$$\begin{bmatrix} \mathbf{Z} & \mathbf{Z} & \mathbf{ZA} & \mathbf{ZA} \\ * & \mathbf{X} & \mathbf{XA} + \mathbf{B}_f \mathbf{C}_2 + \mathbf{G} & \mathbf{XA} + \mathbf{B}_f \mathbf{C}_2 \\ * & * & \mathbf{Z} & \mathbf{Z} \\ * & * & * & \mathbf{X} \\ * & * & * & * \\ * & * & * & * \\ * & * & * & * \\ \mathbf{ZB}_2 & \mathbf{0}_{n \times r} & \mathbf{0}_{n \times p} & \\ \mathbf{XB}_2 + \mathbf{B}_f \mathbf{D}_{22} & \mathbf{D}_f \mathbf{D}_{21} & \mathbf{0}_{n \times p} & \\ \mathbf{0}_{n \times r} & \mathbf{0}_{n \times r} & \mathbf{C}_1^T - \mathbf{C}_2^T \mathbf{D}_f^T - \mathbf{F}^T & \\ \mathbf{0}_{n \times r} & \mathbf{0}_{n \times r} & \mathbf{C}_1^T - \mathbf{C}_2^T \mathbf{D}_f^T & \\ \mathbf{I}_r & \mathbf{0}_{r \times r} & \mathbf{D}_{11}^T - \mathbf{D}_{22}^T \mathbf{D}_f^T & \\ * & \mathbf{I}_r & \mathbf{D}_{21}^T \mathbf{D}_f^T & \\ * & * & \mu \mathbf{I}_p & \end{bmatrix} > \mathbf{0} \quad (4.28)$$

In addition, the remaining matrices that describe the dynamics of the filter are given by

$$\mathbf{A}_f = \mathbf{G}(\mathbf{V}\mathbf{Z})^{-1} \quad \mathbf{C}_f = \mathbf{F}(\mathbf{V}\mathbf{Z})^{-1} \quad (4.29)$$

with $\mathbf{V} = \mathbf{I}_n - \mathbf{X}\mathbf{Z}^{-1}$, defined to simplify the notation. Finally, it is essential to note that matrices \mathbf{Z} , \mathbf{X} , \mathbf{F} , \mathbf{G} , as well as the matrices \mathbf{B}_f and \mathbf{D}_f which also describe the dynamics of the filter are variables of the problem. The main difference with the methods presented in Section 4.1 is that unlike finding an observation gain we are finding a full order dynamic filter given by the matrices \mathbf{A}_f , \mathbf{B}_f , \mathbf{C}_f and \mathbf{D}_f .

5 Control Strategy

This chapter delves into developing a robust control strategy for an affordable, anthropomorphic upper-limb prosthesis based on a UTD system to drive its 3 DoF fingers. Hence, high-level (user intend interpretation) and low-level (to drive each finger) controllers have been considered to understand this work better.

Once the UTD system's full state is known, one can input the estimated state to a controller to regulate or limit the values of specific parameters, like the fingertip force and joint torques. To do that, one can solve the forward and velocity kinematics of the finger (3-link planar arm) to know their values for every instant in time by employing the Eqs. (2.24), (2.29), as well as the following expression.

$$\mathbf{f}_{tip} = (\mathbf{J}(\mathbf{q})^T)^+ \boldsymbol{\tau} \quad (5.1)$$

where \mathbf{f}_{tip} is the force exerted by the fingertip, $\mathbf{J}(\mathbf{q})$ is the space Jacobian matrix in 2D that relates the twist of the fingertip \mathcal{V}_{tip} with the generalized velocities $\dot{\mathbf{q}}$, as follows

$$\mathcal{V}_{tip} = \mathbf{J}(\mathbf{q})\dot{\mathbf{q}} \quad (5.2)$$

At a high level, different techniques can be used to interpret the user's intent gathered by a UPI, where the vast majority are based on electromyography (EMG) as an acquisition method. Based on what the UPI has interpreted, the system decides which fingers must be flexed and which not to achieve a desired grip or gesture. Therefore, considering that the fingers on the artificial hand behave similarly to a non-back drivable system, the on-off controller was designed to achieve the flexion movements with the necessary force \mathbf{f}_{tip} to hold different objects. In contrast, the robust full-state observer estimates the angular displacement θ of the gearhead shaft for each motor (no quadrature encoders are employed) (FAJARDO *et al.*, 2020). This estimation is used to have the necessary feedback to perform the extension movement using a robust feedback controller that drives the finger back to its initial position θ_0 .

At a low level, each finger functions with an individual hybrid control strategy (on-off controller for the flexion process, robust feedback controller for the extension process), except for the thumb, which possesses, additionally, a quadrature encoder to implement a PI position controller for its rotation.

5.1 On-off Controller

Since the armature current i_a of each DC motor is the only feedback signal measured from the system, a simple force on-off controller is implemented to perform the flexion process. In this manner, by constantly monitoring the armature current i_a from each DC motor and, used together with the robust observer-based filter described in chapter 4.2, one can easily be related with the fingertip force \mathbf{f}_{tip} using expressions (2.24), (2.29), (2.30), (3.1) and (5.1). Thus, the prosthesis can perform different predefined grips, ensuring that these are stable, assuming at least three points of contact since the system limits the force exerted by each finger, as illustrated in the FSM in Fig. 5.1.

The system starts with the finger fully extended in a rest position ("open", at $\theta = \theta_0$), modeled by the state S_0 . The transition to S_1 happens when the HLC sends the command to flex the finger, c . This drives the motor and causes the finger to start closing. While in this state, the estimated fingertip force \mathbf{f}_{tip} is continuously determined and, when a predefined threshold, th , is exceeded, the transition to S_2 happens. This parameter may differ for each finger, as each one has a different size and, consequently, discrepant mechanical factors, so the calibration process was carried out experimentally. At this point, the finger is considered completely closed or could be one or more of its phalanges touching the surface of an object. Then, it will begin to open if and only if the o command is issued by the HLC, as shown by the transition from S_2 to S_3 . The alteration in state from S_3 to S_0 happens after the angular displacement, θ is approximated to its initial value $\theta_0 = 0$ (driven by the feedback controller described in Sec. 5-B). This strategy was adopted since the passive tendon (installed on each finger opposes itself to the coiling process but favors the unfurling one; therefore, it is essential to ensure that the motor's shaft rotates the same angular displacement in both processes. Finally, the closing/opening processes may be interrupted and reversed if the appropriate commands are received.

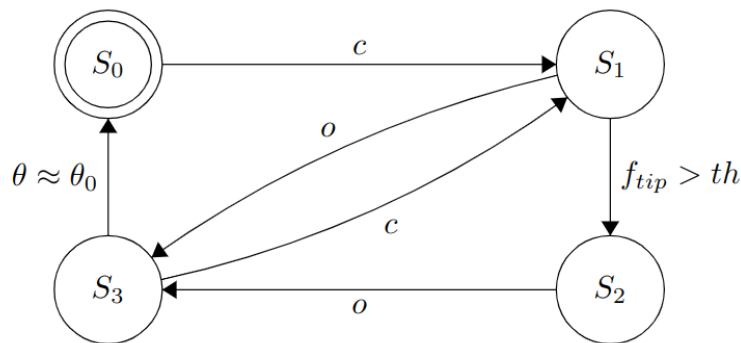


Figure 5.1 – FSM demonstrating the opening/closing behaviour of each finger.

5.2 Discrete-time \mathcal{H}_∞ Feedback Controller

A discretization of the simplified system is also required to design the feedback controller in charge of opening the fingers. Considering that the estimated state vector $\hat{\mathbf{x}}_k$ is available for feedback, that $\mathbf{x}_k \approx \hat{\mathbf{x}}_k$; and that the state information is not corrupted by the input noise \mathbf{w}_k , the characterization of the system is given by the Eq. (4.15) and the following measurement equation

$$\mathbf{y}_k = \mathbf{C}\mathbf{x}_k + \mathbf{D}\mathbf{u}_k \quad (5.3)$$

where $\mathbf{D} \in \mathbb{R}^{q \times p}$ is the feedthrough matrix. Hence, by choosing the following linear static state-feedback control law

$$\mathbf{u}_k = \mathbf{K}\mathbf{x}_k \quad (5.4)$$

where $\mathbf{K} \in \mathbb{R}^{p \times n}$ is the feedback gain that asymptotically stabilizes the closed-loop system and minimizes its \mathcal{H}_∞ norm. Such a structure produces the following closed-loop dynamics

$$\mathbf{x}_{k+1} = \mathbf{A}_c\mathbf{x}_k + \mathbf{B}_2\mathbf{w}_k \quad (5.5)$$

$$\mathbf{y}_k = \mathbf{C}_c\mathbf{x}_k \quad (5.6)$$

with

$$\mathbf{A}_c = \mathbf{A} + \mathbf{B}_1\mathbf{K}, \quad \mathbf{B}_c = \mathbf{B}_2$$

$$\mathbf{C}_c = \mathbf{C} + \mathbf{D}\mathbf{K}$$

The goal is to find a guaranteed-cost feedback gain for the system composed by (4.15) and (5.3), which has to satisfy that $\|\mathbf{y}_k\|_2 \leq \mu\|\mathbf{w}_k\|_2$, with the robustness level $\mu \in \mathbb{R}$ such that $\mu > 0$. Therefore, also from the bounded-real lemma and given the transfer function $H_{wy}(z)$ for the system (5.5)-(5.6), the norm \mathcal{H}_∞ can be characterized using a Lyapunov function, as follows

$$\min_{\mathbf{W}, \mathbf{P}=\mathbf{P}^T>0} \mu \quad (5.7)$$

subject to the following LMI

$$\begin{bmatrix} \mathbf{P} & \mathbf{AP} + \mathbf{B}_1\mathbf{W} & \mathbf{0}_{n \times q} & \mathbf{B}_2 \\ * & \mathbf{P} & \mathbf{PC}^T + \mathbf{W}^T\mathbf{D}^T & \mathbf{0}_{n \times s} \\ * & * & \mathbf{I}_q & \mathbf{0}_{q \times s} \\ * & * & * & \mu^2\mathbf{I}_s \end{bmatrix} > 0 \quad (5.8)$$

where the matrices $\mathbf{W} \in \mathbb{R}^{p \times n}$ and \mathbf{P} are the variables of the problem (OLIVEIRA; GEROMEL; BERNUSOU, 2002). Hence, \mathbf{K} can be recovered using the following expression

$$\mathbf{K} = \mathbf{WP}^{-1} \quad (5.9)$$

On the other hand, to further improve this system's robustness, a slack variable, $\mathbf{G} \in \mathbb{R}^{n \times n}$, can be incorporated so that the optimization problem is now

$$\min_{\mathbf{W}, \mathbf{G}, \mathbf{P}=\mathbf{P}^T > 0} \mu \quad (5.10)$$

which is subject to

$$\begin{bmatrix} \mathbf{P} & \mathbf{AG} + \mathbf{B}_1\mathbf{W} & \mathbf{0}_{n \times q} & \mathbf{B}_2 \\ * & \mathbf{G} + \mathbf{G}^T - \mathbf{P} & \mathbf{G}^T\mathbf{C}^T + \mathbf{W}^T\mathbf{D}^T & \mathbf{0}_{n \times s} \\ * & * & \mathbf{I}_q & \mathbf{0}_{q \times s} \\ * & * & * & \mu^2\mathbf{I}_s \end{bmatrix} > \mathbf{0} \quad (5.11)$$

Therefore, \mathbf{K} can be recovered by

$$\mathbf{K} = \mathbf{WG}^{-1} \quad (5.12)$$

6 Results

This chapter presents the results and key findings obtained from this study. These results are based on applying LMI-based filters and estimators to assistive robotics systems subject to various constraints. The chapter highlights the performance of the proposed LMI-based filters in terms of robustness, stability, and output quality. Furthermore, it comprehensively analyzes the estimation error and its upper bound for different filter structures showing the effectiveness of LMI-based filters and estimators in practical applications through two specific case studies.

6.1 Robust Control Strategy for Sensorless UTD Prosthetic Hands

The experiments to test and validate the methods proposed throughout this work were carried out using the fingers of the Galileo Hand (as shown in Fig. 6.1), controlled by a customized PCB board located on the inside of the palm of the prosthetic device, with its volar side in a supine position (FAJARDO *et al.*, 2017; FAJARDO *et al.*, 2020). These experiments simulated 20 force grips using one test bench for each finger. In this way, for the index, middle and pinky fingers, 10 flexion and extension processes were performed holding a small plastic ball of approximately 6.5 cm in diameter, and 10 processes with each finger completely closed without holding any object. For this, the armature current and the angular position of the motor axis of the fingers above were recorded to estimate the dynamics of each UTD system. In addition, these results were validated by executing different gestures and grasping in the Galileo Hand using different objects of daily living, as shown in the videos presented in the following links: [Gestures](#) and [Graspings](#).



Figure 6.1 – (a) A limb-impaired volunteer tests the Galileo Hand holding a water bottle.
 (b) The test bed used to standardize the experiment iterations of each finger interacting with a small plastic ball.

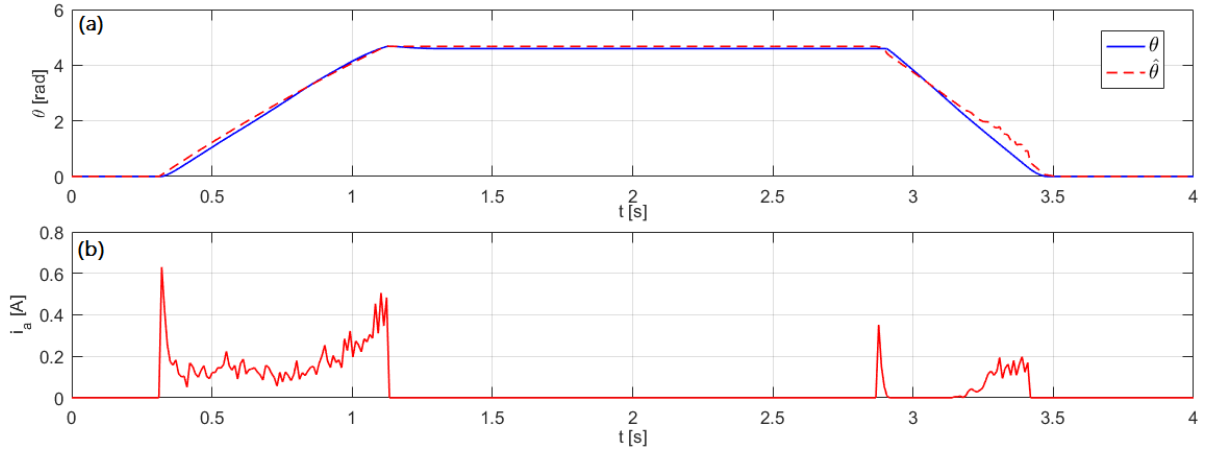


Figure 6.2 – (a) Gearhead shaft’s angular displacement, θ . The dotted red line represents the estimation $\hat{\theta}$; solid blue line, the ground truth. (b) The motor’s armature current, i_a .

However, only the mass matrix effects were considered (no gravity term since most grips for the test were in a neutral position, and no Coriolis and centripetal terms since the generalized speeds are low). MATLAB and YALMIP were utilized to design and characterize the robust \mathcal{H}_∞ observer-based filter, the \mathcal{H}_∞ full-order filter, and the robust \mathcal{H}_∞ feedback controller described in Chapters 4 and 5.2, respectively, as well as MOSEK to solve into a PC (Intel Core i7 Processor) the convex optimization problems subjected to the LMIs (APS, 2019; LOFBERG, 2004). The resulting dynamics of both control strategies were implemented in the MCU (ARM Cortex-M4) in charge of actuating the assistive device’s fingers. Fig. 6.2 presents the behavior of the on-off controller in tandem with the full-order filter in (4.2) during the flexion process of the finger and on the extension process without employing any control strategy. The upper graph shows the estimation of the angular displacement of the motor shaft, $\hat{\theta}$, juxtaposed to its ground truth alternative, θ . The lower one represents the armature current of the brushed DC motor measured by the motor driver. This estimation was established based on the data gathered by measurements acquired using the on-chip ADC for the current and the on-chip timer for the quadrature encoder attached to the motor’s shaft, with a sample rate of 2 kHz. In this manner, the gearhead’s shaft’s angular displacement when the finger is wholly flexed for the one iteration of the process for the index finger results in about 4.5971 rad, the estimated value using the method proposed in (4.1), is about 4.6775 rad while the estimated value using the method proposed in (4.2) is about 4.6253 rad. Similar results were obtained for the extension process where the error is approximately 7.2×10^{-3} mm resulting in a root mean square error (RMSE) for θ of about 0.1394 rad for the method proposed in (4.1). Fig. 6.3(c) and (d) show similar discrepancies in the extension process, where the error is approximately 5.3×10^{-3} mm resulting in a RMSE for θ of about 0.0986 rad for the method proposed in (4.2).

These measurements imply that the active tendon was coiled around 16.5 mm instead of the 16.7–16.8 mm estimation obtained with the two presented methods. A similar difference occurs in the extension process, where that error is minimal, approximately 7.2×10^{-3} mm for the method proposed in (4.1), and 2.5×10^{-3} mm for the one presented in (4.2). This results in a root mean square error for θ of about 0.1394 rad and about 0.1382 rad for both methods. Finally, the robustness level γ , is about 2.2915×10^{-6} and 1.1932×10^{-6} , respectively. These results show similar but better results for the method presented in (4.2) rather than the ones presented in (4.1) (FAJARDO *et al.*, 2020; FAJARDO *et al.*, 2021).

Furthermore, the experiment iterations for the flexion and extension process were performed only for the following fingers: index, middle, ring, and little fingers. The MCP, PIP, and DIP joints' radius and the mass and lengths for each phalange are shown in Table 6.1. In addition, armature's resistance, R_a , about 35.95 Ω, motor's inductance, L_a , about 1.3595 mH, electromotive force constant, k_e , about 2.692 mV/rad/s, elastic constant of the passive tendon, k_s , about 0.0072 N/m, moment of inertia of the rotor, J_m , about 3.458×10^{-12} kgm², motor viscous friction constant, b , of 0 Nms, a gear ratio, G_r , of 250, motor's torque constant, k_t , about 3.539×10^{-3} Nm/A and gearhead's efficiency, η , of 100%, were considered for the experiment. These values were characterized and collected experimentally under laboratory conditions using the same six micro metal gear motors used in the Galileo Hand.

Table 6.1 – Mass and length of the proximal, middle, and distal phalanges, as well as the radius of the MCP, PIP, and DIP joints for each finger.

Finger	m_1 (g)	m_2 (g)	m_3 (g)	l_1 (mm)	l_2 (mm)	l_3 (mm)	r_1 (mm)	r_1 (mm)	r_3 (mm)
Index	4.67	2.68	1.78	45	23	21	3	3.7	3.56
Middle	4.76	2.94	1.78	47	26	21	3	3.7	3.56
Ring	4.67	2.68	1.78	45	23	21	3	3.7	3.56
Pinky	4.05	2.59	1.70	38	22	20	3	3.7	3.56

The results for all the experiment iterations are presented in Table 6.2, where θ corresponds to the mean and standard deviation (SD) of the ground truth gathered by the quadrature encoder attached to the finger under evaluation. The mean and SD were determined since generating identical trajectories for each flexion process is physically impossible. In addition, e_1 is the mean and SD of the estimation error for the estimation method proposed in Sec. 4.1. At the same time, e_2 is the mean and SD of the estimation error for the method proposed in Sec. 4.2. Similar results were achieved since the angular range of motion for the MCP joint in completely closing each finger is the same for each finger; however, the lengths and masses of each phalanx only influence the fingers' kinematics and dynamics.

Table 6.2 – Ground truth and estimation error for all iterations on each finger under estimation methods proposed.

Finger	θ (Mean \pm SD)	e_1 (Mean \pm SD)	e_2 (Mean \pm SD)
Index	4.5925 ± 0.0205 rad	0.0750 ± 0.0056 rad	0.0490 ± 0.0031 rad
Middle	4.6083 ± 0.0177 rad	0.0755 ± 0.0063 rad	0.0502 ± 0.0022 rad
Ring	4.6008 ± 0.0186 rad	0.0740 ± 0.0051 rad	0.0494 ± 0.0036 rad
Pinky	4.5869 ± 0.0218 rad	0.0764 ± 0.0052 rad	0.0504 ± 0.0035 rad

The behavior of the robust output-feedback controller described in Sec. 5-B is shown in Fig. 6.3(a) and (b). As can be seen, it takes the controller about 2 seconds to complete the extension process that drives back the finger, while using full power, it only takes about 0.575 seconds, as shown in Fig. 6.3(c). In addition, the gearhead’s shaft’s angular displacement when the finger grabs the small plastic ball for the 10 processes for the index finger results in about 1.363 rad, the estimated value using the method proposed in (4.1), is about 1.352 ± 0.141 rad while the estimated value using the method proposed in (4.2) is about 1.359 ± 0.105 rad. Similar results were found by experimenting with the middle and pinky fingers. No experiments were performed with the ring finger since it has the same characteristics as the index finger.

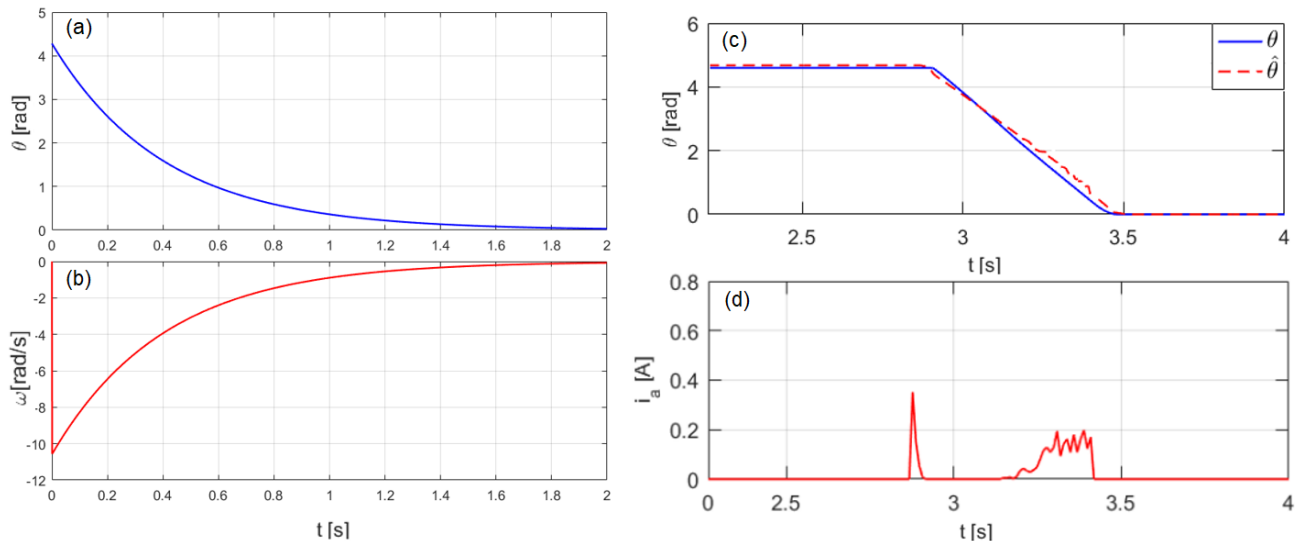


Figure 6.3 – The response of the robust controller during the extension process, (a) Gearhead shaft’s angular displacement, θ , and (b) velocity, respectively. Performance of the estimator during a full power extension process, (c) Solid blue line is the gearhead shaft’s angular displacement, θ . The dotted red line represents the $\hat{\theta}$ estimation, and (d), the current, i_a , measured on the motor’s armature.

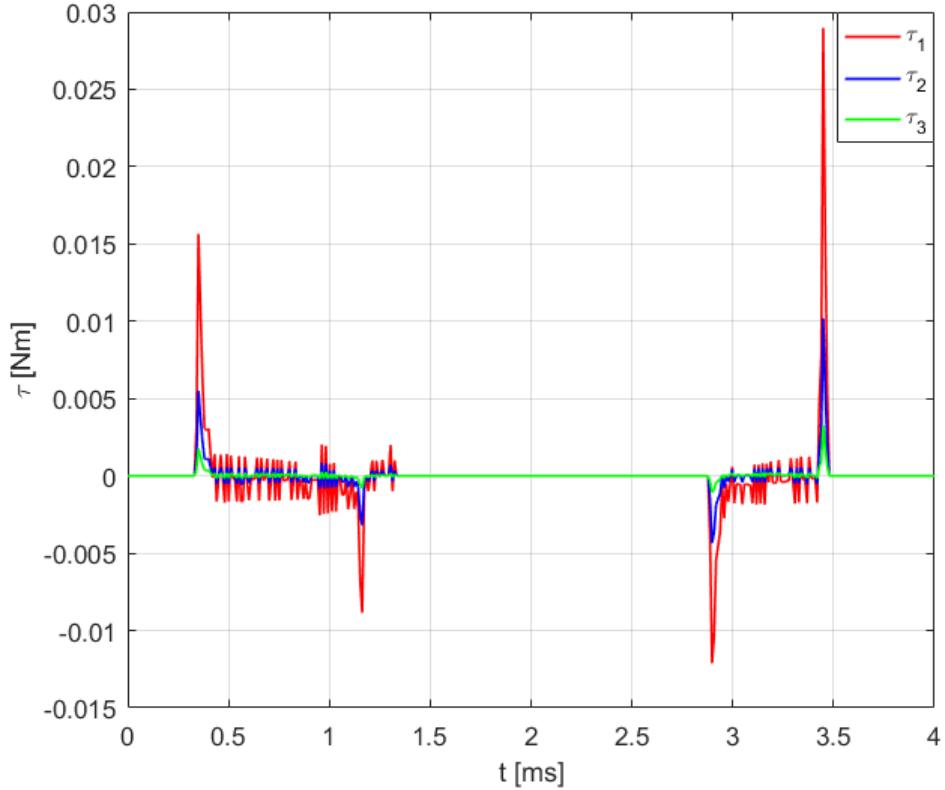


Figure 6.4 – Torque τ applied on the MCP, PIP and DIP joints’ axes (τ_1 , τ_2 and τ_3 , correspondingly).

The estimation for the angular displacement of the gearhead’s shaft, $\hat{\theta}$, was used to project the values of the generalized coordinates $\hat{\mathbf{q}}$ and then determine the resulting torque on each of the joints’ axes, the force exerted by the fingertip \mathbf{f}_{tip} , as well as an estimated trajectory of the finger. This can be visualized in Figs. 6.4, 6.5 and 6.6, where the torques exerted on the MCP, PIP, and DIP joints correspond to τ_1 , τ_2 and τ_3 , accordingly; as well as the magnitude of fingertip force with its components on x and y directions and the fingertip’s trajectory on $X - Y$ plane on the solid blue line. Thus, the estimation error for generalized coordinates, \mathbf{q} , results in $e_{\mathbf{q}} = [0.014, 0.068, 0.012]^T$.

These results were validated by instrumenting the fingertip with a force-sensitive resistor (FSR), showing that the resultant fingertip force was limited to around 0.25 N. In contrast, the model shows a limit of around 0.4 N, as shown in Fig. 6.5. This way, incrementing the fingertip force limit to 0.6 N and 0.8 N, an offset of about 0.15 N is maintained. In addition, the FSR was characterized experimentally in the laboratory using a ten well-known weights from 10 to 100 g. The data was gathered using the on-chip ADC of the main MCU of the Galileo Hand in tandem with a Wheatstone bridge in tandem with the instrumentation amplifier INA122 from Texas Instruments.

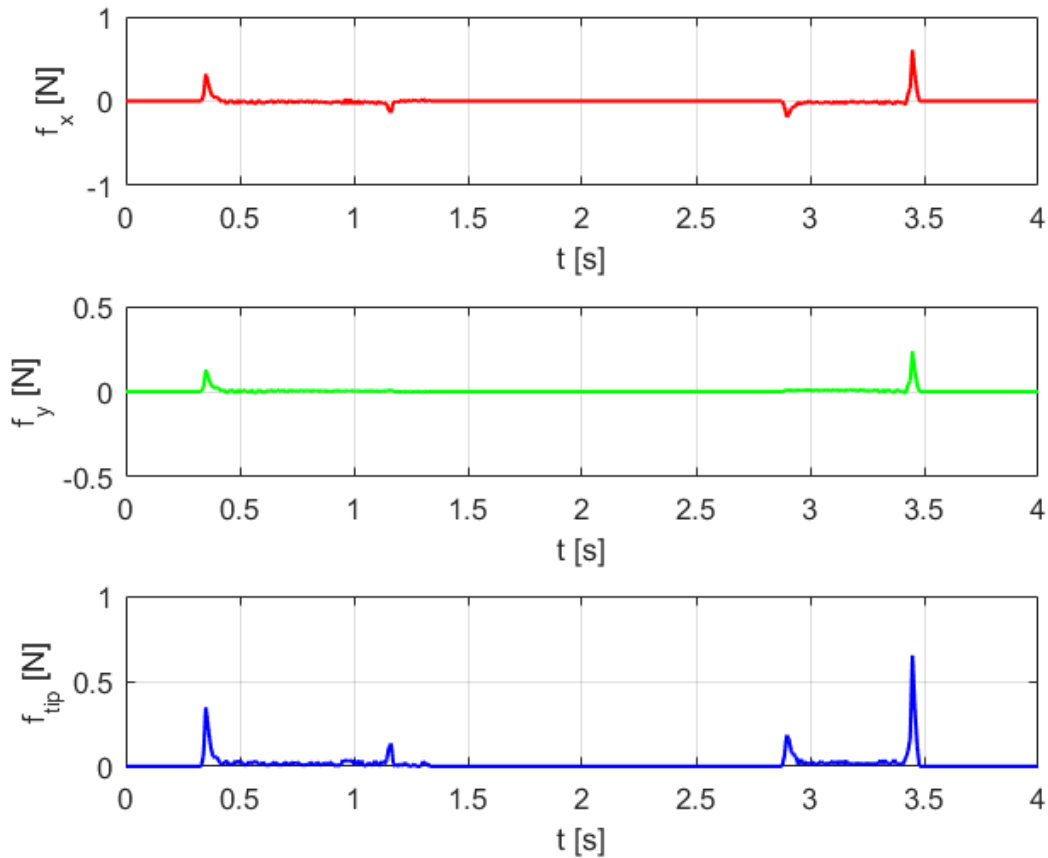


Figure 6.5 – Fingertip force f_{tip} exerted by the finger in x (red) and y (green) directions, as well as the magnitude of the resultant force (blue).

Besides, the methods proposed in Sections (4.1) and (5.2) provide (after 23 and 27 iterations, respectively) observation and output-feedback gains given by (truncated with 4 decimal digits) with $\gamma = 0.0353$ and $\mu = 0.1005$, accordingly.

$$\mathbf{L} = \begin{bmatrix} -0.5250 \\ -14.5567 \\ -0.2948 \end{bmatrix}, \quad \mathbf{K} = \begin{bmatrix} -0.1234 & 0.0001 & -1.5493 \end{bmatrix}$$

tested for the state-space representation of the simplified continuous-time system of the UTD machine described by (truncated with 4 decimal digits)

$$\mathbf{A} = \begin{bmatrix} 0.0000 & 1.0000 & 0.0000 \\ 3.7480 \times 10^{-3} & -0.4360 & 1.0230 \times 10^9 \\ 0.0000 & -1.9800 & -2.6440 \times 10^4 \end{bmatrix}, \quad \mathbf{B} = \begin{bmatrix} 0.0000 \\ 0.0000 \\ 735.6 \end{bmatrix},$$

$$\mathbf{C} = \begin{bmatrix} 0.0000 & 0.0000 & 1.0000 \end{bmatrix}, \quad \mathbf{D} = 0.0000$$

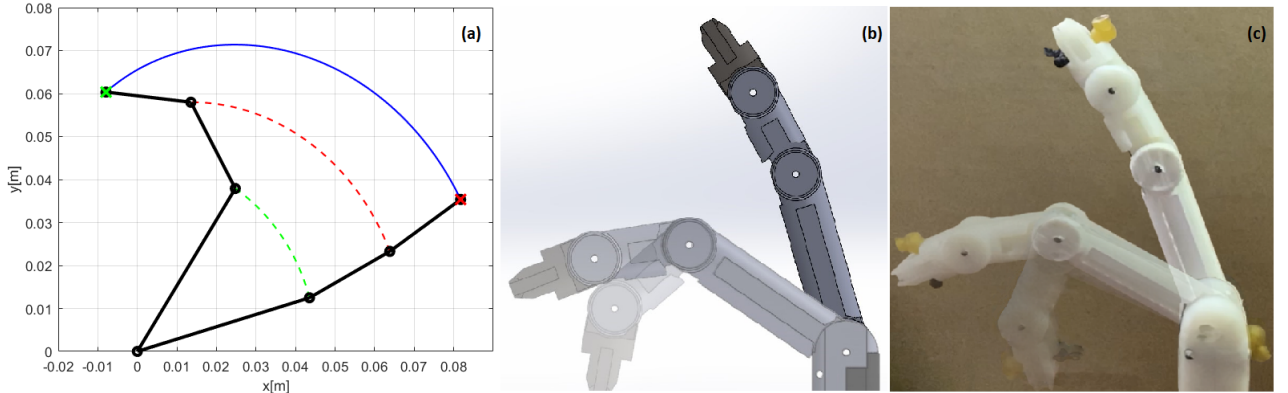


Figure 6.6 – (a) Estimated trajectory of the index finger. The solid blue line represents the trajectory of the fingertip, green and red dotted lines are the DIP and PIP joints. (b) Simulated trajectory with final generalized coordinates $\hat{\mathbf{q}} = [0.946, 1.040, 0.903]^T$ rad. (c) The ground truth for the estimated flexion process with final generalized coordinates $\mathbf{q} = [0.9323, 0.973, 0.891]^T$ rad. Either simulation and ground truth flexion movement starts in $\mathbf{q}_0 = [0.279, 0.209, 0.105]^T$ rad.

Finally, the method proposed in Section (4.2) provides (after 24 iterations) the full-order filter given by (truncated with 4 decimal digits) with $\gamma = 0.0152$, also for the same simplified continuous-time system of the UTD machine

$$\mathbf{A}_f = \begin{bmatrix} 1.0000 & 0.0000 & 0.0000 \\ -0.0110 & 0.0039 & -0.0080 \\ -1.4186 & -0.0013 & 0.0011 \end{bmatrix}, \quad \mathbf{B}_f = \begin{bmatrix} 0.0000 \\ -0.2664 \\ 0.0412 \end{bmatrix}$$

$$\mathbf{C}_f = \begin{bmatrix} -0.0124 & -0.0000 & -0.0000 \\ 0.0000 & -0.0001 & 0.0000 \\ -0.0000 & 0.0000 & 0.0001 \end{bmatrix}, \quad \mathbf{D}_f = \begin{bmatrix} 0.0000 \\ 0.0949 \times 10^{-9} \\ 0.1579 \times 10^{-9} \end{bmatrix}$$

6.2 \mathcal{H}_∞ Filters for Landmark-based Mobile Robot Localization

The experiments to test and validate the abovementioned methods were conducted using the Pioneer P3-DX robot from Adept MobileRobots in real and virtual scenarios. The real robot is equipped with a Sick LMS100 2D LiDAR, while the virtual model utilizes the fast Hokuyo 2D LiDAR available in the CoppeliaSim simulator (ROHMER; SINGH; FREESE, 2013). In addition, although the algorithms were tested in a large environment using the simulator, a small static environment which is composed of flat surfaces (i.e., walls) was built as shown in Figs. 6.7 and 6.8, both in a real scenario and under the virtual robotic simulation framework. This environment was built within an area of 4.67×3.18 meters. Thus, nine landmarks (corners) were placed at Cartesian coordinates (x_m, y_m) in meters, as follows: $\mathcal{L} = \{(0.0, 0.0), (0.0, 2.26), (0.92, 2.26), (0.92, 3.18), (4.19, 3.18), (4.19, 2.325), (4.67, 2.325), (4.67, 0.665), (4.03, 0.0)\}$. This environment was more suitable for validating, evaluating, and comparing both algorithms' performance concerning the EKF algorithm.

On the other hand, MATLAB, YALMIP, and MOSEK were also used to

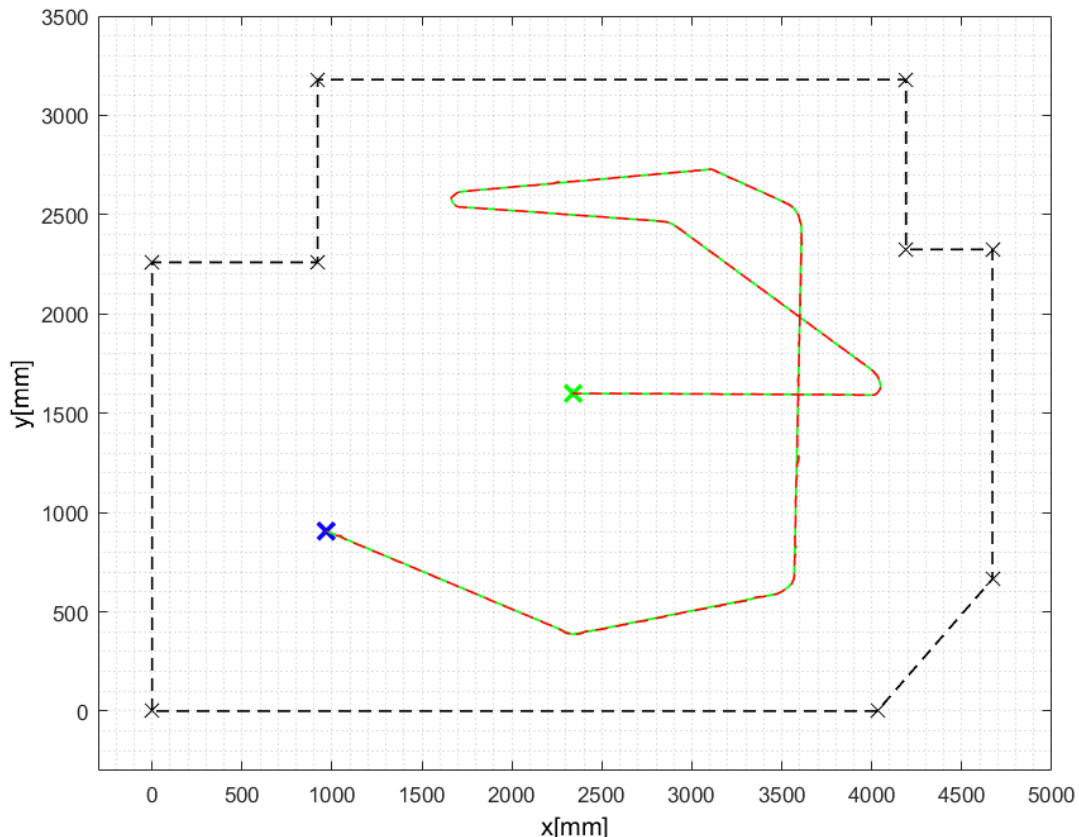


Figure 6.7 – Robot trajectory under a real controlled environment. The green cross is the robot's initial position; the blue is the final estimated position. The green and dotted red lines are the ground truth and the estimated trajectory, respectively.

implement and validate the proposed \mathcal{H}_∞ localization methods (APS, 2019; ANDERSEN; ANDERSEN, 2000; LOFBERG, 2004). All experiments (virtual and real scenarios) were run on a PC with an Intel Core i7 processor with 8 GB of RAM; RESTthru was also employed to establish communication between MATLAB, the Pioneer 3-DX robot, and the Sick LMS100 2D LiDAR (SOUZA *et al.*, 2013). These robust estimation filters also solved the convex optimization problems subjected to the LMIs described in Eqs. (4.28), (4.13) and (5.8) via interior point methods. This way, the parameters of the \mathcal{H}_∞ -based filters described in Eqs. (4.11), (4.14) and (4.29) are determined after finding a feasible solution to the optimization problems as mentioned earlier (NEMIROVSKII; GAHINET, 1994).

Furthermore, successful results were obtained with both methodologies; however, since the results were quite similar, only the results obtained by the filter gain described by Eq. (4.14) are shown in Fig. 6.7, where the solid green line illustrates the ground-truth trajectory of the differential wheeled robot, while the red dashed line illustrates its estimated position in the environment. The green and blue crosses represent the initial and final positions of the robot, respectively. In contrast, the black dashed line and small crosses illustrate the static environment and the landmarks' real positions.

Performance parameters for this scenario, such as the robot pose estimation errors for each iteration and the approximated robustness level γ , are shown in Fig. 6.9. These results were obtained using the two proposed methods and the EKF from a data

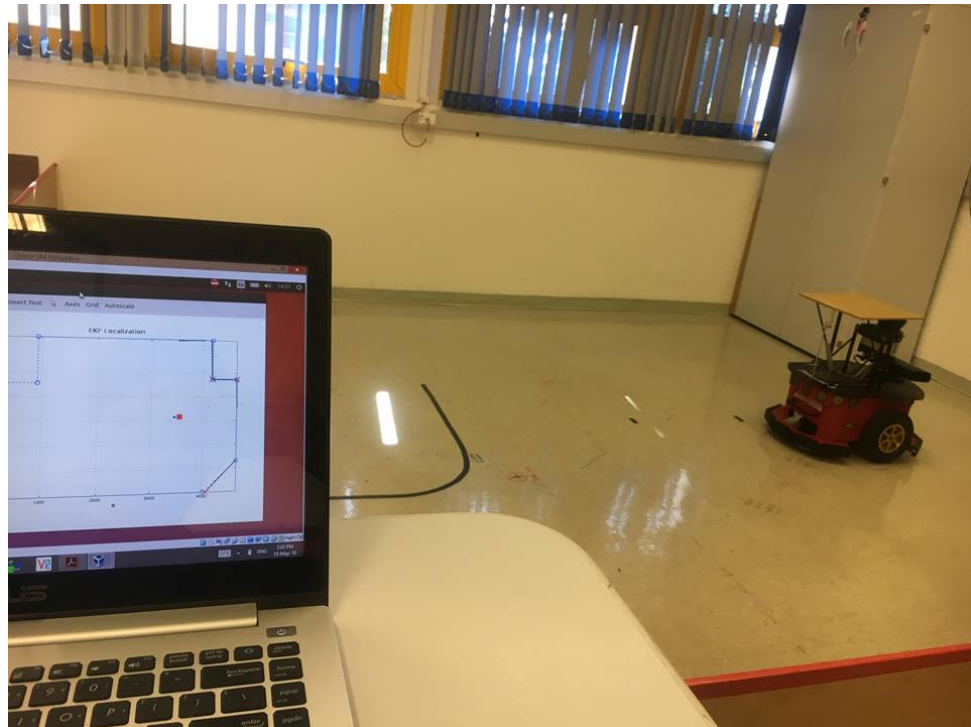


Figure 6.8 – Pioneer P3DX differential wheeled mobile robots during localization tests under the real scenario.

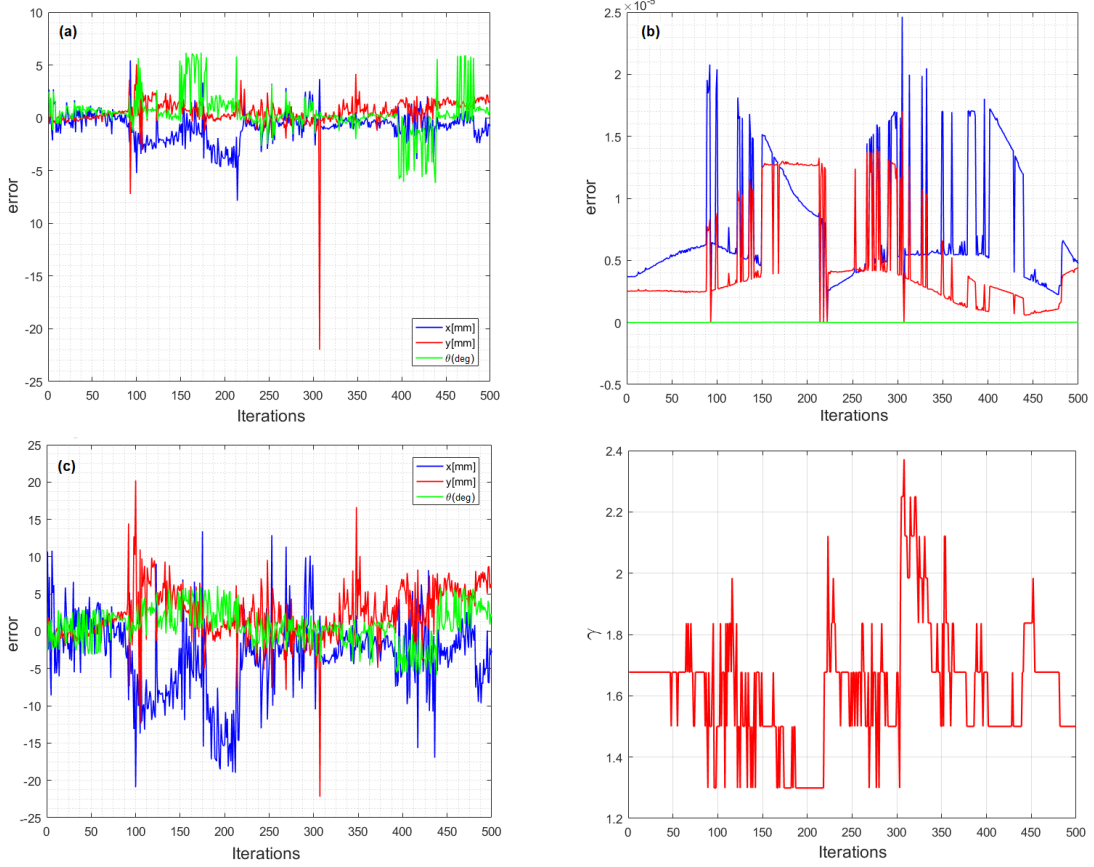


Figure 6.9 – Robot pose estimation error throughout each iteration using the method proposed in Section 4.1 under a real scenario, and using the method proposed in Section 4.2 under simulation environment are in sub-figures (a) and (b). (c) EKF pose estimation error under a real scenario. (d) Robustness level γ using the method proposed in Section 4.2 under the real environment.

collection of 500 samples at a sampling frequency of about 10 Hz. Each sample comprises the control input vector \mathbf{u}_k and a measurement vector with the 241 laser measurements at time k . As mentioned above, well-known feature extraction (corners) and landmark correspondence algorithms were employed. Each solution's complexity depends on the number of detected landmarks in the environment, reflected in the number of variables to solve in each iteration. However, both proposed methods provide convergence even if only two landmarks are observed at any time step. For the first proposed method, the amount of variables oscillates between 34 and 82 at each iteration, and its behavior is described in the same way as the Fig. 6.9(b) for the second method, the number of variables remain constant (40).

In all the tests, the observer-based filter gain matrix and the dynamic filter matrices were calculated below a time interval of approximately 100 ms. Both methodologies present small state estimation errors. Fig. 6.9(a) shows the state estimation error from the observer-based filter, as proposed in Section 4.1 and tested under a real scenario and Fig. 6.9(b) shows the state estimation error from the full-order filter proposed in

Section 4.2 under simulated environment. In contrast, Fig. 6.9(c) presents the estimation error from the EKF, also tested under a real scenario. The RMSE for each of the states are $[1.645 \text{ mm}, 1.482 \text{ mm}, 1.874^\circ]^\text{T}$ and $[6.339 \text{ mm}, 4.363 \text{ mm}, 4.311^\circ]^\text{T}$, respectively. For the method proposed in Section 4.2, the RMSE is about $[1.213 \text{ mm}, 1.028 \text{ mm}, 0.754^\circ]^\text{T}$, showing a better result than the previous methods. Finally, as shown in Fig. 6.9(d), the approximated value of γ depends on the number of landmarks detected. This result is because the length of the measured output matrix \mathbf{C}_k depends directly on the number of variables involved in the convex optimization problem at each iteration. In addition, the realization of observer gain provided by the method proposed in (4.1) and the full-order filter matrices provided by the method proposed in (4.2) were not presented since these change also depending on the linearization method mentioned above.

7 Conclusions

This thesis explores two robust filter estimation methods for linear systems with uncertain and noisy inputs applied to different case studies. This way, this research aimed to develop the methodologies, validate their functionality and, in one particular case, compare the performance of the LMI-based \mathcal{H}_∞ filter estimation methods in contrast to stochastic approaches commonly used in control theory. In general, this work first presents a simplified dynamic model of the finger, in conjunction with a design of a hybrid robust control strategy and robust \mathcal{H}_∞ estimation filters to estimate the full-stated of a UTD system and some relevant parameters, such as the angular displacement of the joints and angular displacement and fingertip force, which are helpful in the prostheses field. The overall strategy using both estimation methods has proven to be a successful alternative to other alternatives, such as installing complex arrays of sensors to control affordable prostheses for trans-radial amputees. Additionally, comparing the two robust filtering proposed methodologies, the whole strategy presents excellent results due to the advantages of that guaranteed-cost filters, which guarantee a better throughput under the \mathcal{H}_∞ robust requirements ([FAJARDO et al., 2020](#); [FAJARDO et al., 2021](#)).

The methodologies employed for this hybrid strategy are based on LMI machinery, allowing the design of more robust controls. This way, systems can better handle possible perturbations and disturbances since they do not assume typical noise characteristics. Their main drawback is the high computational power required to solve these optimization problems. However, approximating the finger dynamics to a linear system allows for solving the optimization problems on a PC capable of running MATLAB and then utilizing those results for its implementation in an MCU, allowing for a compact and affordable option to install in prosthetic devices. So, based on the extensive experimentation and analysis performed, it can be concluded that the LMI-based \mathcal{H}_∞ filter estimation methods offer several advantages over the other methods.

Firstly, the LMI-based approach provides a robust and computationally efficient solution to the filter estimation problem for sensorless and affordable prosthetic hands. This conclusion is valid once a proper linearization or simplification of the system is performed. Besides, it can handle various system uncertainties and measurement noises, making these methodologies well-suited for real-world applications where uncertainties and measurement noises are inevitable. Secondly, the LMI-based \mathcal{H}_∞ filter estimation methods also perform superior estimation accuracy compared to the Kalman filter and other stochastic approaches. This remark is because the LMI-based approach considers a broader range of uncertainties and incorporates them into the filter's design since it does not need any assumption of them, resulting in a more accurate estimation of the system

states.

The purpose of prosthetic hands is to determine whether selected fingers are fully closed, opened, or to grasp an object, rather than the fingertips' precise position and orientation. Thus, the estimation error obtained in this experiment is sufficient for ADLs' apt fulfillment. Most limb-impaired prefer basic functionalities such as holding bottles, books, or glass rather than performing complicated tasks such as writing or manipulating objects with their fingers. In those cases, they prefer to use their healthy limb, if that is the case. This reinforces the idea that better and more robust controllers are necessary to feel confident using this type of assistive device. Another relevant aspect is the robustness; despite the disturbances presented in armature current measurements, as shown in Figs. 6.2 and 6.3, where some discrepancies affect the estimation of the full state; however, it was possible to drive back the finger to the desired position.

Therefore, the proposed strategy behaves as expected, reducing noise effects on estimation and other disturbances' effects, showing better results with the full-order filter presented in 4.2, which guarantees better robustness level than the method proposed in 4.1. Additionally, this strategy was used to determine the kinematics and dynamics of each finger of any particular assistive device, such as the Galileo Hand, as shown in Figs. 6.4, 6.5, and 6.6. These results can be used to design more sophisticated control strategies for sensorless and affordable prosthetic hands, such as gravity compensation and impedance control, improving the functionality of the aforementioned prosthetic devices.

On the other hand, both theoretical remarks for landmark-based localization approaches were successfully validated for small and static environments, as shown in Fig. 6.7. More extensive performance tests must be done to validate its functionality in large environments. However, the methodologies' performance was almost unaffected when detecting fewer landmarks since both filters converged even when only two landmarks were observed. Nevertheless, the computational load seems expensive for large amounts of landmarks, for example, when using all laser measurements as landmarks (polynomial-time complexity, at least $\mathcal{O}(n^6)$ for general purpose solvers) (GAHINET *et al.*, 1994; VANDENBERGHE *et al.*, 2005).

The computational load rises due to the linearization step through Taylor series expansion about an operating point, which implies solving an optimization problem in each algorithm's iteration. However, both methods present good results by only observing two landmarks. It is also interesting to explore other linearization methodologies. This implies modeling the non-linearities as LPV systems or even using Takagi-Tsugeno fuzzy models to reduce the computational load and determine better LMIs characterizations to solve this specific problem better. Therefore, the problem's complexity could become a more challenging problem, but the filter parameters would not have to be calculated at each iteration as done. On the other hand, as shown in Fig. 6.9, the second approach

guaranteed a lower RMSE and norm than the first one, providing encouraging results for future large-scale implementations, validation with other types of sensors and kinematic models; and for possible experimentation by merging with other methodologies. Therefore, the full-order robust filter performed better than the other two compared methods in terms of RMSE and the level of robustness achieved. This means that the upper bound that limits the energy gain from the noise inputs to the estimation error ratio is lower than the others, guaranteeing better performance and robustness (more conservative), as no assumptions were made about the noise.

Therefore, the LMI-based \mathcal{H}_∞ filter estimation methods also offer more flexibility in the design process, allowing for incorporating additional performance specifications and constraints. However, designing filters that meet specific requirements, such as stability, robustness, and performance, is more challenging. Since LMI-based methodologies have been growing during the last decades, and the computational power needed to handle this approach, reliable and user-friendly LMI machinery to solve the convex optimization problems related to robust filtering are needed to get better solutions for large-scale problems.

Besides, these methodologies could also be adapted and expanded for tracking and SLAM problems. Its ability to localize a robot within an environment with only two landmarks makes it promisingly competitive against other algorithms. This advantage and the excellent performance shown by the results, especially when dealing with disturbances and noise inputs that are not necessarily Gaussian, make it attractive for use in other technological fields, such as virtual reality (VR), augmented reality (AR), and even for biomedical purposes, such as use in colonoscopy or endoscopy simulators used for the training of clinical personnel in which the tracking or location of biomedical instruments is critical for the proper handling of this type of instrumentation.

Overall, the results of this thesis suggest that the LMI-based \mathcal{H}_∞ filter estimation methods are a promising alternative to the Kalman filter and other stochastic approaches for linear systems with uncertain or noisy inputs. The robustness, accuracy, and flexibility of the LMI-based approach make it a suitable candidate for a wide range of real-world applications, including assistive robotics. However, further research can be conducted to explore the effectiveness of the LMI-based approach in more complex and non-linear systems through more advanced methods such as Takagi-Tsugeno fuzzy models or LPV control techniques.

Bibliography

- AKHTAR, A. *et al.* A low-cost, open-source, compliant hand for enabling sensorimotor control for people with transradial amputations. In: IEEE. *2016 38th Annual International Conference of the IEEE Engineering in Medicine and Biology Society (EMBC)*. [S.l.], 2016. p. 4642–4645. Cited 2 times on pages [20](#) and [21](#).
- ANDERSEN, E. D.; ANDERSEN, K. D. The MOSEK interior point optimizer for linear programming: an implementation of the homogeneous algorithm. In: *High performance optimization*. [S.l.]: Springer, 2000. p. 197–232. Cited on page [86](#).
- APS, M. The MOSEK optimization toolbox for MATLAB. *User's Guide and Reference Manual, version, v. 4*, 2019. Cited 2 times on pages [79](#) and [86](#).
- ATASOY, A. *et al.* 24 DOF EMG controlled hybrid actuated prosthetic hand. In: IEEE. *2016 38th Annual International Conference of the IEEE Engineering in Medicine and Biology Society (EMBC)*. [S.l.], 2016. p. 5059–5062. Cited on page [56](#).
- AYDOGMUS, O.; TALU, M. F. Comparison of extended-kalman-and particle-filter-based sensorless speed control. *IEEE Transactions on Instrumentation and Measurement*, IEEE, v. 61, n. 2, p. 402–410, 2011. Cited on page [21](#).
- BETKE, M.; GURVITS, L. Mobile robot localization using landmarks. *IEEE transactions on robotics and automation*, IEEE, v. 13, n. 2, p. 251–263, 1997. Cited on page [23](#).
- BIBER, P.; STRASSER, W. The normal distributions transform: A new approach to laser scan matching. In: IEEE. *Proceedings 2003 IEEE/RSJ International Conference on Intelligent Robots and Systems (IROS 2003)(Cat. No. 03CH37453)*. [S.l.], 2003. v. 3, p. 2743–2748. Cited on page [24](#).
- BIDDISS, E. A.; CHAU, T. T. Upper limb prosthesis use and abandonment: a survey of the last 25 years. *Prosthetics and orthotics international*, SAGE Publications Sage UK: London, England, v. 31, n. 3, p. 236–257, 2007. Cited on page [20](#).
- BORENSTEIN, J.; FENG, L. Measurement and correction of systematic odometry errors in mobile robots. *IEEE Transactions on robotics and automation*, New York, NY: Institute of Electrical and Electronics Engineers, c1989-c2004., v. 12, n. 6, p. 869–880, 1996. Cited on page [23](#).
- BOWES, S. R.; SEVINC, A.; HOLLIDAY, D. New natural observer applied to speed-sensorless dc servo and induction motors. *IEEE transactions on industrial electronics*, IEEE, v. 51, n. 5, p. 1025–1032, 2004. Cited on page [21](#).
- BOYD, S. *et al.* Control system analysis and synthesis via linear matrix inequalities. In: IEEE. *1993 American Control Conference*. [S.l.], 1993. p. 2147–2154. Cited on page [25](#).
- BOYD, S. *et al.* *Linear matrix inequalities in system and control theory*. [S.l.]: Siam, 1994. Cited 2 times on pages [33](#) and [66](#).

- BRIDGES, M. M.; PARA, M. P.; MASHNER, M. J. Control system architecture for the modular prosthetic limb. *Johns Hopkins APL Technical Digest*, Citeseer, v. 30, n. 3, 2011. Cited on page 19.
- BROWN, J. W.; CHURCHILL, R. V. *Complex variables and applications*. [S.l.]: McGraw-Hill,, 2009. Cited on page 29.
- CASTANEDA, C. E. *et al.* Discrete-time neural sliding-mode block control for a dc motor with controlled flux. *IEEE Transactions on Industrial Electronics*, IEEE, v. 59, n. 2, p. 1194–1207, 2011. Cited on page 22.
- CHEN, Z. *et al.* Experimental evaluation of cartesian and joint impedance control with adaptive friction compensation for the dexterous robot hand dlr-hit ii. *International Journal of Humanoid Robotics*, World Scientific, v. 8, n. 04, p. 649–671, 2011. Cited on page 22.
- CHORTOS, A.; LIU, J.; BAO, Z. Pursuing prosthetic electronic skin. *Nature materials*, Nature Publishing Group, v. 15, n. 9, p. 937, 2016. Cited 2 times on pages 21 and 54.
- CIPRIANI, C.; CONTROZZI; CARROZZA, M. C. The SmartHand transradial prosthesis. *Journal of neuroengineering and rehabilitation*, BioMed Central, v. 8, n. 1, p. 1, 2011. Cited 3 times on pages 19, 20, and 21.
- CIPRIANI, C.; CONTROZZI, M.; CARROZZA, M. C. Objectives, criteria and methods for the design of the smarthand transradial prosthesis. *Robotica*, Cambridge Univ Press, v. 28, n. 06, p. 919–927, 2010. Cited on page 19.
- CIPRIANI, C. *et al.* On the shared control of an EMG-controlled prosthetic hand: analysis of user–prosthesis interaction. *IEEE Transactions on Robotics*, IEEE, v. 24, n. 1, p. 170–184, 2008. Cited on page 54.
- CORDELLA, F. *et al.* Literature review on needs of upper limb prosthesis users. *Frontiers in neuroscience*, Frontiers, v. 10, p. 209, 2016. Cited 2 times on pages 19 and 51.
- CRANNY, A. *et al.* Thick-film force, slip and temperature sensors for a prosthetic hand. *Measurement Science and Technology*, IOP Publishing, v. 16, n. 4, p. 931, 2005. Cited 2 times on pages 20 and 21.
- CUMMINGS, D. Prosthetics in the developing world: a review of the literature. *Prosthetics and orthotics international*, SAGE Publications, v. 20, n. 1, p. 51–60, 1996. Cited on page 19.
- CUTKOSKY, M. R. On grasp choice, grasp models, and the design of hands for manufacturing tasks. *IEEE Transactions on robotics and automation*, IEEE, v. 5, n. 3, p. 269–279, 1989. Cited on page 52.
- DARIO, P. *et al.* An integrated approach for the design and development of a grasping and manipulation system in humanoid robotics. In: IEEE. (*IROS 2000*). *Proceedings. 2000 IEEE/RSJ International Conference on Intelligent Robots and Systems*. [S.l.], 2000. v. 1, p. 1–7. Cited on page 50.
- ENGEBERG, E. D.; MEEK, S. G.; MINOR, M. A. Hybrid force-velocity sliding mode control of a prosthetic hand. *IEEE Transactions on Biomedical Engineering*, IEEE, v. 55, n. 5, p. 1572–1581, 2008. Cited on page 21.

- FABRIZI, E. *et al.* A KF-based localization algorithm for nonholonomic mobile robots. In: *Theory and Practice of Control and Systems*. [S.l.]: World Scientific, 1998. p. 130–135. Cited on page 24.
- FAIRMAN, F. W. *Linear control theory: the state space approach*. [S.l.]: John Wiley & Sons, 1998. Cited on page 27.
- FAJARDO, J. *et al.* A robust H_∞ full-state observer for under-tendon-driven prosthetic hands. In: IEEE. *2020 IEEE/ASME International Conference on Advanced Intelligent Mechatronics (AIM)*. [S.l.], 2020. p. 1555–1560. Cited 5 times on pages 22, 70, 74, 80, and 89.
- FAJARDO, J. *et al.* A robust control strategy for sensorless under-tendon-driven prosthetic hands. In: IEEE. *2021 20th International Conference on Advanced Robotics (ICAR)*. [S.l.], 2021. p. 581–587. Cited 4 times on pages 22, 70, 80, and 89.
- FAJARDO, J. *et al.* Galileo hand: An anthropomorphic and affordable upper-limb prosthesis. *IEEE Access*, v. 8, p. 81365–81377, 2020. Cited 5 times on pages 24, 50, 52, 62, and 78.
- FAJARDO, J. *et al.* LMI methods for extended \mathcal{H}_∞ filters for landmark-based mobile robot localization. In: *2021 IEEE/ASME International Conference on Advanced Intelligent Mechatronics (AIM)*. [S.l.: s.n.], 2021. p. 511–517. Cited on page 70.
- FAJARDO, J. *et al.* An affordable open-source multifunctional upper-limb prosthesis with intrinsic actuation. In: IEEE. *Advanced Robotics and its Social Impacts (ARSO), 2017 IEEE Workshop on*. [S.l.], 2017. p. 1–6. Cited 7 times on pages 20, 24, 50, 55, 57, 62, and 78.
- FAJARDO, J.; LEMUS, A.; ROHMER, E. Galileo bionic hand: sEMG activated approaches for a multifunction upper-limb prosthetic. In: IEEE. *2015 IEEE Thirty Fifth Central American and Panama Convention (CONCAPAN XXXV)*. [S.l.], 2015. p. 1–6. Cited 2 times on pages 20 and 55.
- FAJARDO, J. *et al.* Evaluation of user-prosthesis-interfaces for semg-based multifunctional prosthetic hands. *Sensors*, Multidisciplinary Digital Publishing Institute, v. 21, n. 21, p. 7088, 2021. Cited on page 57.
- FARKAS, F.; HALÁSZ, S.; KÁDÁR, I. Speed sensorless neuro-fuzzy controller for brush type dc machines. In: *Proceedings of the 5th International Symposium of Hungarian Researchers on Computational Intelligence, Budapest, Hungray*. [S.l.: s.n.], 2004. p. 11–12. Cited on page 22.
- FIGARELLA, T.; JANSEN, M. Brush wear detection by continuous wavelet transform. *Mechanical systems and signal processing*, Elsevier, v. 21, n. 3, p. 1212–1222, 2007. Cited on page 21.
- FOUGNER, A. *et al.* Resolving the limb position effect in myoelectric pattern recognition. *IEEE Transactions on Neural Systems and Rehabilitation Engineering*, IEEE, v. 19, n. 6, p. 644–651, 2011. Cited on page 55.
- FOUGNER, A. *et al.* Control of upper limb prostheses: Terminology and proportional myoelectric control—a review. *Transactions on Neural Systems and Rehabilitation Engineering*, IEEE, v. 20, n. 5, p. 663–677, 2012. Cited on page 55.

- FOX, D.; BURGARD, W.; THRUN, S. Markov localization for mobile robots in dynamic environments. *Journal of artificial intelligence research*, v. 11, p. 391–427, 1999. Cited on page 24.
- FUJIWARA, E.; SUZUKI, C. K. Optical fiber force myography sensor for identification of hand postures. *Journal of Sensors*, Hindawi, v. 2018, 2018. Cited on page 55.
- GAETANI, F. *et al.* Design of an arduino-based platform interfaced by bluetooth low energy with myo armband for controlling an under-actuated transradial prosthesis. In: IEEE. *2018 International Conference on IC Design & Technology (ICICDT)*. [S.l.], 2018. p. 185–188. Cited on page 22.
- GAHINET, P. *et al.* The LMI control toolbox. In: IEEE. *Proceedings of 1994 33rd IEEE Conference on Decision and Control*. [S.l.], 1994. v. 3, p. 2038–2041. Cited on page 90.
- GEROMEL, J. C. *et al.* H_2 and H_∞ robust filtering for discrete-time linear systems. *SIAM Journal on Control and Optimization*, SIAM, v. 38, n. 5, p. 1353–1368, 2000. Cited 3 times on pages 24, 70, and 71.
- GHAOUI, L. E.; NICULESCU, S.-l. *Advances in linear matrix inequality methods in control*. [S.l.]: SIAM, 2000. Cited on page 32.
- GORDON, N. J.; SALMOND, D. J.; SMITH, A. F. Novel approach to nonlinear/non-gaussian bayesian state estimation. In: IET. *IEE proceedings F (radar and signal processing)*. [S.l.], 1993. v. 140, n. 2, p. 107–113. Cited on page 24.
- GRIGORIADIS, K. M.; WATSON, J. T. Reduced-Order H_∞ and $L_2 - L_\infty$ filtering via linear matrix inequalities. *IEEE Transactions on Aerospace and Electronic Systems*, IEEE, v. 33, n. 4, p. 1326–1338, 1997. Cited on page 25.
- GUO, W. *et al.* Mechanomyography assisted myoelectric sensing for upper-extremity prostheses: a hybrid approach. *IEEE Sensors Journal*, IEEE, v. 17, n. 10, p. 3100–3108, 2017. Cited on page 55.
- HOTSON, G. *et al.* Individual finger control of a modular prosthetic limb using high-density electrocorticography in a human subject. *Journal of neural engineering*, IOP Publishing, v. 13, n. 2, p. 026017, 2016. Cited 2 times on pages 19 and 54.
- HUR, H.; AHN, H.-S. Discrete-time H_∞ filtering for mobile robot localization using wireless sensor network. *IEEE Sensors Journal*, IEEE, v. 13, n. 1, p. 245–252, 2012. Cited on page 25.
- JETTO, L.; LONGHI, S.; VENTURINI, G. Development and experimental validation of an adaptive extended kalman filter for the localization of mobile robots. *IEEE Transactions on Robotics and Automation*, IEEE, v. 15, n. 2, p. 219–229, 1999. Cited on page 24.
- JETTO, L.; LONGHI, S.; VITALI, D. Localization of a wheeled mobile robot by sensor data fusion based on a fuzzy logic adapted kalman filter. *Control Engineering Practice*, Elsevier, v. 7, n. 6, p. 763–771, 1999. Cited on page 24.
- JIANG, L. *et al.* A modular multisensory prosthetic hand. In: IEEE. *2014 IEEE International Conference on Information and Automation (ICIA)*. [S.l.], 2014. p. 648–653. Cited 2 times on pages 20 and 21.

- JIANG, X. *et al.* Exploration of force myography and surface electromyography in hand gesture classification. *Medical engineering & physics*, Elsevier, v. 41, p. 63–73, 2017. Cited on page 55.
- JIMENEZ, M. C.; FISHEL, J. A. Evaluation of force, vibration and thermal tactile feedback in prosthetic limbs. In: IEEE. *2014 IEEE Haptics Symposium (HAPTICS)*. [S.l.], 2014. p. 437–441. Cited 2 times on pages 21 and 54.
- JOHANSEN, D. *et al.* Control of a robotic hand using a tongue control system—a prosthesis application. *IEEE Transactions on Biomedical Engineering*, IEEE, v. 63, n. 7, p. 1368–1376, 2016. Cited 2 times on pages 54 and 55.
- JOHANSSON, R. S.; WESTLING, G. Roles of glabrous skin receptors and sensorimotor memory in automatic control of precision grip when lifting rougher or more slippery objects. *Experimental brain research*, Springer, v. 56, n. 3, p. 550–564, 1984. Cited on page 21.
- KAPANDJI, I. The physiology of the joints, volume i, upper limb. *American Journal of Physical Medicine & Rehabilitation*, LWW, v. 50, n. 2, p. 96, 1971. Cited on page 51.
- KATE, J. T.; SMIT, G.; BREEDVELD, P. 3d-printed upper limb prostheses: a review. *Disability and Rehabilitation: Assistive Technology*, Taylor & Francis, v. 12, n. 3, p. 300–314, 2017. Cited on page 19.
- KHALID, A.; NAWAZ, A. Sensor less control of dc motor using kalman filter for low cost cnc machine. In: IEEE. *2014 International Conference on Robotics and Emerging Allied Technologies in Engineering (iCREATE)*. [S.l.], 2014. p. 180–185. Cited on page 21.
- KIRIY, E.; BUEHLER, M. Three-state extended kalman filter for mobile robot localization. *McGill University., Montreal, Canada, Tech. Rep. TR-CIM*, v. 5, p. 23, 2002. Cited on page 23.
- KOHLBRECHER, S. *et al.* A flexible and scalable slam system with full 3d motion estimation. In: IEEE. *2011 IEEE International Symposium on Safety, Security, and Rescue Robotics*. [S.l.], 2011. p. 155–160. Cited 2 times on pages 24 and 63.
- KONTOUDIS, G. P. *et al.* Open-source, anthropomorphic, underactuated robot hands with a selectively lockable differential mechanism: Towards affordable prostheses. In: IEEE. *Intelligent Robots and Systems (IROS), 2015 IEEE/RSJ International Conference on*. [S.l.], 2015. p. 5857–5862. Cited on page 20.
- LEVY, T. J.; BEATY, J. D. Revolutionizing prosthetics: neuroscience framework. *Johns Hopkins APL Technical Digest*, Citeseer, v. 30, n. 3, p. 223–229, 2011. Cited on page 19.
- LIU, Z. Z.; LUO, F. L.; RASHID, M. H. Speed nonlinear control of dc motor drive with field weakening. *IEEE Transactions on Industry Applications*, IEEE, v. 39, n. 2, p. 417–423, 2003. Cited on page 22.
- LOFBERG, J. YALMIP: A toolbox for modeling and optimization in MATLAB. In: IEEE. *2004 IEEE international conference on robotics and automation (IEEE Cat. No. 04CH37508)*. [S.l.], 2004. p. 284–289. Cited 2 times on pages 79 and 86.

- LU, F.; MILIOS, E. Robot pose estimation in unknown environments by matching 2d range scans. *Journal of Intelligent and Robotic systems*, Springer, v. 18, n. 3, p. 249–275, 1997. Cited on page [24](#).
- MEDYNSKI, C.; RATTRAY, B. Bebionic prosthetic design. In: MYOELECTRIC SYMPOSIUM. [S.I.], 2011. Cited on page [20](#).
- MIOZZI, C. *et al.* Feasibility of an rfid-based transcutaneous wireless communication for the control of upper-limb myoelectric prosthesis. IET, 2018. Cited on page [54](#).
- MONZÉE, J.; LAMARRE, Y.; SMITH, A. M. The effects of digital anesthesia on force control using a precision grip. *Journal of neurophysiology*, American Physiological Society Bethesda, MD, v. 89, n. 2, p. 672–683, 2003. Cited on page [21](#).
- MOUTOPOULOU, E. *et al.* Feasibility of a biomechatronic EPP Upper Limb Prosthesis Controller. In: IEEE. *2015 37th Annual International Conference of the IEEE Engineering in Medicine and Biology Society (EMBC)*. [S.I.], 2015. p. 2454–2457. Cited on page [54](#).
- NAVARAJ, W. T. *et al.* Upper limb prosthetic control using toe gesture sensors. In: IEEE. *2015 IEEE SENSORS*. [S.I.], 2015. p. 1–4. Cited 2 times on pages [54](#) and [55](#).
- NEMIROVSKII, A.; GAHINET, P. The projective method for solving linear matrix inequalities. In: IEEE. *Proceedings of 1994 American Control Conference-ACC'94*. [S.I.], 1994. v. 1, p. 840–844. Cited 2 times on pages [64](#) and [86](#).
- OLIVEIRA, M. C. d. *Controle de sistemas lineares baseado nas desigualdades matriciais lineares*. Phd Thesis (PhD Thesis) — Universidade Estadual de Campinas (UNICAMP). Faculdade de Engenharia . . . , 1999. Cited 2 times on pages [36](#) and [37](#).
- OLIVEIRA, M. C. D.; GEROMEL, J. C.; BERNUSSOU, J. Extended H_2 and H_∞ norm characterizations and controller parametrizations for discrete-time systems. *International Journal of Control*, Taylor & Francis, v. 75, n. 9, p. 666–679, 2002. Cited 4 times on pages [24](#), [67](#), [68](#), and [77](#).
- OLIVEIRA, M. C. de; SKELTON, R. E. Stability tests for constrained linear systems. In: *Perspectives in robust control*. [S.I.]: Springer, 2007. p. 241–257. Cited 2 times on pages [32](#) and [33](#).
- ORGANIZATION, W. H. *et al.* *World report on disability: World Health Organization*; 2011. [S.I.]: PLoS One. Cited on page [19](#).
- OZAWA, R.; HASHIRII, K.; KOBAYASHI, H. Design and control of underactuated tendon-driven mechanisms. In: IEEE. *2009 IEEE International Conference on Robotics and Automation*. [S.I.], 2009. p. 1522–1527. Cited 2 times on pages [52](#) and [54](#).
- PENG, C.-C.; WANG, Y.-T.; CHEN, C.-L. LIDAR based scan matching for indoor localization. In: IEEE. *2017 IEEE/SICE International Symposium on System Integration (SII)*. [S.I.], 2017. p. 139–144. Cited 2 times on pages [24](#) and [63](#).
- PILLING, D.; BARRETT, P.; FLOYD, M. Disabled people and the internet: Experiences, barriers and opportunities. Joseph Rowntree Foundation, 2004. Cited on page [19](#).

- PITT, M. K.; SHEPHARD, N. Filtering via simulation: Auxiliary particle filters. *Journal of the American statistical association*, Taylor & Francis Group, v. 94, n. 446, p. 590–599, 1999. Cited on page 24.
- PRAESOMBOON, S. *et al.* Sensorless speed control of dc servo motor using kalman filter. In: IEEE. *2009 7th International Conference on Information, Communications and Signal Processing (ICICS)*. [S.l.], 2009. p. 1–5. Cited on page 21.
- RAN, A.; VREUGDENHIL, R. Existence and comparison theorems for algebraic riccati equations for continuous-and discrete-time systems. *Linear Algebra and its applications*, Elsevier, v. 99, p. 63–83, 1988. Cited on page 36.
- ROHMER, E.; SINGH, S. P.; FREESE, M. V-REP: A versatile and scalable robot simulation framework. In: IEEE. *International Conference on Intelligent Robots and Systems (IROS)*. [S.l.], 2013. p. 1321–1326. Cited on page 85.
- ROMAO, L. B. R. R. *Projeto de Filtros para Sistemas Lineares com Critérios H-2, H-infinito e H-infinito em Faixas de Frequência por meio de Desigualdades Matriciais*. Phd Thesis (PhD Thesis) — Universidade Estadual de Campinas (UNICAMP). Faculdade de Engenharia . . . , 2017. Cited 3 times on pages 27, 29, and 34.
- ROTHWELL, J. *et al.* Manual motor performance in a deafferented man. *Brain*, Oxford University Press, v. 105, n. 3, p. 515–542, 1982. Cited on page 21.
- RYSER, F. *et al.* Fully embedded myoelectric control for a wearable robotic hand orthosis. In: IEEE. *2017 International Conference on Rehabilitation Robotics (ICORR)*. [S.l.], 2017. p. 615–621. Cited on page 55.
- SCIENCES, E. National Academies of; MEDICINE *et al.* *The promise of assistive technology to enhance activity and work participation*. [S.l.]: National Academies Press, 2017. Cited 2 times on pages 20 and 21.
- SEOK, J.-K. Frequency-spectrum-based antiwindup compensator for pi-controlled systems. *IEEE Transactions on Industrial Electronics*, IEEE, v. 53, n. 6, p. 1781–1790, 2006. Cited on page 21.
- SHAKED, U.; THEODOR, Y. H_∞ -optimal estimation: a tutorial. In: IEEE. *[1992] Proceedings of the 31st IEEE Conference on Decision and Control*. [S.l.], 1992. p. 2278–2286. Cited on page 25.
- SIEGWART, R.; NOURBAKHS, I. R.; SCARAMUZZA, D. *Introduction to autonomous mobile robots*. [S.l.]: MIT press, 2011. Cited 4 times on pages 22, 23, 44, and 62.
- SINCERO, G. C.; CROS, J.; VIAROUGE, P. Arc models for simulation of brush motor commutations. *IEEE transactions on magnetics*, IEEE, v. 44, n. 6, p. 1518–1521, 2008. Cited on page 21.
- SKELETON, R. E. Linear matrix inequality techniques in optimal control. *Encyclopedia of Systems and Control*, Springer, p. 1112–1121, 2021. Cited on page 24.
- SKELETON, R. E.; IWASAKI, T.; GRIGORIADIS, K. *A unified algebraic approach to linear control design*. [S.l.]: London, 2013. Cited 2 times on pages 32 and 33.

- SLADE, P. *et al.* Tact: Design and performance of an open-source, affordable, myoelectric prosthetic hand. In: IEEE. *2015 IEEE International Conference on Robotics and Automation (ICRA)*. [S.l.], 2015. p. 6451–6456. Cited on page 20.
- SODHI, P. *et al.* Ics: Incremental constrained smoothing for state estimation. In: IEEE. *2020 IEEE International Conference on Robotics and Automation (ICRA)*. [S.l.], 2020. p. 279–285. Cited on page 24.
- SOUZA, R. *et al.* A restful platform for networked robotics. In: IEEE. *2013 10th International Conference on Ubiquitous Robots and Ambient Intelligence (URAI)*. [S.l.], 2013. p. 423–428. Cited on page 86.
- STANGO, A.; YAZDANDOOST, K. Y.; FARINA, D. Wireless radio channel for intramuscular electrode implants in the control of upper limb prostheses. In: IEEE. *2015 37th Annual International Conference of the IEEE Engineering in Medicine and Biology Society (EMBC)*. [S.l.], 2015. p. 4085–4088. Cited on page 54.
- SUL, S.-K. *Control of electric machine drive systems*. [S.l.]: John Wiley & Sons, 2011. Cited 2 times on pages 20 and 21.
- TAKAKI, T.; OMATA, T. High-performance anthropomorphic robot hand with grasping-force-magnification mechanism. *IEEE/ASME Transactions on Mechatronics*, IEEE, v. 16, n. 3, p. 583–591, 2011. Cited on page 50.
- THRUN, S. Probabilistic robotics. *Communications of the ACM*, ACM New York, NY, USA, v. 45, n. 3, p. 52–57, 2002. Cited 2 times on pages 40 and 44.
- THRUN, S. *et al.* Robust monte carlo localization for mobile robots. *Artificial intelligence*, Elsevier, v. 128, n. 1-2, p. 99–141, 2001. Cited on page 24.
- TRACHTENBERG, M. S. *et al.* Radio frequency identification-an innovative solution to guide dexterous prosthetic hands. In: IEEE. *Engineering in Medicine and Biology Society, EMBC, 2011 annual international conference of the IEEE*. [S.l.], 2011. p. 3511–3514. Cited on page 55.
- TROCCAZ, J.; CONNOLLY, C. Prosthetic hands from touch bionics. *Industrial Robot: An International Journal*, Emerald Group Publishing Limited, v. 35, n. 4, p. 290–293, 2008. Cited on page 20.
- VANDENBERGHE, L. *et al.* Interior-point algorithms for semidefinite programming problems derived from the KYP lemma. In: *Positive polynomials in control*. [S.l.]: Springer, 2005. p. 195–238. Cited on page 90.
- VAZQUEZ-SANCHEZ, E.; SOTTILE, J.; GOMEZ-GIL, J. A novel method for sensorless speed detection of brushed dc motors. *Applied Sciences*, Multidisciplinary Digital Publishing Institute, v. 7, n. 1, p. 14, 2017. Cited on page 21.
- VISCONTI, P. *et al.* Technical features and functionalities of Myo armband: an overview on related literature and advanced applications of myoelectric armbands mainly focused on arm prostheses. *International Journal on Smart Sensing and Intelligent Systems*, Exeley Inc., v. 11, n. 1, p. 1–25, 2018. Cited on page 56.

- VOLKMAR, R. *et al.* Improving bimanual interaction with a prosthesis using semi-autonomous control. *Journal of neuroengineering and rehabilitation*, Springer, v. 16, n. 1, p. 140, 2019. Cited on page 55.
- WANG, C. M. Location estimation and uncertainty analysis for mobile robots. In: IEEE. *Proceedings. 1988 IEEE International Conference on Robotics and Automation*. [S.l.], 1988. p. 1231–1235. Cited on page 23.
- WEERASOORIYA, S.; EL-SHARKAWI, M. A. Identification and control of a dc motor using back-propagation neural networks. *IEEE transactions on Energy Conversion*, IEEE, v. 6, n. 4, p. 663–669, 1991. Cited on page 22.
- YACHIANGKAM, S. *et al.* Speed-sensorless separately excited dc motor drive with an adaptive observer. In: IEEE. *2004 IEEE Region 10 Conference TENCON 2004*. [S.l.], 2004. v. 500, p. 163–166. Cited on page 21.
- YANG, F. *et al.* Mobile robot localization using robust extended H_∞ filtering. *Proceedings of the Institution of Mechanical Engineers, Part I: Journal of Systems and Control Engineering*, Sage Publications Sage UK: London, England, v. 223, n. 8, p. 1067–1080, 2009. Cited 3 times on pages 23, 24, and 25.
- ZHOU, K.; DOYLE, J.; GLOVER, K. Robust and optimal control. *Control Engineering Practice*, Elsevier Science Publishing Company, Inc., v. 4, n. 8, p. 1189–1190, 1996. Cited 4 times on pages 27, 30, 31, and 34.
- ZHU, C. *et al.* Geometry design and tooth contact analysis of crossed beveloid gears for marine transmissions. *Chinese Journal of Mechanical Engineering*, Springer, v. 25, n. 2, p. 328–337, 2012. Cited on page 52.